HELMUT SCHMIDT
UNIVERSITÄT
Universität der Bundeswehr Hamburg

Toward Realistic Multiscale Simulations of Nanoparticle Injection Devices used for Single Particle Diffractive Imaging

Doctoral Thesis

approved by the

Faculty of Mechanical and Civil Engineering

of the

Helmut-Schmidt-University
University of the German Federal Armed Forces

for obtaining the academic degree of

Doktor Ingenieur (Dr.-Ing.)

presented by

Surya Kiran Peravali

from India

Hamburg, 2025

Referees

Univ.-Prof. Dr.-Ing. habil. Michael Breuer

Professor and Head, Department of Fluid Mechanics (PfS)
Faculty of Mechanical and Civil Engineering
Helmut-Schmidt-Universität/Universität der Bundeswehr Hamburg
Holstenhofweg 85 / Postfach 70 08 22
22043 Hamburg / Germany

Univ.-Prof. Dr.-rer. nat. habil. Jochen Küpper

Group leader Controlled Molecule Imaging, Center for Free-Electron Laser Science
Lead Scientist, Deutsches Elektronen-Synchrotron DESY
Professor in the Department of Physics, Universität Hamburg
Professor by courtesy in the Department of Chemistry, Universität Hamburg
Center for Free-Electron Laser Science (CFEL)
Deutsches Elektronen-Synchrotron DESY
Notkestrasse 85
22607 Hamburg / Germany

Univ.-Prof. Dr.-rer. nat. habil. Philipp Neumann

Lead Scientist and Head of IT-Department, Deutsches Elektronen-Synchrotron DESY
Professor, High Performance Computing & Data Science, Universität Hamburg
Deutsches Elektronen-Synchrotron DESY
Notkestrasse 85
22607 Hamburg / Germany

The day of submission: June 17, 2025

The day of completion of the oral examination: July 21, 2025

To my Guru,

Dr. M. Balakrishnan,

whose wisdom lives on
as a guiding light.

Kurzfassung

Single Particle Diffractive Imaging (SPI) ist eine leistungsstarke Technik, die in der Strukturbiologie und den Nanowissenschaften eingesetzt wird, um die dreidimensionale Struktur einzelner Nanopartikel, Biomoleküle und Viren zu bestimmen, ohne dass eine Kristallisation erforderlich ist. Durch die Bestrahlung der Partikel mit ultraschnellen Freie-Elektronen-Röntgenlaserpulsen (XFEL) werden mittels SPI Beugungsmuster aufgenommen, die zu hochauflösenden Bildern rekonstruiert werden. Eine effiziente und genaue Modellierung und Simulation von Nanopartikel-Injektionssystemen spielt eine zentrale Rolle bei der Weiterentwicklung der SPI-Experimente, die für eine optimale Qualität der Beugungsmuster auf gut fokussierte Partikelströme angewiesen sind. In dieser Arbeit werden diese Herausforderungen durch die Entwicklung und Optimierung von Multiskalen-Simulationsmethoden für Nanopartikel-Injektionsgeräte angegangen, wobei der Schwerpunkt auf dem aerodynamischen Linsensystem (ALS) und seiner Kombination mit einer kryogen gekühlten Buffergas-Zelle (BGC) liegt.

Ein hybrider für Molekular-Kontinuum-Simulationsansatz, der die klassische numerische Strömungsmechanik (CFD) basierend auf der Kontinuumsannahme und die auf der kinetischen Gastheorie basierende Direct Simulation Monte Carlo (DSMC) Methode kombiniert, wird eingesetzt, um die Strömung des trägergases und die Trajektorien der Nanopartikel in verschiedenen Strömungsregimen genau zu erfassen. Der Ansatz verbessert die Berechnungs effizienz, indem DSMC selektiv in Regionen angewendet wird, in denen molekulare Effekte dominieren, während CFD für Regionen mit niedriger Knudsen-zahl. Umfassende Auswertungen von Widerstandsmodellen aus der Literatur - einschließlich molekularer Widerstandskraftformulierungen - werden durchgeführt. Die Einführung einer relaxationsbasierten Korrektur für stark verdünnte Strömungen mit niedriger Geschwindigkeit verbessert die Vorhersage von Partikeltrajektorien, insbesondere im Übergangsbereich und in stark verdünnten gelieten.

Die Skalierbarkeit und Rechenleistung des Frameworks werden durch detailliertes Benchmarking bewertet. Zusätzliche Sensitivitätsanalysen zum Einfluss von DSMC-Parametern wie und Partikelanzahl, Gittergröße und Zeitschrittgröße unterstützen die effiziente Modellimplementierung weiter. Wichtige Benchmark-Fälle, darunter gasdynamische Düsen und Wiedereintrittsfahrzeuge, zeigen die Vielseitigkeit des Ansatzes bei der Simulation von internen und externen Strömungen.

Die ALS-Konfiguration verdeutlicht die Anwendbarkeit des Rahmens für die Modellierung von Einspritzdüsen, wo der hybride CFD-DSMC-Ansatz in Kombination mit verbesserten Widerstandsmodellen eine hervorragende Übereinstimmung mit experimentellen Daten und übertrifft damit konventionelles CFD. Eine weitere Validierung anhand gemessenen Strahlbreiten und Fokuspositionen wird für BGC- und kombinierte BGC-ALS Aufbauten für verschiedene Partikelgrößen und Einlassdrücke durchgeführt. Dieser validierte Aufbau wird wird dann zur Bewertung der Injektorleistung verwendet, wobei der Schwerpunkt auf Nanopartikeln in Proteingröße liegt, Dies ermöglicht eine aufschlussreiche Bewertung der Fokussierungseffizienz und Strahlqualität unter realistischen SPI-Bedingungen. Die BGC-ALS-Konfiguration verbessert durch die kryogene Kühlung die Fokussierung

kleinerer Partikel durch Reduzierung der thermischen Geschwindigkeiten und die Brownsche Bewegung unterdrückt und dadurch die Strahlkollimation verbessert - ideal für SPI-Experimente.

Durch die Beseitigung von Schwachstellen in aktuellen Methoden, die Validierung der Simulationsvorhersagen mittels experimentellen Ergebnissen und die Weiterentwicklung von Techniken zur Modellierung von Widerstandskräften schafft diese Arbeit eine solide Grundlage für die Optimierung von SPI-Injektorsystemen und ebnet den Weg für zukünftige Innovationen bei Nanopartikel-Injektionstechnologien.

Abstract

Single-particle diffractive imaging (SPI) is a powerful technique used in structural biology and nanoscience to determine the three-dimensional structure of individual nanoparticles, biomolecules, and viruses without the need for crystallization. By exposing freely flowing particles to ultrafast X-ray free-electron laser (XFEL) pulses, SPI captures diffraction patterns that can be reconstructed into high-resolution images. Efficient and accurate modeling and simulation of nanoparticle injection systems are essential for designing and optimizing injectors that deliver high-density, well-collimated particle streams – an important requirement for maximizing hit rates and image quality in SPI experiments. This thesis addresses these challenges by developing and optimizing multiscale simulation methodologies for nanoparticle injection devices, with a particular focus on aerodynamic lens systems (ALS) and its combination with cryogenically cooled buffer-gas cells (BGC).

A hybrid molecular-continuum simulation framework, integrating classic Computational Fluid Dynamics (CFD) based on the continuum assumption and the Direct Simulation Monte Carlo (DSMC) method based on the kinetic theory of gases, is employed to accurately capture the carrier gas flow and nanoparticle trajectories across diverse flow regimes. The approach improves the computational efficiency by selectively applying DSMC in regions where molecular-scale effects dominate, while using CFD for low Knudsen number regions. Comprehensive evaluations of drag force models from the literature including molecular drag formulations are conducted, along with the introduction of a relaxation-based correction for highly rarefied, low-speed flows, to enhance particle trajectory predictions, particularly in transitional and rarefied regimes.

The framework's scalability and computational performance are assessed through detailed benchmarking, while sensitivity analyses on DSMC parameters such as particle number, grid size, and time step size further guide efficient model implementation. Key benchmark cases, including gas dynamic nozzles and re-entry vehicles, demonstrate the framework's versatility in simulating internal and external flows.

The ALS configuration highlights the framework's applicability to injector modeling, where the hybrid DSMC/CFD approach combined with improved drag models achieve excellent agreement with experimental data, outperforming conventional CFD. Further validation against measured beam widths and focus positions is carried out for BGC and combined BGC-ALS setups across different particle sizes and inlet pressures. This validated setup is then used to assess the injector performance, with emphasis on protein-sized nanoparticles, enabling an insightful evaluation of the focusing efficiency and beam quality under realistic SPI conditions. Notably, the BGC-ALS configuration, through cryogenic cooling, enhances the focusing of smaller particles by reducing thermal velocities and suppressing Brownian motion, thereby improving the beam collimation – ideal for SPI experiments.

By bridging gaps in current methodologies, validating simulation results against experimental data, and advancing drag force modeling techniques, this thesis establishes a robust foundation for optimizing SPI injector systems and paving the way for future innovations in nanoparticle injection technologies.

Acknowledgments

This work was supported by the Helmholtz Data Science Graduate School for the Structure of Matter (DASHH, HIDSS-0002), by the Helmut-Schmidt University (HSU) – University of the German Federal Armed Forces Hamburg and by Deutsches Elektronen-Synchrotron DESY, a member of the Helmholtz Association (HGF).

First and foremost, I would like to express my deepest gratitude to my advisor, Prof. Michael Breuer, for his invaluable guidance, support, and supervision throughout my doctoral journey. I am also thankful to him for welcoming me into the Fluid Mechanics research group at Helmut Schmidt University.

I am equally grateful to my co-supervisors, Prof. Jochen Küpper and Prof. Philipp Neumann, for their continuous support and mentorship. Prof. Küpper's insightful discussions and the opportunity to work on interdisciplinary research at CFEL-CMI, DESY, greatly contributed to this work. Prof. Neumann's help with programming, HPC-related guidance, and support in accessing computing infrastructure were essential for the simulation work. I also thank him for integrating me into the HPC group at HSU and for his helpful suggestions throughout the project.

I would also like to offer special thanks to my office colleague, Khaled Boulbrachene, for his constant moral support throughout the course of this work. His encouragement, thoughtful conversations, and willingness to share ideas contributed meaningfully to both the scientific and personal aspects of my journey. I am grateful for the endless support from Dr. Amit Samanta – as a team leader, scientific coordinator, and mentor – for his guidance and thoughtful discussions within the COMOTION team at CFEL-CMI, DESY.

I would also like to thank all my present and former colleagues from Helmut Schmidt University – both in the Fluid Mechanics and HPC groups – as well as my colleagues from the CFEL-CMI group at DESY, for their support, collaboration, and the enjoyable working atmosphere. A special thanks goes to my colleagues Nidin Vadassery (CFEL-CMI), Ali Khalifa (Fluid mechanics) and Johann Antonio Duffek (HPC) for their support during this work.

I would also like to thank the organizers of the DASHH graduate school, Christiane and Heike, for their unwavering support and for providing an excellent organizational framework that benefited all of us students. I am equally grateful to my fellow DASHH students, whose active participation and friendship helped create a vibrant and supportive academic community.

I acknowledge dtec.bw – Digitalization and Technology Research Center of the Bundeswehr (project hpc.bw) for provision of computational resources on HSUper, dtec.bw is funded by the European Union – NextGenerationEU. I also acknowledge the Maxwell computational resources operated at Deutsches Elektronen-Synchrotron DESY.

I would also like to express my heartfelt thanks to my parents for their unconditional love, encouragement, and support throughout this journey – even from afar. Their belief in me has been a constant source of strength and motivation.

Contents

List of Figures

List of Tables

1 Introduction

Single-particle diffractive imaging (SPI) has become a groundbreaking technique for imaging atomic-scale structures and dynamics of nanoparticles and biomolecules [1, 2, 3]. By employing ultra-intense and ultra-short x-ray pulses generated by using X-ray Free-Electron Lasers (XFEL's) [4, 5, 6], SPI captures high-resolution diffraction patterns by scattering x-rays off individual particles. By collecting a series of such patterns from identical particles, a comprehensive three-dimensional reconstruction of their structure can be achieved. This technique holds immense promise for structural biology, material science, and nanotechnology, as it overcomes the limitations of traditional crystallography by imaging particles without the need for crystallization [7, 8, 9].

The SPI process primarily involves three key steps: First, identical samples are delivered into the XFEL beam, where a series of two-dimensional diffraction patterns are captured from randomly isolated particles. Next, these thousands of 2D diffraction patterns are aligned and reconstructed into a three-dimensional diffraction pattern. Finally, the high-resolution 3D structure of the samples is obtained through phase recovery [10, 11, 12, 13, 14] (see Figure 1.1).

Single-particle diffractive imaging (SPI) is versatile and can be applied to a wide variety of particles. It is commonly used to study biological particles such as proteins, viruses, and DNA/RNA, as well as cellular structures, which typically range in size from a few nanometers ($\approx$ 15 nm [15]) to hundreds of nanometers [9, 16, 17, 18, 19]. However, achieving the necessary experimental conditions for SPI is challenging, as the technique relies on recording thousands of diffraction patterns from identical particles. One of the primary limitations is the collection of a substantial number of high-quality diffraction patterns within a short time, which is closely tied to the efficiency of sample delivery systems [20, 21]. This process requires precise control over the injection and collimation of particle streams in the gas phase and their subsequent transfer into vacuum environments to minimize the background gas, which can lead to undesired scattering. Additionally, since any particle that interacts with the ultra-intense x-ray pulse is destroyed, new particles must be continuously replenished in real-time to maintain the stream [22]. This real-time replenishment is especially critical, as it allows for uninterrupted data collection in SPI experiments, compensating for particle loss and maintaining the integrity of the measurements.

Various sample delivery systems have been employed for single-shot imaging at XFELs, including fixed targets [23, 24], liquid jet injectors [25], and aerosol injectors [17]. Among these, aerosol injectors are widely favored due to their ability to minimize background scattering [26]. These systems must be meticulously optimized to produce dense particle streams with high purity, ensuring efficient interception of the particles by the x-ray beam and maximizing the likelihood of capturing high-resolution diffraction patterns [11, 17]. Despite their advantages, aerosol injectors face challenges such as low hit rates, which result

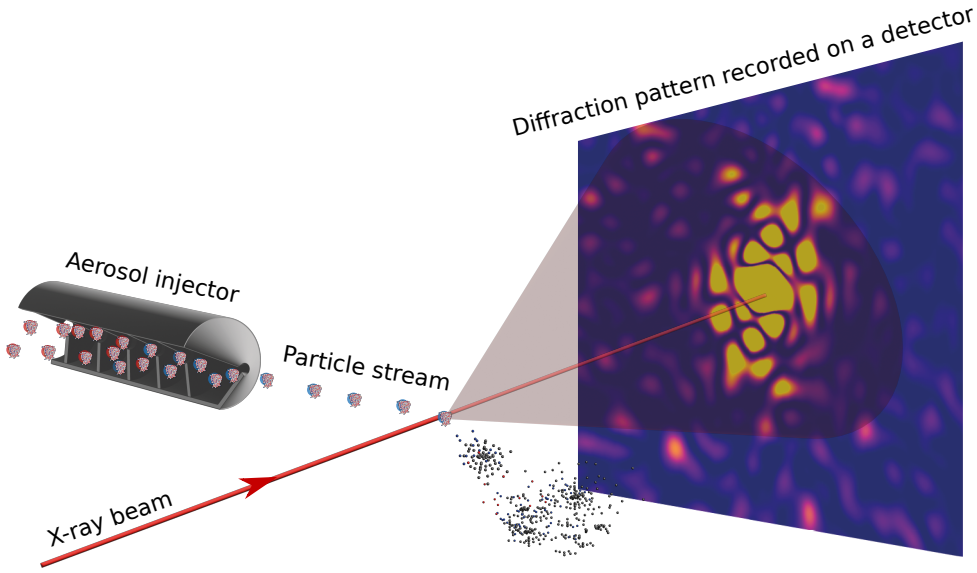

Fig. 1.1. Skematic sketch of SPI experiment.

in prolonged measurement times and excessive sample consumption [27]. Furthermore, background scattering signals from residual gas molecules emitted by the injector can obscure the sample signal, complicating data acquisition.

Developing and improving efficient aerosol injector designs is therefore crucial for SPI experiments [15]. Increasing the hit rate and collecting more high-quality diffraction patterns require further reductions in the particle beam diameter to increase sample density. To minimize background scattering noise and enhance the signal-to-noise ratio, it is essential to either reduce the amount of carrier gas or shift the particle beam's focus position within the vacuum chamber.

The aerodynamic lens stack (ALS), a key component of aerosol injectors, consists of a series of orifices designed to focus and accelerate aerosolized particles. This concept was first introduced by Liu et al. [28], based on predictions by Robinson [29] regarding the behavior of small particles in irrotational and incompressible gas flow past an obstacle. In such flows, particles experience separation from the carrier gas due to inertia, as they pass through regions of converging-diverging flow. The orifices in the ALS act as focusing lenses for the particle beams, inducing these accelerations and concentrating the particles into a narrow beam while allowing the carrier gas to dissipate. The ALS setups have been widely used in particle mass spectrometers and microscale device fabrication [30, 31].

For SPI, the widely used standard ALS-based injector, known as the "Uppsala injector", is designed to deliver collimated particle beams across a range of particle sizes from 0.1 to 3 μm [17]. However, its optimization for specific particle sizes is limited, with the pressure upstream of the ALS being the only adjustable parameter. Focussing smaller particles (20 nm), such as proteins, has always been a challenge due to their low inertia and high diffusivity [32]. These particles closely follow gas streamlines, allowing only minimal focusing to be achieved. Additionally, their motion is significantly influenced by Brownian dynamics, resulting in high diffusivity [33]. This not only broadens the particle

beam but also leads to considerable particle losses, further complicating the delivery of well-collimated particle streams for SPI experiments.

Reducing the carrier gas temperature, such as generating cold molecular beams, is a key approach to improving the injection of small particles [34]. In previous SPI experiments [35], cold molecular beams were produced using a cryogenic buffer-gas cell (BGC) for larger particles ($>$ 200 nm), where the carrier gas is cooled to 4 K. Nanoparticles are introduced into the BGC, where they undergo thermalization before exiting through an aperture into a vacuum, forming a particle beam. To enable the injection of smaller particles ($<$100 nm), experimental advancements have been made by coupling an aerodynamic lens stack (ALS) with the BGC [34]. The resulting particle beams show promise as a starting point for producing well-controlled beams. This technique not only reduces Brownian diffusion but also prevents the denaturation of protein and biomolecule particles by shock-freezing them, thereby preserving their structural integrity.

Developing and optimizing these aerosol injection systems for improving SPI involves addressing the complex interplay between particle size, flow rates, gas pressures, and operating temperatures [35, 36]. Additionally, achieving precise particle control in novel experimental regimes, such as those requiring cryogenic temperatures, adds further challenges to the optimization process. This process demands multiple iterative cycles of modifying existing injectors and evaluating their performance. Given the vast parameter space and the time-intensive nature of each step, relying exclusively on experimental observations is insufficient for achieving efficient optimization.

Numerical simulations have become an invaluable tool for gaining a deeper understanding of the underlying processes and optimizing aerosol injector performance [28, 32, 35, 36, 37, 38, 39, 40, 41]. To achieve this, it is essential to study the flow characteristics of the gas and the trajectories of the nanoparticles in detail. Moreover, the inherent complexity of the physics involved must be carefully considered when addressing these problems numerically, ensuring accurate modeling to achieve meaningful insights. Previous attempts [36, 38, 42] to establish a numerical framework primarily relied on the continuum mechanics hypothesis. In these studies, a two-step approach was typically employed: First, the flow field of the gas was simulated using Navier-Stokes-based Computational Fluid Dynamics (CFD) tools; subsequently, particle trajectories were calculated by interpolating the flow field to the positions of the particles to determine the forces (e.g., drag) on the particles. However, in certain regions of the aerosol injector, the flow partially violates the continuum assumption [34], particularly near or beyond the outlet, where the flow expands into the ultra-high vacuum environment where the flow expands into the ultra-high vacuum environment close to the interaction point with the x-ray beam. In this region, the mean free path (λ) – the average distance a molecule travels before colliding with another – increases significantly. As the flow expands, non-equilibrium effects also become pronounced, further challenging the applicability of continuum-based models. Furthermore, certain experiments require operating with low inlet pressures upstream of the ALS or using lighter carrier gases [34], both of which result in flows with higher mean free path values. The validity of the continuum assumption is quantified using the Knudsen number (Kn), defined as the ratio of the mean free path to the characteristic length of the system. When $Kn > 0.1$, the continuum-based Navier-Stokes solvers are no longer

applicable, and rarefied gas dynamics models must be utilized instead (see Figure 1.2). In such flow regimes, conventional continuum solvers fail to accurately characterize the flow field, necessitating the use of alternative approaches and the corresponding numerical methods. One such approach is the Direct Simulation Monte Carlo (DSMC) method, which provides a numerical approximation to the solution of the Boltzmann equation. Originally developed by Bird [43], the DSMC method is particularly well-suited for flows with high Knudsen numbers and has become a widely adopted technique for modeling rarefied gas flows with precision, especially in academic research.

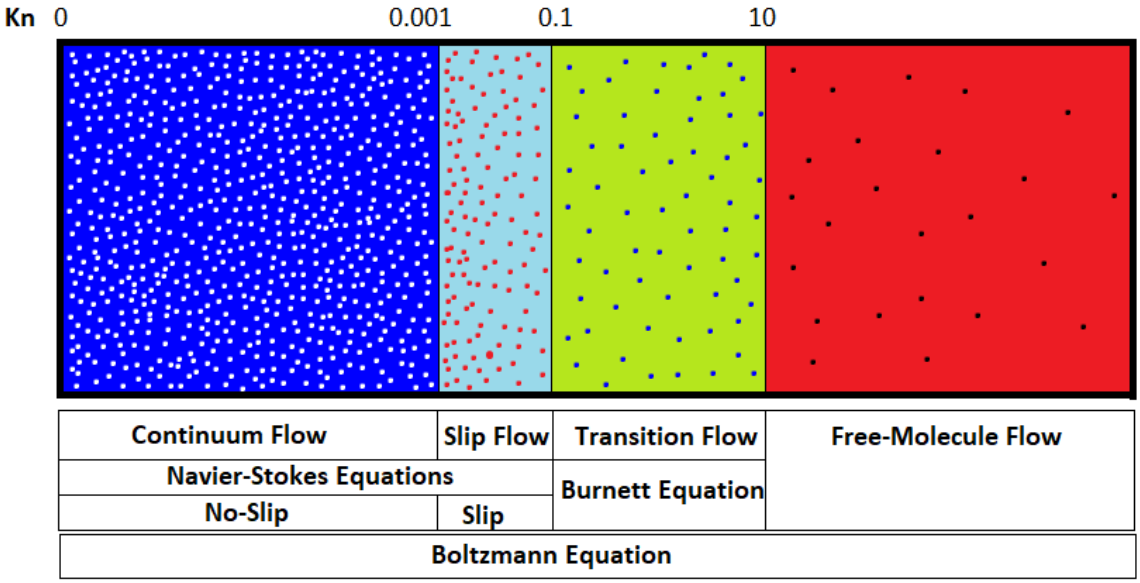

Fig. 1.2. Flow regimes depending on Kn and the governing equations.

In most SPI experiments, the flow field of particle injection spans a wide range of Knudsen number (Kn) regimes, encompassing both continuum and rarefied regions. This variability makes the selection of an appropriate solver particularly challenging. In rarefied regions, the continuum hypothesis fails, rendering CFD solvers ineffective at providing accurate results. Conversely, the computational cost of DSMC simulations, which scales with Kn^{-4} [44], can become prohibitively expensive for flows with smaller Knudsen numbers, adding significant complexity to the modeling process.

To address these challenges, a multiscale approach is essential, combining computational methods suitable for continuum flow, such as Navier-Stokes solvers, with particle-based methods like direct simulation Monte Carlo (DSMC). Such simulations enable the detailed computation of gas flows within injectors, the expansion of particles into vacuum chambers, and the resulting particle trajectories.

The path of the particles is primarily governed by drag forces, and for smaller particles, additional effects such as Brownian motion must also be considered. The validity of different force formulations [45, 46, 47, 48] in these multiscale regimes must be carefully evaluated to ensure accurate modeling. Furthermore, detailed investigations into the interaction between the flow and the particles in the high Knudsen and Mach number

regimes are crucial for understanding particle dynamics under extreme conditions. These multiscale and multiphysics simulations must account for the large phase space of experimental parameter variations, underscoring the need for efficient simulation frameworks and advanced data analysis techniques.

1.1 Objectives

This thesis addresses the challenges associated with optimizing particle injection devices for SPI through the development of a novel simulation framework. The framework combines state-of-the-art methods to simulate gas flows and particle dynamics, enabling rapid exploration of experimental parameter spaces and the derivation of actionable insights for injector design.

The objective of this work was to develop innovative multiscale simulation methodologies and advanced data analysis techniques, leveraging high-performance computing, to achieve physically more reliable predictions of the processes occurring in SPI injection systems. The approach aims to overcome several of the limitations associated with current methodologies. By enabling a deeper understanding of aerodynamic lens stacks, optimizing their performance, and extending their application range, the study seeks to advance SPI capabilities. The extensive datasets generated by simulating millions of particle trajectories will play a pivotal role in achieving these goals.

Specifically, this work focuses on:

1. **Simulating gas flows across continuum-to-rarefied transition regimes**
   Developing a hybrid molecular-continuum solver (DSMC/CFD) to accurately resolve gas flows across varying Knudsen number regimes, ensuring precise modeling in both continuum and rarefied flow regions.

2. **Modeling particle trajectories**
   Computing nanoparticle trajectories influenced by forces derived from interpolated flow fields. This involves detailed modeling of particle motion through multiscale gas flows, evaluating particle-background gas interactions, and refining existing force models for improved accuracy.

3. **Studying particle behavior in cold-gas environments**
   Extending particle trajectory modeling to cryogenic flow conditions and evaluating particle behavior under thermal cooling. Special emphasis is placed on understanding the dynamics of very small nanoparticles (< 20 nm) in such environments.

4. **Developing tools for experimental optimization**
   Providing efficient tools to minimize reliance on time-intensive trial-and-error experiments by leveraging the simulation framework for rapid evaluation and injector design guidance.

The findings of this research offer significant advancements in the design and optimization of nanoparticle injection systems for SPI. By bundling innovative multiscale

simulation methodologies and data analysis supported by high-performance computing, this work aims to improve the understanding and application range of aerodynamic lens stacks. These advancements will not only enhance particle beam quality but also optimize the overall efficiency of SPI experiments, ultimately contributing to the feasibility of molecule-imaging experiments on a larger scale

1.2 Thesis overview

This thesis is structured as follows: Chapter 2 focuses on modeling gas flows in the continuum regime using OpenFOAM [49]. The governing equations of fluid dynamics, along with the underlying modeling assumptions, are introduced. Numerical discretization techniques and solution methods employed in the `sonicFoam` and `rhoCentralFoam` solvers are discussed in detail. Additional analyses are conducted to validate the reliability and accuracy of the computational models.

Chapter 3 focuses on the rarefied flow regime, utilizing the Direct Simulation Monte Carlo (DSMC) method as implemented in SPARTA [50]. It explores key aspects such as collision models, molecular interaction models like the variable hard sphere (VHS) and variable soft sphere (VSS) approaches, and energy exchange models, including constant and variable relaxation models. These methods are employed to accurately capture the physical behavior of gases in rarefied environments. Additionally, this chapter introduces the hybrid DSMC/CFD methodology, incorporating a one-way flux-based coupling to bridge the continuum and rarefied regimes effectively. It provides an overview of related work on CFD/DSMC/hybrid simulations, summarizing studies concerning their accuracy and computational performance, and positioning the current study within the context of hybrid coupling methodologies.

Chapter 4 addresses particle transport modeling using the `CMInject` framework [42]. To provide the context for the current study, previous works on ALS simulation methodologies are reviewed. The governing equations for particle motion are introduced, with a detailed focus on the force models used to compute particle trajectories in multiscale gas flows.

Chapter 5 evaluates the CFD, DSMC, and the hybrid DSMC/CFD approaches for low-density internal and external flows, with test cases including gas dynamic nozzle expansion and shock-generating flows. Sensitivity analyses on DSMC parameters, such as particle numbers, grid size, and time step, are conducted, combined with an examination of the computational performance and energy consumption, offering insights into optimization strategies.

Chapter 6 investigates the aerodynamic lens stack in SPI systems, focusing on its behavior in multiscale and highly rarefied regimes. A hybrid DSMC/CFD simulation framework is employed to model the complex flow physics and particle trajectories accurately. Computational efficiency is improved by restricting DSMC to regions requiring molecular

modeling. Various drag force models are examined, and the approach is validated against multiple experimental configurations, demonstrating its effectiveness in enhancing particle collimation and focusing.

Chapter 7 begins by validating the simulation methodology under cryogenic flow conditions to ensure accuracy and effectiveness in extreme temperature environments. It then explores the integration of a cryogenically cooled buffer-gas cell (BGC) with an ALS in SPI injection systems to enhance particle beam quality. By combining the BGC with the aerodynamic lens stack, cryogenically cooled particle beams are generated for smaller nanoparticles, enabling even smaller nanoparticles for future applications.

Finally, Chapter 8 presents the conclusions drawn from the research, summarizing the key findings and contributions of the work. It also provides a future outlook, outlining potential avenues for further research and development in the optimization of nanoparticle injection systems and the corresponding simulation methodologies.

2 Modeling gas flows in the continuum regime

Efficient and accurate modeling of gas flows in the continuum regime forms a cornerstone for understanding the dynamics of aerodynamic injection systems [36]. This chapter delves into computational fluid dynamics (CFD) simulations performed using OpenFOAM (v2112) [49], a robust open-source framework tailored for solving partial differential equations, including the Navier-Stokes equations.

The chapter explores the application of continuum mechanics principles to describe and predict the flow behavior in scenarios where the continuum assumption holds valid. OpenFOAM's extensive library facilitates the simulation of compressible flows using either density-based or pressure-based approaches, with equations solved in a coupled or segregated manner. The methodologies described here enable accurate modeling of the flow field within aerosol injectors, which is essential for predicting injector performance, optimizing design parameters, and studying the detailed behavior of the flow inside the injector [32].

Previous CFD studies on aerosol injection for SPI [34, 35, 36, 37, 42] have utilized finite-element-based solvers such as COMSOL. In flow regimes, where the Mach number (Ma) exceeds 0.3, stabilization techniques were required to mitigate numerical instabilities arising from compressibility effects [36]. To suppress spurious oscillations – especially in high-speed flows – artificial diffusion must be introduced [51]. While these stabilization methods improve numerical robustness, they can also alter key flow features, potentially reducing the accuracy of shock capturing and sharp gradient resolution. By employing compressible finite-volume method (FVM) based solvers in OpenFOAM, this study aims to reduce the dependence on artificial stabilization while ensuring robust and physically accurate simulations of gas flows in aerodynamic injection systems.

2.1 Governing equations

The simulations in this study are based on the Navier-Stokes equations, which represent the conservation laws governing fluid dynamics. These equations are essential for capturing the behavior of continuum flows relevant to aerodynamic lens systems. The equations in the Eulerian frame of reference are given by:

- **Continuity Equation:** Governs the conservation of mass:

$$\frac{\partial \rho}{\partial t} + \nabla \cdot (\rho \mathbf{u}) = 0, \tag{2.1}$$

- **Momentum Equation:** Captures the transport of momentum, incorporating pressure gradients, viscous effects, and external forces:

$$\frac{\partial \rho \mathbf{u}}{\partial t} + \nabla \cdot (\rho \mathbf{u}\mathbf{u}) + \nabla p + \nabla \cdot \tau = 0, \tag{2.2}$$

- **Energy Equation:** Accounts for energy conservation, including heat transfer and compressibility effects:

$$\frac{\partial \rho E}{\partial t} + \nabla \cdot (\rho \mathbf{u} E) + \nabla \cdot (p\mathbf{u}) + \nabla \cdot (\tau \cdot \mathbf{u}) + \nabla \cdot \mathbf{J} = 0, \tag{2.3}$$

where ρ is the mass density, $\mathbf{u}$ is the fluid velocity vector, p is the pressure, E is the energy density given by:

$$E = e + \frac{|\mathbf{u}|^2}{2} \tag{2.4}$$

with e being the specific internal energy, τ is the viscous stress tensor represented for a Newtonian fluid by:

$$\tau = -\mu \left[\nabla \mathbf{u} + (\nabla \mathbf{u})^T - \frac{2}{3}(\nabla \cdot \mathbf{u})\mathbf{I} \right]. \tag{2.5}$$

Here, $\mathbf{I}$ is the unit tensor, $\mathbf{J}$ is the diffusive flux of heat with the thermal conductivity k and the temperature T,

$$\mathbf{J} = -k \, \nabla T. \tag{2.6}$$

2.2 Modeling assumptions

The following key assumptions are adopted to simplify the modeling and to ensure computational efficiency for the flow conditions under consideration:

- **Flow Regime:** Due to the low characteristic Reynolds numbers of the cases considered in this work ($Re < 10$), the flow is assumed to be laminar. Turbulence modeling is not required as the flow remains stable and free from turbulent fluctuations.

- **Equation of State:** The gas is modeled as a perfect gas, assuming it follows the ideal gas law:

$$p = \rho \, R \, T, \tag{2.7}$$

  where R is the specific gas constant.

- **Transport Properties:** The temperature dependence of the dynamic viscosity μ is estimated using the Sutherland transport model [52]:

$$\mu = \frac{A_s \sqrt{T}}{1 + T_s/T}, \tag{2.8}$$

where A_s is the Sutherland coefficient, T_s is the Sutherland temperature, and T is the absolute temperature. These coefficients are chosen based on the properties of the working gas and are specified in Chapter 5, Chapter 6 and Chapter 7. For cases where accurate Sutherland coefficients are not available, a simplified `constTransport` model is used [53], which assumes constant μ and Prandtl number Pr.

These assumptions ensure that the numerical simulations accurately capture the flow behavior in the continuum regime.

2.3 OpenFOAM solvers and numerical discretization

The governing equations are discretized and solved using the finite-volume method (FVM), which forms the backbone of OpenFOAM's numerical framework. In FVM, the computational domain is divided into non-overlapping control volumes, and the conservation equations for mass, momentum, and energy are integrated over each control volume. Fluxes across the cell faces are approximated, resulting in a set of algebraic equations that are solved iteratively to determine the field variables such as the velocity $\mathbf{u}$, the pressure p, and the temperature T. This approach ensures the conservation of mass, momentum, and energy at the control volume level, making it a robust and versatile method for solving fluid dynamics problems.

OpenFOAM employs a collocated variable arrangement, where all field variables (such as velocity, pressure, and temperature) are stored at the cell centers. The collocated variable arrangement is particularly popular in industrial CFD solvers as it provides greater flexibility in mesh generation for complex three-dimensional geometries, as well as for incorporating features such as refinement, grading, and surface layers. However, it requires appropriate interpolation schemes to maintain numerical stability and prevent non-physical oscillations in the pressure and velocity fields. In pressure-based solvers (e.g., `sonicFoam`, `rhoPimpleFoam`, `rhoSimpleFoam`.), this is addressed using techniques like Rhie-Chow interpolation [54], which introduces a pressure-gradient correction to stabilize the solution and to ensure proper velocity-pressure coupling. In contrast, density-based solvers (e.g., `rhoCentralFoam`) inherently handle this coupling through flux-based formulations, eliminating the need for explicit pressure-correction steps. Instead of solving for the pressure iteratively, these solvers compute the pressure from the equation of state of a perfect gas. To ensure numerical stability, density-based solvers rely on flux splitting techniques and upwind-biased numerical dissipation [55, 56]. The central-upwind schemes [57] employed in `rhoCentralFoam` compute numerical fluxes using local wave-speed estimates, allowing a smooth transition between second-order central differencing in smooth regions and upwind schemes near shocks or discontinuities. This approach provides a balance between accuracy and stability, making it particularly well-suited for high-Mach number flows and shock-dominated problems.

The OpenFOAM framework provides both pressure-based and density-based approaches for solving compressible flow problems, implemented through solvers such as `sonicFoam` and `rhoCentralFoam`, respectively. This section elaborates on the numerical techniques

employed by these solvers, with a comparative evaluation of their performance presented in Chapter 5.

2.3.1 Pressure-based solver: `sonicFoam`

`sonicFoam` is a pressure-based, transient solver designed for compressible flows. It employs the Pressure-Implicit with Splitting of Operators (PISO) algorithm [58], a semi-implicit method that divides the pressure-velocity coupling into sequential steps for computational efficiency. By iteratively updating pressure and velocity corrections, PISO ensures stability for large time steps and captures transient flow features such as acoustic waves and moderate compressibility effects.

A key feature of `sonicFoam` is the derivation of the pressure equation directly from the discrete forms of the momentum and continuity equations, as proposed by Issa [58]. This approach ensures compatibility between the pressure and velocity fields, avoiding inconsistencies that could violate the continuity equation. The resulting solver achieves robust and accurate solutions for compressible flow problems, making it well-suited for aerodynamic and thermodynamic applications.

To refine the solution, `sonicFoam` follows a predictor-corrector strategy based on the PISO algorithm, ensuring compatibility with the continuity equation. The process begins with a momentum predictor step, where the momentum equation is solved to obtain an intermediate velocity field without enforcing mass conservation. A pressure-correction equation, derived from the continuity equation, is then solved to update the pressure. Using this corrected pressure gradient, the velocity field is adjusted to maintain consistency with the momentum equation. Unlike incompressible solvers, where pressure corrections primarily enforce divergence-free velocity fields, `sonicFoam` also includes the energy equation in the PISO loop. This step updates the temperature or internal energy field, ensuring proper coupling between density, pressure, and thermodynamic variables. This approach is particularly important for temperature-dependent flows and compressible regions, where variations in density and energy transport influence the overall solution. If necessary, additional corrector loops are applied to further refine the velocity, pressure, and energy fields for improved accuracy [59].

To improve solution stability and prevent numerical oscillations, `sonicFoam` employs total variation diminishing (TVD) schemes [60] in the discretization of convective fluxes. These schemes dynamically adapt between central differencing in smooth regions (for high accuracy) and upwind-biased interpolation near steep gradients (for improved stability). One commonly used TVD scheme in `sonicFoam` is the van Leer limiter, which adjusts numerical dissipation based on local flow gradients, reducing spurious oscillations while maintaining second-order accuracy. The application of TVD flux limiting enhances solution stability in flows where shocks or expansion waves may be present. However, since `sonicFoam` is a pressure-based solver, it does not inherently capture strong discontinuities as effectively as density-based solvers. Additional stabilization, such as mesh refinement or artificial viscosity, may be required in cases involving high-Mach number flows to prevent numerical artifacts near sharp gradients.

Temporal and Spatial Discretization: `sonicFoam` employs the first-order implicit `Euler` scheme for time discretization, which is particularly suitable for transient simulations due to its simplicity and efficiency. Alternative higher-order schemes, such as the implicit `backward` or `Crank-Nicolson (CN)` schemes, are also available for enhanced stability or second-order accuracy in time. Spatial gradients are computed using the `Gauss linear` scheme, with a cell-limited variant for velocity gradients (`grad(U)`[1]) to ensure stability in regions of steep gradients. Divergence terms – for instance, for velocity (e.g., $\nabla \cdot (\rho \mathbf{uu}) \Rightarrow$ `div(phi,U)`) – are discretized using flux limiters such as `Gauss vanLeerV` [61], further promoting TVD behavior. Additionally, the pressure and energy divergence terms adopt `Gauss limitedLinear` schemes [60], while Laplacian terms are treated using the `Gauss linear limited corrected` scheme [60] to improve accuracy on non-orthogonal meshes. For the remaining flow properties, a standard `linear` interpolation is used for transferring cell-center values to face centers across the computational domain, with surface-normal gradients computed via the `corrected` approach [53].

Solution Methods: Within the PISO loop, the pressure equation is solved using the Preconditioned Bi-Conjugate Gradient Stabilized (`PBiCGStab`) method [62, 63] with a `DILU` preconditioner [60], while the velocity and energy equations use similar solver settings to ensure consistency. The density equation is handled by a `diagonal` solver. The solver employs the PISO algorithm, which is configured by setting `nOuterCorrectors` to 1 within the PIMPLE dictionary[2]. Additionally, `nCorrectors` is set to 2, ensuring two pressure-correction steps per time step, while no non-orthogonal corrections are applied—thus balancing computational cost and accuracy. Convergence in `sonicFoam` is further controlled via absolute (`tolerance`) and relative (`relTol`) thresholds specified in the `fvSolution` dictionary (Appendix A).

2.3.2 Density-based solver: `rhoCentralFoam`

The `rhoCentralFoam` solver utilizes a density-based approach to model high-speed compressible flows. It is particularly well-suited for cases involving shock waves, contact surfaces, and other discontinuities, where numerical accuracy and stability are critical. Unlike pressure-based solvers, which rely on iterative pressure corrections, `rhoCentralFoam` solves for the density, momentum, and energy directly, with the pressure coupled through the equation of state.

The solver is based on semi-discrete, non-staggered, Godunov-type central-upwind schemes [55, 56], which approximate numerical fluxes without requiring explicit Riemann solvers. Unlike methods such as AUSM [64], HLLC [65], and Roe's solver [66], `rhoCentralFoam` avoids solving the Riemann problem at each interface, instead integrating fluxes over the Riemann fan [56]. This approach eliminates the need for characteristic decomposition and eigenvalue calculations, reducing computational costs while ensuring robustness. The method, implemented in OpenFOAM by Greenshields et al. [57], is

[1] Representation in OpenFOAM dictionary
[2] Setting `nOuterCorrectors` > 1, the solver uses PIMPLE [60].

particularly effective for unstructured meshes with arbitrary polyhedral cells, making it well-suited for complex geometries.

A key advantage of `rhoCentralFoam` is that it avoids the carbuncle phenomenon [67, 68], a well-known instability observed in Riemann solvers when handling strong shocks [69]. This increased stability and simplicity make it well-suited for supersonic and hypersonic flows, where accurate shock capturing is essential.

Unlike fully explicit Godunov-type solvers, `rhoCentralFoam` employs a central-upwind flux splitting approach, which applies central differencing in smooth regions while introducing upwind dissipation near discontinuities to ensure stability. To further enhance numerical robustness, total variation diminishing (TVD) schemes are applied during flux reconstruction rather than directly in the convective flux discretization [57], enabling high-resolution shock capturing while maintaining solution stability.

The solution procedure begins by reconstructing the density, velocity, and temperature at cell faces using the van Leer limiter, ensuring smooth and oscillation-free interpolation. Fluxes, including mass, momentum, and energy, are then computed using the central-upwind flux splitting approach, ensuring robust capture of shock waves – preventing spurious oscillations near steep gradients while preserving high accuracy in smooth regions. The mass conservation equation is solved first to determine the density, followed by an inviscid momentum update, which is then corrected for the viscous effects through a diffusive velocity correction step. Similarly, the energy equation is advanced using an inviscid predictor step, followed by a diffusive temperature correction to account for heat conduction. Finally, the pressure is updated using the ideal gas law, ensuring thermodynamic consistency [57, 59].

Temporal and Spatial Discretization: `rhoCentralFoam` employs the first-order implicit `Euler` scheme for time discretization. Although the `Euler` scheme is straightforward and efficient for transient compressible flow simulations, similar to `sonicFoam` alternative higher-order schemes – such as the implicit `backward` or `Crank-Nicolson (CN)` schemes – are available for enhanced temporal accuracy if required. Spatial discretization is achieved using the `Gauss linear` scheme for gradient calculations, with a cell-limited reconstruction applied during flux splitting to enforce TVD behavior. In particular, `rhoCentralFoam` employs the `Kurganov` flux scheme – derived from central-upwind methods – for high-speed flows. Divergence terms (e.g., for viscous fluxes such as $\nabla \cdot \tau \Rightarrow$ `div(tauMC)`) are discretized using `Gauss linear`, while Laplacian terms are treated with the `Gauss linear limited corrected` scheme [60] to handle non-orthogonal meshes effectively. For reconstruction, the `vanLeer` limiter is used for scalar quantities like ρ and T, while the `vanLeerV` limiter is applied to the velocity vector field $\mathbf{u}$ to ensure consistent TVD behavior for vector quantities. As with `sonicFoam`, surface-normal gradients are computed via the `corrected` approach [53].

Solution Methods: The governing conservation equations in `rhoCentralFoam` are solved sequentially. A `diagonal` solver is used for the density, while the momentum equation (i.e., for $\rho\mathbf{u}$) is typically solved using a Gauss–Seidel-based method (e.g., `smoothSolver`). The energy equation (ρE) is solved with similar settings, often employing stricter tolerances

to improve accuracy. Since the pressure is updated via the ideal gas law after the conservation equations are solved, there is no separate pressure-correction loop. Convergence is controlled through absolute (`tolerance`) and relative (`relTol`) thresholds specified in the `fvSolution` dictionary (Appendix A).

The combination of the `Kurganov` flux scheme, TVD stabilization in flux reconstruction, and straightforward iterative solvers makes `rhoCentralFoam` a robust tool for gas-dynamic simulations involving shock-dominated flows, including supersonic jet interactions, hypersonic vehicle aerodynamics, and high-enthalpy flow studies.

To summarize Table 2.1 compares the key features of `sonicFoam` and `rhoCentralFoam`. The choice between these solvers depends on the specific application requirements. A detailed evaluation and validation of their performance is presented in Chapter 5. The following subsections provide details on discretization schemes, solution methods, boundary conditions, and parallelization options used in the simulations.

Feature	**`sonicFoam`**	**`rhoCentralFoam`**
Solver Type	Pressure based	Density based
Flux Scheme	Central differencing with Rhie-Chow interpolation	Central-upwind flux splitting
Pressure Handling	Iterative pressure correction (PISO)	Pressure naturally coupled via the equation of state (EOS)
Shock Handling	Requires additional stabilization techniques	Naturally shock-capturing via flux splitting
TVD Application	TVD applied to convective fluxes	TVD applied in flux reconstruction (ρ, $\mathbf{u}$, T)
Ideal Flow Regimes	Moderate-speed compressible flows	High-speed, shock-dominated flows

Tab. 2.1. Comparison of `sonicFoam` and `rhoCentralFoam` solvers in OpenFOAM.

2.4 Boundary conditions

Boundary conditions in OpenFOAM define how the computational domain interacts with its surrounding and are crucial for ensuring numerical stability and physical accuracy. The domain is divided into patches, and specific conditions are assigned to each patch for variables such as velocity, pressure, and temperature. These boundary conditions are broadly categorized as Dirichlet or Neumann types.

Dirichlet boundary conditions specify fixed values for field variables on a boundary and are implemented using the `fixedValue` keyword. For example, a fixed inlet velocity or a constant wall temperature can be applied using this approach. Neumann boundary conditions enforce a fixed gradient, or zero gradient, using `fixedGradient` or `zeroGradient`, commonly employed at outlets to allow variables to adjust freely.

OpenFOAM also provides specialized boundary conditions for complex flow scenarios. The `waveTransmissive` [70] condition, for instance, minimizes wave reflections at outlets in compressible flow simulations, making it ideal for high-speed flows with shock waves. Similarly, the `supersonicFreestream` [49] condition handles supersonic inflows and outflows by ensuring natural adjustments without reflections, which is critical for aerodynamic and propulsion applications.

At walls, boundary conditions vary based on the flow physics. For viscous flows, the no-slip condition sets the velocity to zero, while the slip condition eliminates tangential velocity components, simulating inviscid behavior. Additionally, walls are typically treated as impermeable surfaces, meaning the normal velocity component must be zero to prevent fluid penetration. Thermal boundaries at walls can either maintain a fixed temperature or are insulated with zero heat flux, depending on the setup.

Symmetry and periodic conditions further simplify the modeling of flows in symmetric geometries or repeating domains. The `symmetryPlane` enforces zero normal gradients, while the `cyclic` condition connects opposite patches, often used in rotating machinery or periodic flows.

While OpenFOAM provides a wide array of additional boundary conditions tailored for various specialized applications, such as rotating frames, porous media, or multi-phase flows, these are beyond the scope of this work and are not discussed further due to their limited relevance to the simulations presented in this thesis. The boundary conditions outlined here are carefully selected to meet the specific requirements of the studied cases (see Chapter 5, Chapter 6 and Chapter 7), ensuring accurate and efficient solutions.

2.5 Grid generation

In OpenFOAM, the grid generation plays a vital role in preparing the computational domain for the simulations. Two commonly used utilities, `blockMesh` and `snappyHexMesh`, provide structured and unstructured meshing capabilities, respectively [53]. `blockMesh` is designed for generating structured hexahedral meshes based on user-defined blocks. The geometry is divided into blocks, with each block specified by corner vertices in a Cartesian coordinate system. The mesh resolution is defined by specifying the number of cells along the principal directions, and physical boundary conditions are applied by labeling the boundaries. This utility is particularly effective for simple geometries such as rectangular or cylindrical domains, offering precise control over the mesh quality.

On the other hand, `snappyHexMesh` is used for generating unstructured, hexahedral-dominant meshes [53] for complex geometries. It starts with a coarse structured mesh, often generated using `blockMesh`, and refines the mesh based on the geometry, which is imported as STL or OBJ files. The utility snaps the mesh to the surface features of the geometry and allows for the addition of boundary layers near walls to enhance resolution. This makes `snappyHexMesh` suitable for intricate geometries such as aerodynamic shapes or porous media.

Both `blockMesh` and `snappyHexMesh` provide tools for assessing and improving mesh quality by evaluating parameters such as orthogonality, aspect ratio, and skewness using

`checkMesh`. Maintaining high mesh quality is crucial for ensuring numerical stability and accuracy in CFD simulations. Figure 2.1 shows an example of how a structured body-fitted grid can be obtained using `blockMesh` and `snappyHexMesh` utilities.

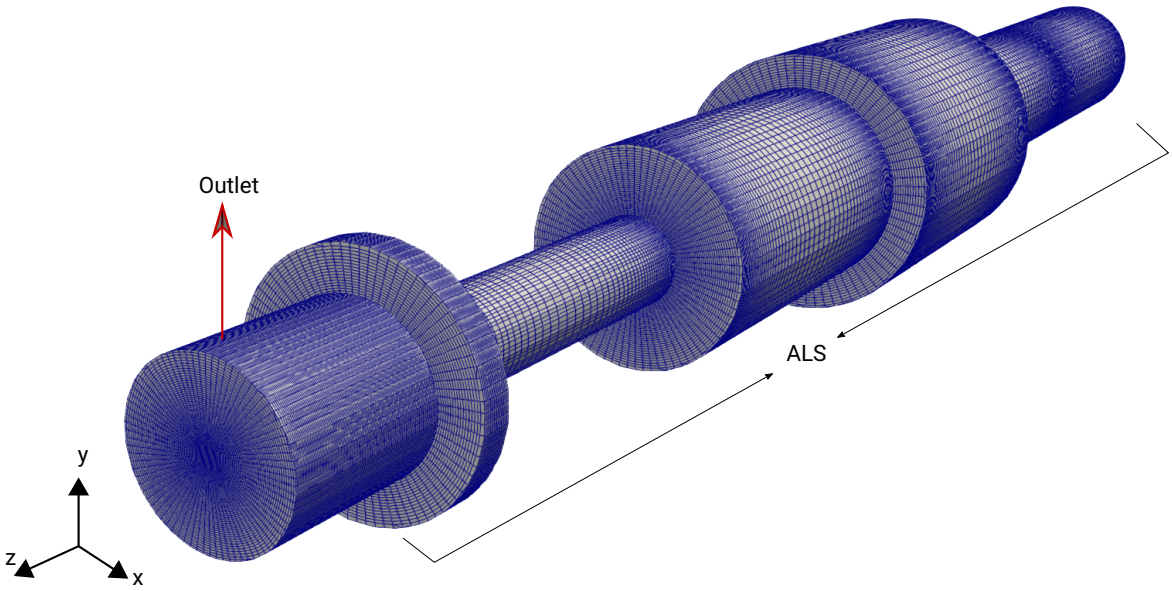

Fig. 2.1. Structured O-grid of an aerodynamic lens stack geometry [37] generated using the `blockMesh` and `snappyHexMesh` utility. A cylindrical block-structured grid was initially created using the `blockMesh` utility and later refined by snapping it onto the geometry of the ALS using the `snappyHexMesh` utility.

2.6 Parallelization in OpenFOAM

OpenFOAM achieves parallel execution using the Message Passing Interface (MPI) [53], allowing efficient computations on distributed-memory systems. The primary approach to parallelization is domain decomposition, where the computational domain is divided into multiple subdomains, each assigned to a separate processor. This decomposition is managed by the `decomposePar` utility, which partitions the mesh using different strategies to optimize computational load balancing and minimize inter-processor communication.

Among the available decomposition methods [53], the `simple` method divides the domain along user-specified Cartesian directions, making it suitable for block-structured meshes and cases where the workload is evenly distributed. The `hierarchical` method extends this approach by allowing multi-level decomposition, first splitting along a primary direction and then further subdividing the resulting sections, which is beneficial for complex geometries or parallel systems composed of different processor architectures. The `scotch` method, on the other hand, uses a graph-based algorithm to automatically balance the computational load while minimizing the processor communication, making it particularly effective for unstructured meshes and cases with highly non-uniform workloads. Additionally, OpenFOAM supports `manual` decomposition, where the user explicitly

defines the domain split via the `manualCoeffs` [53] entry in the `decomposeParDict`. This approach is useful for irregular geometries, processor-specific workloads, or optimization for specific hardware.

Once the domain is decomposed, each processor solves its assigned subdomain independently while exchanging interface data with neighboring subdomains via MPI. To maintain solution accuracy, OpenFOAM synchronizes information at subdomain boundaries using ghost cells, ensuring consistent flux calculations.

After the simulation, the individual subdomains are reconstructed into a single dataset using the `reconstructPar` utility, allowing for post-processing and visualization. With its efficient parallel implementation, OpenFOAM scales well across multiple processors [71, 72], making it well-suited for high-performance computing applications in computational fluid dynamics.

The various numerical methods and solver configurations discussed in this chapter are comprehensively compared and evaluated in Chapter 5. This evaluation examines their performance, accuracy, and computational efficiency under supersonic expanding flow conditions similar to those encountered in aerosol injector systems. Based on these comparisons, the final selection of methods employed in the simulations is justified. Furthermore, the complete solver settings (e.g., `fvSchemes` and `fvSolution`) are provided in Appendix A.

3 Modeling gas flows in rarefied and multiscale regimes[1]

Understanding gas flows in transitional and rarefied regimes is crucial for accurately modeling aerodynamic injection systems, vacuum-based processes, and nanoscale gas transport. In aerosol injection systems used for single-particle diffractive imaging (SPI), the molecular mean free path increases significantly as the flow expands from high-pressure conditions inside the injector to the near-vacuum environment of the experimental chamber [36]. For injectors operating at low inlet pressures, the overall flow often transitions into either a multiscale regime, where continuum and rarefied effects coexist, or a fully rarefied regime, where molecular interactions dominate. Accurately capturing such flow physics requires methods beyond traditional computational fluid dynamics (CFD) based on the Navier-Stokes equations.

For flows in the continuum regime ($Kn \ll 0.1$), the Navier-Stokes equations provide an effective description, and CFD solvers employing the finite-volume method (FVM) can resolve flow features with reasonable accuracy. However, as Kn increases beyond 0.1, the continuum assumption no longer holds true and further assumptions such as the local thermodynamic equilibrium and no-slip boundary conditions begin to break down. Extended continuum models, such as the Burnett equations and regularized moment equations, have been proposed to address this issue but are often numerically unstable and difficult to implement for complex flow configurations [75, 76].

To capture rarefied flow effects, several numerical approaches based on the kinetic theory of gases have been developed, each with specific advantages and limitations. The Direct Simulation Monte Carlo (DSMC) method [43] is a widely used stochastic approach that approximates the Boltzmann equation by simulating the motion and collisions of representative gas molecules. The method captures rarefied gas dynamics by tracking a statistical ensemble of simulation particles that undergo free molecular motion and probabilistic inter-molecular collisions. Through this process, macroscopic flow properties such as pressure, temperature, and velocities emerge naturally from molecular interactions. DSMC is particularly effective for rarefied flows ($Kn > 0.1$), as it inherently accounts for

[1] Certain components of this chapter are based on the publication: S. K. Peravali, V. Jafari, A. K. Samanta, J. Küpper, M. Amin, P. Neumann and M. Breuer, "Accuracy and performance evaluation of low density internal and external flow predictions using CFD and DSMC", *Computers & Fluids* **279**, 106346 (2024) [73] and S. K. Peravali, A. K. Samanta, M. Amin, P. Neumann, J. Küpper and M. Breuer, "An improved simulation methodology for nanoparticle injection through aerodynamic lens systems", *Physics of Fluids* **37** (3), 033380 (2025) [74]. I am the principal contributor to both publications. I contributed in drafting the original manuscripts and overseeing the review and editing processes. I was also deeply involved in the visualization and validation of data, the development and application of the methodology, and conducting the investigations. Additionally, I contributed in the formal analysis and conceptualization of the papers.

non-equilibrium effects, including velocity slip, temperature jumps, and strong translational and internal energy deviations from equilibrium distributions. Despite its accuracy in high-Kn number regimes, DSMC becomes computationally expensive as Kn decreases. The method's cost scales inversely with the Knudsen number ($\sim Kn^{-4}$) [44], meaning that in near-continuum or dense gas regions, resolving intermolecular collisions necessitates a prohibitively large number of simulated particles. This limitation makes DSMC inefficient for low-Kn number flows, where continuum-based approaches such as CFD based on the Navier-Stokes equations provide a more practical alternative.

Alternative approaches for solving the Boltzmann equation include deterministic methods such as the Discrete Velocity Method (DVM) [77, 78]. In DVM, the velocity space is discretized into a finite set of velocities, converting the Boltzmann equation into a system of PDEs for the distribution function at each discrete velocity. The transport term is handled using finite-difference or finite-volume schemes, while the collision term, which is often computationally the most demanding part, is evaluated through simplified models such as the Bhatnagar-Gross-Krook (BGK) model [79], the Shakhov model [80] or the Ellipsoidal-Statistical BGK (ES-BGK) model [81]. These models replace the full collision integral by a relaxation toward a local Maxwellian distribution over a characteristic timescale, significantly reducing the computational effort. While DVM avoids the statistical noise of stochastic methods like DSMC and offers accurate results in the transition regime, it suffers from high computational and memory requirements due to the need for fine resolution in the velocity space [82, 83], especially in multi-dimensional and highly non-equilibrium flows (e.g., shocks, expansions, ...) [84]. Moreover, like DSMC it becomes inefficient in the low-Knudsen number (near-continuum) regime due to requirement of grid sizes and timesteps smaller than the molecular mean free path and the mean collison time, respectively.

However, DSMC handles higher-order non-equilibrium effects naturally, as it simulates molecular interactions directly without relying on a discretized velocity space or approximate collision models. This makes DSMC particularly advantageous in capturing complex, high-Kn number flows with sharp gradients or strong anisotropy, such as those found in shocks or expansions [85, 86, 87, 88, 89], where deterministic solvers may struggle without adaptive grids or advanced modeling. Due to these advantages, and the availability of well-developed and mature open-source DSMC codes [90, 91], this study employs the DSMC method to model rarefied flows and flows in the transition regime.

This chapter presents an overview of the fundamental principles underlying the DSMC method, with a focus on the physical models employed to resolve rarefied flow regimes. It then describes the hybrid DSMC/CFD framework adopted in this work for accurately capturing multiscale gas dynamics. Finally, a literature review is provided to contextualize the present study within existing research and to underscore the advantages of the selected methodology.

3.1 DSMC method

The Direct Simulation Monte Carlo (DSMC) method is a discrete particle simulation technique that provides a numerical approximation to the solution of the Boltzmann equation:

$$\frac{\partial f}{\partial t} + \mathbf{u} \cdot \nabla f = \left(\frac{\partial f}{\partial t}\right)_{\text{coll}} . \tag{3.1}$$

Here, $f(\mathbf{x}, \mathbf{u}, t)$ is the gas distribution function which represents the probability density of finding a molecule at position $\mathbf{x}$, with velocity $\mathbf{u}$, at time t.

In the DSMC method, each particle represents a large ensemble of real gas molecules [43, 92] and their interactions. Both intermolecular and molecule-surface collisions are modeled probabilistically. The method solves the Boltzmann equation by decoupling the advection term $(\mathbf{u} \cdot \nabla f)$ from the collision term $\left(\frac{\partial f}{\partial t}\right)_{\text{coll}}$ (see Figure 3.1), treating them in successive steps [93].

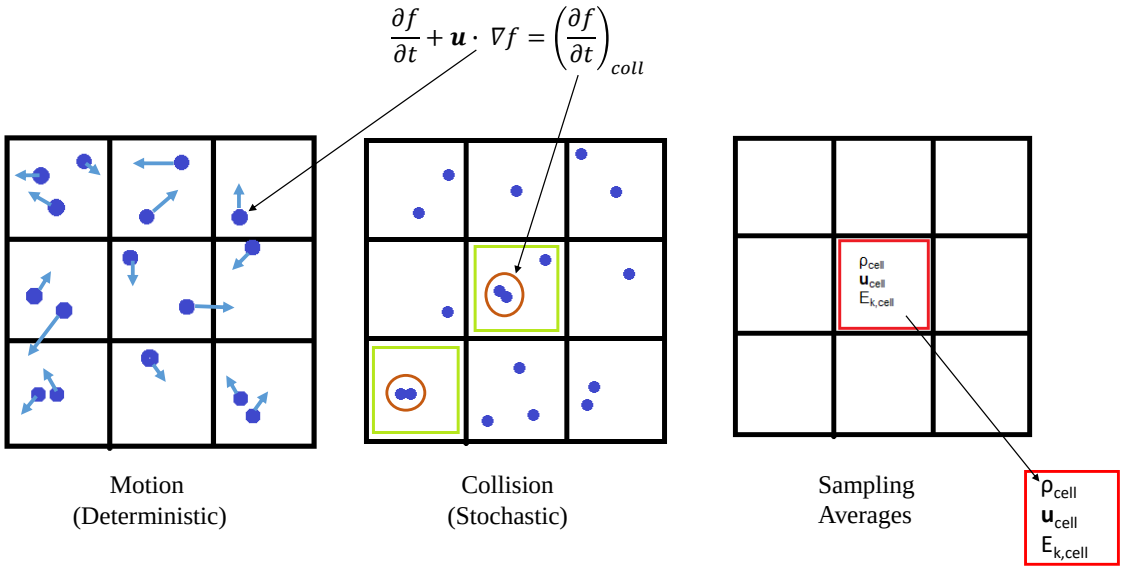

Fig. 3.1. A skematic sketch of the DSMC method.

The DSMC algorithm comprises the following steps:

1. **Domain discretization and initialization:** The computational domain is discretized into a grid of finite-sized cells. Each grid cell is populated with a certain number of simulation particles based on the initial flow conditions. Particle positions and velocities are typically initialized using a Maxwell-Boltzmann distribution.

2. **Particle movement:** Particles move through the grid deterministically (i.e., without collisions during this step, see Figure 3.1) according to their velocities over a time step Δt:

$$\mathbf{x}(t + \Delta t) = \mathbf{x}(t) + \mathbf{u}(t)\ \Delta t \tag{3.2}$$

   Here, $\mathbf{x}$ and $\mathbf{u}$ are the position and velocity vectors of the particle, respectively. Particles that cross cell boundaries are reassigned to the appropriate grid cell.

3. **Boundary interactions:** Particles interact with domain boundaries, including inflow/outflow and solid surfaces. Inlet boundaries introduce new particles, while outlet boundaries remove those exiting the domain. Reflections at walls are modeled using gas-surface interaction models, which are detailed in Section 3.2.

4. **Collision modeling:** Intermolecular collisions are handled stochastically using Monte Carlo methods. Candidate particle pairs are selected within each cell using a collision algorithm, and their post-collision velocities and positions are updated based on the chosen molecular interaction model. Details are discussed in Section 3.3.

5. **Sampling and averaging:** Macroscopic flow quantities such as number density, velocity, temperature, and pressure, are obtained by averaging microscopic particle data within each grid cell. This process is described in Section 3.4.

Steps 2 through 5 are repeated over successive time steps until the simulation reaches the desired end time. The accuracy of the DSMC method depends on several key parameters, including the number of particles per cell, the cell size relative to the mean free path, the selected time step, and the collision model used. The sensitivity of these parameters for low-density flows is evaluated in Chapter 5.

In this study, the SPARTA (Stochastic PArallel Rarefied-gas Time-accurate Analyzer) DSMC code [90] is employed to simulate transitional and rarefied gas flows. SPARTA is a high-performance, extensively benchmarked tool [94] capable of simulating systems with particle counts ranging from a few thousand to billions. It is optimized for parallel computing, offering excellent scalability and efficient memory usage [95]. SPARTA provides a comprehensive set of models to accurately capture gas dynamics in high-Knudsen-number regimes, including various molecular collision models, boundary condition formulations, and chemistry models for reactive flows. The following sections describe the boundary condition and collision models employed in this study.

3.2 Boundary conditions

The boundary conditions in DSMC can be classified in two types: Free-stream boundary conditions (inlet and outlet) and wall boundary conditions, where the gas-surface interactions are predominant. The inlet boundary condition introduces simulation particles into the computational domain by generating an influx through the designated boundary face at each time step. For every grid cell, whose face is aligned with the inlet boundary, the

molecular flux per unit area and per unit time, also referred to as the inward number flux $\dot{N}_i$, is calculated using the expression derived from the kinetic gas theory [43]:

$$\dot{N}_i = \frac{n}{\beta\ 2\pi^{\frac{1}{2}}} \left[\exp(-s^2\cos^2\phi + \pi^{\frac{1}{2}} s\cos\phi\{1+\mathrm{erf}(s\cos\phi)\}\right] \tag{3.3}$$

Here, n is the number density, β is the reciprocal of the most probable thermal speed $\sqrt{m/(2k_BT)}$, where m is the molecular mass, T is the temperature and k_B is the Boltzmann constant. The molecular speed ratio is given by $s = \beta|\mathbf{U}|$ where $\mathbf{U}$ is the free-stream velocity and ϕ is the angle between the free-stream velocity $\mathbf{U}$ and the unit normal vector $\mathbf{e}$ to the surface element [43]. This formulation allows accurate computation of the number of particles injected across the inlet boundary, based on local flow conditions (e.g., number density, streaming velocity, thermal temperature, ...), while preserving mass and momentum fluxes in accordance with the kinetic theory. The outlet boundary condition acts as a vacuum sink, removing simulation particles that exit the computational domain. Gas-surface interactions must be used for wall boundaries. This boundary condition can be modeled by two types of interactions: Specular and diffusive reflections. In the specular case, the particle is reflected elastically where its velocity component normal to the surface is reversed. In the diffuse case, the post-interaction velocity of a particle striking a thermal wall is sampled from a Maxwellian distribution corresponding to the wall temperature, with both the speed and direction governed by this distribution. The normal velocity component u is calculated using [90, 92, 96]:

$$u = (-\ln(R_f))^{\frac{1}{2}}/\beta, \tag{3.4}$$

where R_f is a random fraction between 0 and 1. To compute the tangential velocity components v and w (which lie in the plane tangent to the wall surface), a pair of independent random fractions is used to calculate the magnitude of the tangential velocity V_r and the angular coordinate θ [96]:

$$V_r = (-\ln(R_f))^{\frac{1}{2}}/\beta \quad \text{and} \quad \theta = 2\pi R_f\ . \tag{3.5}$$

The tangential components are then obtained by projecting V_r onto two orthogonal directions in the surface plane:

$$v = V_r\cos\theta \quad \text{and} \quad w = V_r\sin\theta\ . \tag{3.6}$$

In the diffusive interaction model described above, it is assumed that the incident gas molecules undergo a complete energy accommodation upon colliding with the surface. This means the molecules are fully thermalized by the surface, and their post-collision velocities are sampled from a Maxwellian distribution corresponding to the surface temperature, regardless of their incoming energy.

However, in many practical scenarios, especially with limited interaction time or specific surface properties, only a partial energy accommodation occurs. In such cases, only a

fraction of the energy is exchanged during the collision. This is quantified based on a parameter called thermal accommodation coefficient α_E, which is traditionally defined as:

$$\alpha_E = \frac{E_i - E_r}{E_i - E_w} \,, \tag{3.7}$$

where E_i is the incident energy per molecule, E_r is the reflected energy per molecule and E_w is the energy per molecule corresponding to the fully diffuse reflection with the equilibrium temperature of the reflected gas T_r equal to the equilibrium temperature of the surface T_w. If $\alpha_E = 0$ the gas reflection leads to a perfectly elastic gas-surface. Conversely, $\alpha_E = 1$, means a fully inelastic collision, in which the molecule is completely thermalized to the wall temperature. The accommodation coefficients can also be defined for the normal and tangential components of momentum and energy [43, 92].

The Maxwellian gas–surface interaction model (Figure 3.2 (a)) accounts for the accommodation coefficient defined in Eq. (3.7) by assuming that a fraction ϵ of the incident molecules is scattered diffusely, while the remaining part $(1 - \epsilon)$ is reflected specularly. Here, ϵ is typically taken to be equivalent to the thermal accommodation coefficient α_E. This combination of specular and diffuse reflections provides a simple and computationally efficient framework for modeling gas–surface interactions. While this model is effective in describing the thermodynamic behavior of the gas, it fails to capture the detailed molecular-level behavior often observed in gas–surface scattering experiments [97]. Moreover, it does not account for the internal energy exchange with the surface and lacks the flexibility to control the angular scattering distribution.

The Cercignani-Lampis model (CL) [98, 99] is based on the assumption that there is no coupling between the normal and tangential velocity components during gas-molecule reflections from a surface unlike the Maxwellian model. Therefore, this model uses two coefficients α_n and α_t, which represent energy accommodation coefficients associated with the normal and tangential components of the velocity, respectively. The scattering distribution of the molecules is centered around an average scattering angle $\overline{\theta}_r$, which is a function of the above two accommodation coefficients. This scattering distribution has a lobular shape similar to the one observed in the experiments [97]. This model was applied in DSMC by Lord [99]. The algorithmic expressions of the CL (Cercignani–Lampis) gas-surface interaction model are given as follows. The reflected tangential velocity components v_r and w_r are computed as [92]:

$$v_r = \frac{1}{\beta}\left[\overline{v}_r + \sqrt{-\alpha_t \ln R_{f,1}}\cos(2\pi R_{f,2})\right], \tag{3.8}$$

$$w_r = \frac{1}{\beta}\sqrt{-\alpha_t \ln R_{f,1}}\sin(2\pi R_{f,2}), \tag{3.9}$$

where $\overline{v}_r = \sqrt{1-\alpha_t}\, v_i$ is the mean reflected tangential velocity based on the incident velocity v_i, and α_t is the tangential momentum accommodation coefficient. $R_{f,1}$ and $R_{f,2}$ are independent random numbers uniformly distributed between 0 and 1.

The reflected normal velocity u_r is evaluated using:

$$u_r = \frac{1}{\beta}\sqrt{\overline{u}_r^2 + 2\overline{u}_r\sqrt{-\alpha_n \ln R_{f,3}}\cos(2\pi R_{f,4}) - \alpha_n \ln R_{f,3}}\ , \tag{3.10}$$

where $\overline{u}_r = \sqrt{1-\alpha_n}\,u_i$, is the mean reflected normal velocity based on u_i being the incident normal velocity. $R_{f,3}$ and $R_{f,4}$ are also uniformly distributed random fractions between 0 and 1.

The full derivation of the above CL algorithm is provided in Shen [92]. Later, Lord [100, 101] extended the CL model [98] to the CLL model (Cercignani-Lampi-Lord) accounting for the internal energy exchange by introducing accommodation coefficients for rotational and vibrational modes. Another key advantage of this model is the capability to produce diffuse scattering with incomplete energy accommodation ($\alpha_E = \alpha_n = \alpha_t < 1$). This model is illustrated in Figure 3.2 (b).

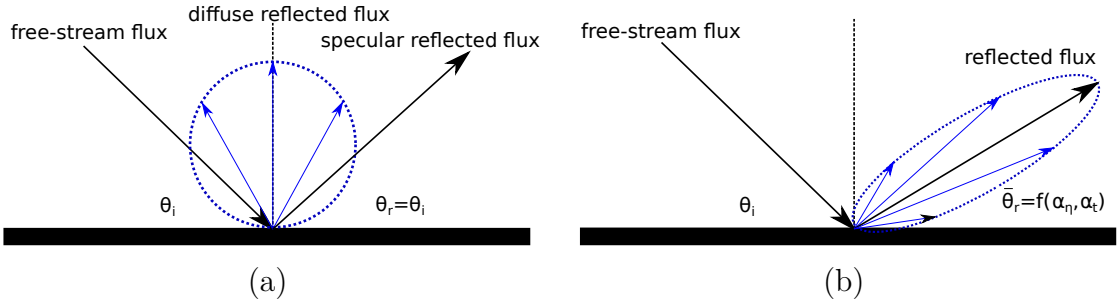

Fig. 3.2. Schematic diagrams of the (a) Maxwell model and (b) the CLL model.

Furthermore, this model enables the control over the angular scattering distribution through an eccentricity parameter (*eccen*). This makes the model particularly useful in simulating cases such as adiabatic walls (see Section 5.4.4), where gas-surface interactions are purely elastic yet isotropic. By setting $\alpha_E = \alpha_n = \alpha_t = 0$, a perfectly elastic reflection is ensured, and by choosing *eccen* $= 0$, the reflected particles exhibit isotropic scattering. While the CLL model introduces additional computational complexity due to its sampling procedures, it remains a widely used and physically accurate choice for rarefied gas flow simulations involving gas-surface interactions.

In Chapter 5, a detailed evaluation of the gas–surface interaction models, including the CLL and Maxwellian reflection approaches, is conducted across different flow scenarios to assess their impact on the simulation accuracy and physical realism.

3.3 Inter-particle collision models

Several collision sampling schemes are available in the DSMC method to model interactions between simulation particles. SPARTA employs Bird's No-Time-Counter (NTC) method [43], which is one of the most widely used and computationally efficient collision

algorithms in DSMC simulations. The computational cost of the NTC method is dictated by the number of simulated particles and this method ensures that the correct collision rate is maintained while preserving the statistical accuracy of molecular interactions [96]. In this scheme the number of collision pairs N_{coll} in a cell over the time step Δt is given by:

$$N_{coll} = \frac{1}{2}\frac{N\ (N-1)\ F_N\ (\sigma_t\ c_r)_{max}\ \Delta t}{V_c} \tag{3.11}$$

where N is the number of particles in the cell, F_N is the number of real molecules represented by each particle, $(\sigma_t\ c_r)$ is the product of total collision cross-section σ_t and the relative particle velocity c_r and V_c is the volume of the cell. Random collision pairs are selected at each cell per time step and a collision pair is chosen based on an acceptance-rejection procedure, i.e., if the condition in Equation (3.12) is met, then the collision between the pair is performed.

$$\frac{\sigma_t\ c_r}{(\sigma_t\ c_r)_{max}} > R_f. \tag{3.12}$$

In a DSMC simulation of a homogeneous gas, the probability of a collision of two molecules is proportional to the product of the total collision cross-section σ_t and the relative speed between the colliding molecules c_r. The differential cross-section σ is defined as [92, p. 70]:

$$\sigma = \frac{b}{\sin\chi}\left|\frac{db}{d\chi}\right|. \tag{3.13}$$

Here b is the minimum distance between the initial trajectories of two approaching molecules in the center-of-mass framework, prior to any influence from intermolecular forces. χ is the deflection angle of the relative velocity. The total collision cross-section is then defined as [92, p. 71]:

$$\sigma_t = 2\pi\int_0^{\pi}\sigma\sin\chi\,d\chi = 2\pi\int b\,db \tag{3.14}$$

The parameter b is given by a molecular model. In the present study, two molecular models, the Variable Hard Sphere (VHS) model and the Variable Soft Sphere (VSS) model, are used in the simulations.

3.3.1 Variable Hard Sphere (VHS) model

The VHS molecular diameter d_{VHS} is defined as [92]:

$$d_{VHS} = \left[\frac{(15/8)(m/\pi)^{1/2}(k_B\ T_{ref})^{\omega}}{\Gamma((9/2)-\omega)\ \mu_{ref}\ \epsilon_t^{\omega-(1/2)}}\right]^{1/2} \tag{3.15}$$

where μ_{ref} and T_{ref} are the reference viscosity and reference temperature, respectively. ω is the power exponent of the temperature in the viscosity law, ϵ_t is the relative mean

kinetic energy, m is the molecular mass and Γ is the Gamma function. The parameter b is calculated from d_{VHS} and the deflection angle χ as:

$$b = d_{VHS} \cos\left(\frac{1}{2}\chi\right). \tag{3.16}$$

3.3.2 Variable Soft Sphere (VSS) model

For flows where the molecular diffusion plays an important role, the VSS model is preferred to the VHS model [102]. In this model, the molecular diameter is defined by [92]:

$$d_{VSS} = \left[\frac{5(\alpha+1)(\alpha+2)(m/\pi)^{1/2}(k_B\, T_{ref})^{\omega}}{16\alpha\ \Gamma((9/2)-\omega)\ \mu_{ref}\ \epsilon_t^{\omega-(1/2)}}\right]^{1/2}. \tag{3.17}$$

The parameter b in this model is calculated as:

$$b = d_{VSS}^{\alpha} \cos\left(\frac{1}{2}\chi\right), \tag{3.18}$$

where α is the scattering coefficient and is related to the Schmidt number S_c:

$$\alpha = \frac{10}{S_c\ (21-6\omega)-5}. \tag{3.19}$$

The choice of the collision model is case-dependent. In Chapter 5, both the VHS and VSS models are evaluated in terms of simulation accuracy and computational performance.

3.3.3 Energy exchange models

The molecular collisions can be either elastic where there is no energy exchange between energy modes, and inelastic where the energy is exchanged between translational and internal energy modes. Due to the enormous number of collisions in the DSMC simulation, using the traditional models like dual repulsive centers, the sphero-cylindrical model, the rough sphere model and the harmonic oscillator model for internal energy modeling is impractical, primarily because of their high computational costs [92]. Larsen and Borgnakke [103, 104] introduced a phenomenological model that can be used to simulate the energy exchange between the molecules. In this model, the total energy (kinetic + internal) is assumed to be conserved. The translational and internal energy (post collision) are sampled according to the equilibrium distributions of the total energy. The equilibrium energy distribution function for a specified number of degrees of freedom is given by [96]:

$$f(E) = \frac{1}{\Gamma(\xi/2)}\left(\frac{E}{k_BT}\right)^{\frac{\xi}{2}-1} \exp\left(\frac{-E}{k_BT}\right), \tag{3.20}$$

where $f(E)$ is the probability of occurrence of E, ξ is the degree of freedom, k_B is the Boltzmann constant and T is the temperature. For mono-atomic and diatomic gases –

where the rotational degree of freedom $\xi_{rot} \leq 2$ – the internal energy can be computed by sampling a random fraction R_f according to:

$$E = -\ln(R_f) k_B T. \tag{3.21}$$

For polyatomic gas species where $\xi_{rot} > 2$, the internal energy is then sampled using the acceptance-rejection method from the distribution function shown in Equation (3.20).
In this model, only a fraction of collisions is assumed to be inelastic, which is defined by an average probability of internal energy exchange ϕ. This parameter is used to determine the rate of relaxation process of the energy, which can also be given as the inverse of the relaxation collision number Z ($\phi = 1/Z$). The relaxation collision number is defined as [92, 105]:

$$Z = \frac{\tau_i}{\tau_t}. \tag{3.22}$$

Here τ_i is the relaxation time and τ_t is the mean collision time. SPARTA uses the Larsen and Borgnakke (L-B) model with constant or variable relaxation. The variable rotational relaxation model in SPARTA is described in Section 3.3.3.1. The collision parameters used in the simulations are tabulated in Table 3.1. In the current study, the vibrational mode and chemical reactions are assumed to be frozen and the impact of different relaxation models on simulation accuracy and performance is systematically assessed in Chapter 5.

Gas	Molecular diameter	ω	T_{ref}	α	ξ_{rot}	ϕ_{rot}
N2	4.07e-10 m	0.74	273.15	1.36	2	0.2
He	2.33e-10 m	0.66	273.15	1.26	0	0

Tab. 3.1. Collision model parameters of simulated gas molecules [96, 106].

3.3.3.1 Variable relaxation model

In the variable relaxation L-B model in SPARTA, ϕ is computed in the following way:

$$\phi_{rot} = \frac{1}{Z_{rot}} = \frac{1 + \frac{\pi^{3/2}}{2}\left(\frac{T^*}{T}\right)^{1/2} + \left(\frac{\pi^2}{4} + \pi\right)\frac{T^*}{T}}{Z_{rot,\infty}}, \tag{3.23}$$

where T^* is the characteristic temperature of the intermolecular potential and $Z_{rot,\infty}$ is the limiting value of the rotational relaxation number. T is extracted from the total energy E_c [96]:

$$T = \frac{2E_c}{k_B\left(5 - 2\omega + \xi_{rot}\right)}. \tag{3.24}$$

Here $5 - 2\omega$ is the translational degree of freedom.

The terms T^* and $Z_{rot,\infty}$ are unknowns in Eq. (3.23), which are inferred from different experiments. For air, Parker [107] employed Eq. (3.23) with $Z_{rot,\infty} = 15.7$ and $T^* = 80.0$ K. Lordi and Mates [108] fitted their experimental data to Eq. (3.23) and obtained

$Z_{rot,\infty} = 23.0$ and $T^* = 91.5$ K. Both models can be used for temperature ranges from 0 to 1200 K .

3.4 Sampling flow data

Macroscopic flow properties, such as number density, pressure, velocity, and temperature, are obtained by averaging microscopic particle data within each computational cell at specified sampling intervals [96]. The following quantities are sampled in the present study:

- **Number density n:**

$$n = \frac{F_N \cdot N}{V_c} \ , \tag{3.25}$$

  where F_N is the number of real molecules represented per simulation particle, N is the number of particles in the cell, and V_c is the cell volume.

- **Flow velocity components u, v, w:**

$$u = \frac{\sum_i^N m_i u_{p,i}}{\sum_i^N m_i} \tag{3.26}$$

  where $u_{p,i}$ is the x-component of the velocity of the i-th particle, and m_i is its mass. The v and w components (in y and z directions) are calculated analogously.

- **Translational temperature T:**

  First, the thermal velocity of each particle is calculated as the deviation from the cell-averaged flow velocity:

$$\mathbf{C}_i = \mathbf{u}_{p,i} - \mathbf{u} \tag{3.27}$$

  The translational temperature is then computed from the mean kinetic energy of thermal motion:

$$T = \frac{1}{3Nk_B} \sum_i^N m_i |\mathbf{C}_i|^2 \tag{3.28}$$

- **Rotational temperature T_{rot}:**

$$T_{\mathrm{rot}} = \frac{2}{k_B} \cdot \frac{\sum_i^N E_{\mathrm{rot},i}}{\sum_i^N \xi_{rot,i}} \tag{3.29}$$

  where $E_{\mathrm{rot},i}$ is the rotational energy (see Eq. (3.21)) of the i-th particle, and $\xi_{rot,i}$ is its rotational degree of freedom.

- **Pressure p:** The pressure is calculated using the ideal gas relation:

$$p = nk_BT \ . \tag{3.30}$$

To reduce statistical fluctuations, the sampled macroscopic quantities are further time-averaged after the simulation reaches steady state. In this study, a minimum of 1000 steady-state time snapshots are averaged to ensure reliable macroscopic estimates from the DSMC simulation.

3.5 Hybrid DSMC/CFD

The DSMC method has been demonstrated to effectively resolve rarefied flows [96]. However, for low Knudsen number regimes, DSMC becomes computationally expensive due to the drastic increase in molecular collisions. Additionally, statistical noise can become significant, particularly in low-speed regions of the flow, requiring extensive averaging to obtain accurate macroscopic properties [109]. In contrast, Navier-Stokes-based CFD solvers efficiently resolve continuum flow regimes with high accuracy and efficiency.

For multiscale flows, where the Knudsen number varies across the computational domain – spanning continuum, transitional, and free-molecular flow regimes – a hybrid DSMC/CFD approach is efficient. This method ensures that CFD is applied in regions where the continuum assumption holds, while DSMC is used in rarefied regions (see Figure 1.2). The key to effective coupling is defining a continuum breakdown criterion, which determines the regions where DSMC must be applied.

Once the computational domain is divided, information exchange between the CFD and DSMC regions must be carefully handled. Coupling strategies fall into two main categories: one-way and two-way coupling. In one-way coupling, macroscopic properties such as density, velocity, and temperature are transferred from CFD to DSMC without any feedback. This approach is computationally efficient and suitable when the rarefied region does not significantly influence the overall flow. Conversely, two-way coupling involves bidirectional exchange of information, where rarefied effects modify the continuum region. This method is essential when rarefaction strongly influences global flow properties and ensures a self-consistent solution across both regimes.

The implementation of coupling can further be classified as either state-based or flux-based. In state-based coupling, each region extends slightly beyond the interface into buffer cells (see Figure 3.3), where the macroscopic properties are computed independently for each region. Specifically, the particle-averaged values from the rarefied region serve as the macroscopic boundary conditions in the buffer cells of the continuum region, while the continuum region's macroscopic properties are used to generate particles in the buffer cells of the rarefied region. This method allows each solver to determine the fluxes across the interface (i.e., the flux across the cell face) on its own, ensuring inherent conservation of mass, momentum, and energy.

In contrast, flux-based coupling shown in Figure 3.4 matches the integrated fluxes of mass, momentum, and energy directly at the interface. This approach tends to be less sensitive to mismatches in grid resolution or solver specifics because it transfers information in the form of integrated quantities rather than relying on matching of state values at individual grid points. Such robustness is particularly advantageous when coupling solvers that operate on different scales or resolutions – for example, OpenFOAM's body-fitted

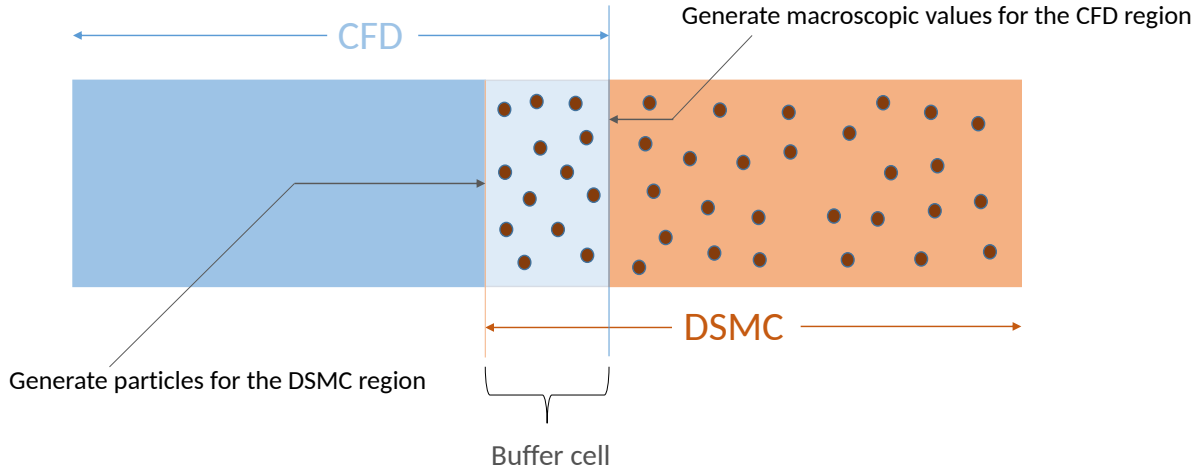

Fig. 3.3. State-based coupling.

grid with SPARTA's Cartesian grid – ensuring a more consistent and conservative transfer of information across the interface.

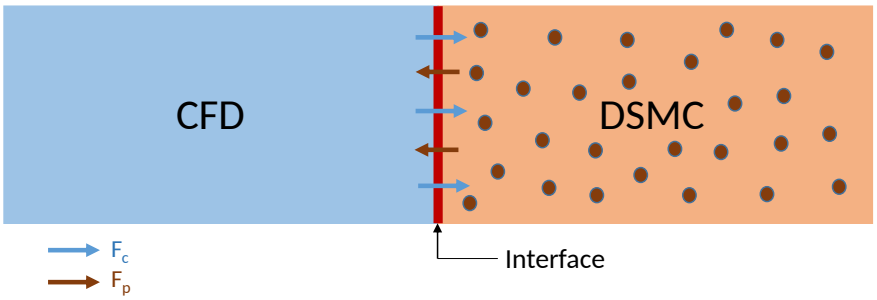

Fig. 3.4. Flux based coupling (F_c and F_p are the flux from the continuum domain and the DSMC domain, respectively.).

The selection between state-based and flux-based coupling depends on the specific simulation requirements. When the grid resolutions on both sides are comparable and a two-way coupling is necessary, state-based coupling is preferred, as macroscopic properties (e.g., density, velocity, and temperature) can be directly exchanged. This method is particularly advantageous over flux-based coupling because flux quantities from the DSMC region can exhibit high statistical fluctuations, especially near the continuum regime [109].

In contrast, flux-based coupling is more practical for one-way coupling, particularly when the grid resolutions of the CFD and DSMC domains differ significantly. Although flux-based coupling may introduce additional statistical noise, it has been successfully implemented in various hybrid DSMC/CFD frameworks. For instance, a one-dimensional flux-based hybrid solver was initially developed for shock-wave problems [110] and later extended to two dimensions for rarefied slit flows [111]. Additionally, flux-based coupling has been applied to a range of problems, including planar Couette flow under different

interface conditions [112], hypersonic rarefied flow over blunt bodies [113], and high-speed nozzle expansions into vacuum [114].

For gas flows inside aerosol injectors used in SPI experiments, where rarefaction primarily results from gas expansion and backflow is negligible, the influence of the rarefied region on the overall flow is minimal. Consequently, a one-way flux-based coupling approach is adopted in this study to ensure computational efficiency while maintaining accuracy. In this context, the statistical fluctuations typically associated with flux quantities from DSMC are of lesser concern, as the coupling is unidirectional and does not affect the upstream continuum domain.

Various breakdown parameters have been proposed to determine the validity of the continuum assumption in hybrid solvers. The most notable among them are described as follows:

- **Knudsen number** Kn: By definition the Knudsen number is the ratio of the mean free path λ to a characteristic length L. The continuum breakdown occurs in those computational regions where $Kn > 0.1$. However, because Kn is typically defined as a global parameter for the entire flow domain, it may not capture critical local variations that can significantly affect the flow properties.

- **Chapman-Enskog parameter** $\Gamma(\mathbf{C})$: This parameter serves as an accurate predictor of non-continuum conditions [115] and is defined as:

$$\Gamma(\mathbf{C}) = 1 + (\hat{\mathbf{J}} \cdot \mathbf{C}) \left(\frac{2}{5} \mathbf{C} \cdot \mathbf{C} - 1 \right) - (\mathbf{C} \cdot \hat{\tau} \cdot \mathbf{C}) \tag{3.31}$$

  Here, $\mathbf{C} = \beta \mathbf{c}'$ is the non-dimensional thermal velocity with $\mathbf{c}'$ being the thermal velocity and β the reciprocal of the most probable speed. Furthermore, $\hat{\mathbf{J}} = \frac{2}{p} \beta \mathbf{J}$ is the non-dimensional heat flux vector, and $\hat{\tau} = \frac{\tau}{p}$ is the non-dimensional viscous stress tensor. When Γ deviates substantially from unity, it indicates that the underlying assumptions of continuum mechanics no longer hold, and that non-equilibrium effects are dominating the system's behavior. Evaluating Γ is challenging because it depends on the thermal velocity $\mathbf{c}'$ of the particles. In practice, one must compute either an average or a maximum value of Γ over the full distribution function of particle velocities, which can be computationally expensive [116]. This difficulty has motivated the development of simpler, more efficient parameters, which are described in the following.

- **Bird's paramater** P: Bird's parameter [117] represents the ratio between the Lagrangian mean free path, and the characteristic macroscopic length scale, such as the density gradient length. It is typically defined for steady flows as:

$$P = \frac{\lambda}{\rho} \sqrt{\frac{m}{2 k_B T}} \left| \mathbf{u} \cdot \nabla \rho \right| . \tag{3.32}$$

  When $P > 0.04$, the flow regime is generally no longer considered as a continuum. Although derived from DSMC computations [117] and validated on expanding flows

(free jets) [118], an evaluation study for hypersonic flows over a blunt body [119] revealed that Bird's parameter fails to predict continuum breakdown near body surfaces. Moreover, it does not incorporate local flow variables beyond the density.

- **Boyd's Gradient-Length-Local Knudsen number** $Kn_{GLL,Q}$: In order to account for the local effects which the global Knudsen number cannot capture and the failure of Bird's parameter in near-wall regions, Boyd [116] proposed a local Knudsen number $Kn_{GLL,Q}$, which is defined as:

$$Kn_{GLL,Q} = \lambda \left| \frac{\nabla Q}{Q} \right|. \tag{3.33}$$

When $Kn_{GLL,Q} > 0.05$ the continuum breakdown is assumed. This criterion was found to be effective in predicting continuum breakdown in the shock wave near the surface of the body in hypersonic flows [119] and was further evaluated on hypersonic interaction flows [120]. These studies showed that the maximum of the local Knudsen number based on density $Kn_{GLL,\rho}$, temperature $Kn_{GLL,T}$ and velocity $Kn_{GLL,|\mathbf{v}|}$ accurately predicts the continuum breakdown near the surface and in the free-stream.

To capture both global and local rarefaction effects, a composite breakdown Knudsen number Kn_B is computed as the maximum of the global Knudsen number and the local Knudsen numbers:

$$Kn_B = \max(Kn, Kn_{GLL,\rho}, Kn_{GLL,T}, Kn_{GLL,|\mathbf{v}|}). \tag{3.34}$$

This composite parameter has been demonstrated to be effective for expanding flows in gas dynamic nozzles [87, 121], which are analogous to the flow conditions encountered in SPI experiments.

The hybrid DSMC/CFD framework in this work is implemented in the following way: The flow is initially simulated using CFD (Navier-Stokes eq.) and the continuum breakdown criterion Kn_B is evaluated. Based on this criterion, the former computational domain is split into CFD and DSMC regions using an interface. At the interface, the CFD solution data – obtained on a body-fitted grid – are interpolated onto the corresponding cell faces of the regular Cartesian grid that defines the interface. This mapping of flow variables (such as velocity, pressure, and temperature) is then used to generate the required inflow molecular flux per unit time [43] for the DSMC domain to simulate the rarefied region. The DSMC solution is sampled as described in Section 3.4 to extract macroscopic information, e.g., velocity, pressure and temperature, of the flow and the statistical noise is filtered out. The steady-state solution of the flow from both CFD using a body-fitted grid, and DSMC using a Cartesian grid, are then interpolated in their specific regions onto a regular Cartesian grid, see Figure 3.5, to have a smoothed contiguous multiscale flow field. The cell size of this regular Cartesian grid is typically chosen to be in the order of the minimum mean free path λ_{min}, observed throughout the computational domain.

This coupling strategy ensures computational efficiency while maintaining accuracy in regions of rarefaction. The validation of the hybrid method for a gas-dynamic nozzle flow, including comparisons with experimental data, is discussed in Chapter 5.

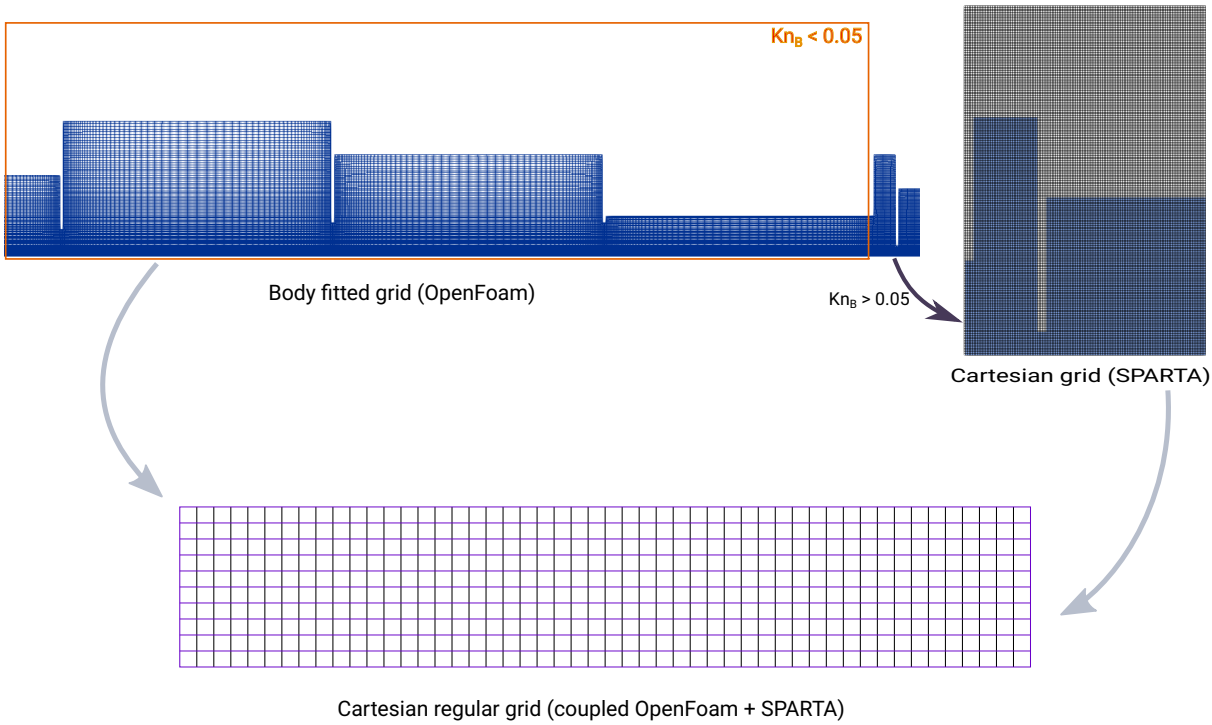

Fig. 3.5. Schematic diagram showing the hybrid DSMC/CFD coupling.

3.6 State-of-the art and open issues

Numerous studies were performed to analyze gas flow fields, including rarefied and continuum flows, most of them using DSMC or CFD methods. This section provides a brief summary of the literature, which cannot be comprehensive but primarily presents studies that depict specific aspects relevant to the study on multiscale/rarefied simulations – yet collectively demonstrate remaining open questions in the field.

The majority of studies focused on the accuracy and parameter investigations of DSMC simulations such as the choice of the mesh or the collision model [103, 104, 106, 122, 123, 124] and validated the results partially against experimental results. Some studies were related to more practical cases for engineering purposes [85, 86, 87, 88, 89, 120, 125]. Since the DSMC method can be very time consuming, many studies targeted the performance of the approach: While the computational performance of the DSMC method on different computer architectures in terms of runtime is discussed in [95, 126, 127, 128, 129], algorithms and optimizations to speed up the DSMC method can be found in [130, 131, 132, 133]. To the author's knowledge, energy consumption has not been addressed so far. Discussions on the impact of the mesh dependency, collision model and boundary conditions are not included in the aforementioned works.

Flows through micro-nozzles were studied based on DSMC and a compressible Navier-Stokes solver applying slip and no-slip conditions [87]. The computational results are compared and the most important outcome is that a better agreement between DSMC and CFD is observed when a slip-wall boundary condition is implemented. It is also shown that the CFD and DSMC results differ in the divergent parts of the nozzle, especially close to the outflow, where the Knudsen number Kn is relatively high or, in other words, strong rarefied effects start to appear. No evaluation of the results with regard to a comparison with experimental findings or computational expenses are included. The effect of different parameters such as inlet and wall boundary conditions and the Reynolds number on DSMC and Navier–Stokes approaches for a micro-nozzle flow with a relatively small Knudsen numbers was studied [88]. Furthermore, it was investigated in which part of the micro-nozzle DSMC and CFD provide the best results. It is shown that the CFD results exhibit obvious deviations from the DSMC results as Kn exceeds 0.045. The computational performance of large-scale parallel DSMC on homogeneous (CPU) and heterogeneous (CPU+GPU) systems was studied and different programming approaches (MPI, hybrid MPI+OpenMP and OpenACC) were discussed [131].

Extensive research on the development of hybrid DSMC/CFD methods was carried out, c.f. [85, 120, 125, 134, 135, 136, 137, 138, 139]. With regard to their application, simulation cases were mostly very specific, and the comparison was focused typically either on numerical accuracy [85, 120, 125, 137, 138, 139, 140] or on performance [134]. For example, the advantages of a hybrid DSMC/CFD approach over pure DSMC is indicated in [120]. For this purpose, the authors simulate a hypersonic flow over a two-dimensional wedge. A comparison of the flow field predicted by a 3D DSMC/CFD simulation considering a space capsule geometry is given in [125], including a validation against experimental results from wind tunnel tests. The study also investigates the effect of the mesh dependency on CFD and DSMC methods. A comparison study [85] explores the performance difference between coupled DSMC/CFD and pure CFD methodologies in simulating a gas centrifuge handling $^{235}UF_6$ gas. Pure DSMC results around the Mars pathfinder and Mars micro-probe capsules are studied in [89], however, without a validation against experimental results. Computational efficiency of massively parallel (stand-alone) DSMC for different cases is studied, amongst others, in [95] and [126]. Another comparison study between DSMC and CFD results of a low-density nozzle flow and the experimental evaluation is discussed in [105].

The accuracy of a DSMC simulation depends on a number of numerical parameters such as the time step size, the cell size, and the number of samples. Furthermore, the choice of the collision model plays an important role. An analysis of (statistical and deterministic) numerical errors corresponding to numerical parameters in the DSMC method is provided in [141] based on a simple heat transfer problem between two parallel plates in 1D and 2D. The statistical error analysis of the DSMC method applied to hypersonic and nozzle flows is provided in [142]. A further error analysis considering various numerical parameters (sampling cells, sampling time step and sample sizes) is provided in [143].

Despite these extensive studies, several open questions remain regarding the optimal implementation of pure DSMC and hybrid DSMC/CFD methods. Table 3.2 summarizes which related studies addressed different aspects of DSMC/CFD simulations in terms of

accuracy and computational performance, and classifies the work presented in Chapter 5. This chapter introduces a new study that systematically evaluates these unresolved issues, providing detailed insights into the hybrid simulation framework. The summary also offers practical recommendations on DSMC, CFD, and hybrid methods, along with guidelines for calibrating DSMC parameters that critically influence simulation accuracy and efficiency. The validated hybrid framework is subsequently applied to simulate aerosol injection systems for SPI, as described in Chapter 6 and Chapter 7.

Work	**CM**[a]	Kn	**GSI**[b]	**Run-Time**	**EC**[c]	**Validation**
Boyd [116]		✓				✓
Wang and Boyd [120]		✓				
Glass and Horvath [125]		✓				✓
Ghazanfari et al. [85]		✓				
Gallis et al. [128]	✓	✓		✓		
Plimpton et al. [126]				✓		✓
Li et al. [131]				✓		
Roohi and Darbandi [130]				✓		
La Torre et al. [87]		✓				
Chung et al. [105]	✓	✓	✓			✓
Hedahl and Wilmoth [144]			✓			
Koura and Matsumoto [145]	✓					
Liu et al. [88]		✓				
Moss et al. [89]		✓				
Khanlarov and Lukianov [129]				✓		
Swaminathan-Gopalan and Stephani [122]	✓					
Weaver and Alexeenko [106]	✓					✓
Stefanov et al. [124]		✓				
Larsen and Borgnakke [103]	✓					
Larsen and Borgnakke [104]	✓	✓				
Xiao et al. [86]	✓	✓				✓
Klothakis and Nikolos [95]				✓		✓
Chen and Boyd [142]	✓	✓		✓		
Plotnikov and Shkarupa [143]		✓				
Pfeiffer et al. [121]		✓		✓		✓
Falchi et al. [146]		✓				
Chapter 5	✓	✓	✓	✓	✓	✓

Tab. 3.2. Overview of related work on DSMC/CFD simulations and classification of the present study. Here, Kn refers to studies related to continuum breakdown using global and/or local Knudsen numbers. ([a] Collision Model, [b] Gas-Surface Interaction, [c] Energy Consumption).

4 Modeling particle transport through multiscale flow regimes[1]

Understanding particle migration in fluid flows is fundamental in quantitatively describing aerosol systems. In particular, for single-particle diffractive imaging (SPI) experiments, precise control and prediction of particle behavior are essential for ensuring consistent performance and efficiency. Particulate flows in these systems can be modeled using either an Eulerian–Eulerian [147] or an Eulerian–Lagrangian approach [148, 149, 150]. In the Eulerian–Eulerian framework, both the carrier fluid and the particle phases are treated as continuous fields, with separate conservation equations for mass, momentum, and energy governing each phase. This multiphase continuum approach is most suitable when the particle volume fraction is high (e.g., fluidized beds, dust lifting devices etc.) [151, 152, 153, 154].

On the other hand, the Eulerian–Lagrangian approach is the most popular method for modeling particle transport in dilute flows. In this approach, the carrier fluid is described on a fixed grid using the Eulerian framework, while the particles or a number of representative particles are tracked individually in a Lagrangian framework. This method offers the distinct advantage of capturing detailed particle trajectory information – from the injection point to the final destination – enabling the study of dispersion, deposition, and focusing effects at the individual particle level. Additionally, this approach offers the flexibility to incorporate various complex forces acting on the particles, such as drag, gravity, thermophoretic and photophoretic forces, as well as stochastic forces arising from Brownian motion.

The coupling between the Lagrangian particles and the fluid solver can be implemented in several ways [148]. In a one-way coupling, the fluid flow influences the particles, but the particles do not affect the fluid flow. This is appropriate for systems with very low particle concentrations. In contrast, a two-way coupling scheme allows for mutual interaction, so that the momentum exchanged between the fluid and particles can alter the flow field. In even denser systems, a four-way coupling scheme has to be employed, which not only accounts for two-way fluid-particle interactions but also includes particle–particle collisions. For the aerosol systems used in SPI, the particle concentrations and sizes are typically low. This permits simplification by assuming that the flow field remains unaffected by

[1] The methodologies presented in this chapter are based on the publication: S. K. Peravali, A. K. Samanta, J. Küpper, M. Amin, P. Neumann and M. Breuer, "An improved simulation methodology for nanoparticle injection through aerodynamic lens systems", *Physics of Fluids* **37** (3), 033380, (2025) [74]. I am the principal contributor to this publication. I contributed in drafting the original manuscript and overseeing its review and editing processes. I was also deeply involved in the visualization and validation of data, the development and application of the methodology, and conducting the investigations. Additionally, I contributed in the formal analysis and conceptualization of the paper.

the presence of particles [148] and that particle–particle interactions are negligible [149], thereby justifying the use of a one-way coupled approach.

Using this approach, numerical simulations have been successfully employed to characterize particle beam collimation in aerosol injectors, such as aerodynamic lens stacks (ALS) [39, 40]. Another numerical study described the focusing of particles to a beam with a diameter smaller than 30 nm using an ALS [155]. This work established the guidelines for designing aerodynamic lens systems for nanoparticles [156] and also a design tool that predicts ALS dimensions to focus particles of certain sizes at different flow conditions [157]. This one-way coupled Eulerian–Lagrangian methodology was subsequently adopted for simulating nanoparticle-injection experiments at XFEL facilities [36]. Furthermore, gas-particle interactions in a cryogenically cooled buffer-gas system have also been studied using this approach [35]. In all these studies the flow through the aerosol injectors was assumed to be a *continuum* as numerical solvers based on continuum mechanics, i.e., the Navier-Stokes equations, were used to predict the gas flows under steady-state conditions. Furthermore, the flow was always constrained to be laminar because flow instabilities and turbulence can disperse particles and destroy focusing [157].

The particle trajectories were computed based on forces determined from these simulated flow fields. The forces acting on a particle can be broadly categorized into deterministic and stochastic components. The deterministic drag force ($\mathbf{F}_{drag}$) model used for calculating the particle movement in the fluid is often described by Stokes' law. Under continuum conditions, this model accurately predicts drag; however, when particle diameters become comparable to or smaller than the fluid's mean free path (rarefied gas flow with particle Knudsen number $Kn_p > 1$), non-continuum effects lead to decreased drag forces. To account for these effects, the empirical Cunningham slip-correction factor [45] was applied to the Stokes drag.

The Stokes-Cunningham drag model described and used in previous numerical works [35, 36, 39, 40, 155, 156] is confined to continuum gas flow fields at low Mach numbers and also strictly depends on empirical relations. For rarefied flow regimes ($Kn_p > 1$), the drag force on spherical particles at low Mach numbers was described by the Epstein model [46]. Unlike the Cunningham model, which assumes the gas molecules to be specularly reflected on the surface of the particle, the Epstein drag model assumes a combination of both specular and diffusive gas-surface collisions. A closed-form expression for the drag force on small spheres in the free-molecular regime for all Mach numbers was described [47]. Furthermore, several studies reported on the generalization of the drag force model to encompass a broad spectrum of Reynolds and Mach numbers. These works relied on either *ad-hoc* interpolations between different regimes [158, 159], empirical correlations from the available literature [150] or neural-network based empirical formulations [160]. In recent years, a derivation of a generalized physics-based expression for the drag coefficient of spherical particles was attempted [48]. For highly rarefied regimes where the gas can tend toward non-equilibrium, a DSMC-based approach for computing the drag force on a particle was introduced [161, 162]. This is advantageous when the molecular distribution of the gas is not known beforehand and can only be determined through DSMC computations. The main disadvantages of this model are that it can be inaccurate in the low-Knudsen number regime and that it is computationally inefficient.

In addition to drag, the Brownian motion plays a significant role, particularly at the nanoscale level. The Brownian motion arises from random collisions between gas molecules and particles, imparting a stochastic fluctuating force $\mathbf{F}_b$ that causes the particle trajectories to deviate from purely deterministic paths. This random motion is especially critical for nanoparticles, whose low inertia makes them highly sensitive to thermal fluctuations [163]. The interplay between the drag force and the Brownian motion is crucial for accurately modeling particle transport in aerosol systems.

The numerical studies described above have led to the development of an in-house particle trajectory simulation tool, denoted CMInject [42]. In previous studies using CMInject, the fluid flow field was computed exclusively with COMSOL [34, 37], a weakly compressible flow solver confined to low-Mach number flows. Presently, CMInject has been extended to work seamlessly with the compressible solvers in OpenFOAM described in Chapter 2, as well as with DSMC and the hybrid DSMC/CFD framework described in Chapter 3. Moreover, different drag models have been incorporated into CMInject to suit the corresponding flow regimes encountered – from continuum over transitional flows to rarefied flows. The following sections detail the numerical implementation of this extended framework, highlighting its enhanced applicability for simulating particle transport in multiscale aerosol systems.

4.1 Particle tracking with CMInject

The CMInject framework, implemented in Python [42], computes particle trajectories using the Langevin approach, where the motion of a particle is governed by the coupled equations:

$$\begin{aligned} \frac{d\mathbf{x}_p}{dt} &= \mathbf{u}_p, \\ \frac{d}{dt}\left(m_p\,\mathbf{u}_p\right) &= \mathbf{F}_{drag} + \mathbf{F}_b\ , \end{aligned} \tag{4.1}$$

with $\mathbf{x}_p$ representing the particle position, m_p the particle mass, $\mathbf{u}_p$ the particle velocity vector, $\mathbf{F}_{drag}$ the deterministic drag force, $\mathbf{F}_b$ the stochastic Brownian force, and t the time. A two-step approach is followed in the framework. In the first step of the one-way coupled approach, the flow field is computed using either CFD, DSMC, or a hybrid DSMC/CFD framework as described in Chapter 2 and Chapter 3. This flow field provides the necessary macroscopic properties – such as velocity, pressure, and temperature – that are used to compute the forces acting on the particles. The flow field, mapped onto a regular Cartesian grid as described in Chapter 3, is then linearly interpolated using `scipy.interpolate.RegularGridInterpolator` [164] to determine the fluid forces at the particle locations for subsequent trajectory calculations.

In the second step, particle trajectories are computed by numerically integrating the Langevin equation using the forces obtained from the interpolated flow field. The in-

tegration is performed by splitting the operations into two sequential steps: First, the deterministic contributions are integrated, i.e.,

$$\frac{d\mathbf{x}_p}{dt} = \mathbf{u}_p, \qquad \frac{d\mathbf{u}_p}{dt} = \frac{\mathbf{F}_{drag}}{m_p}\,. \tag{4.2}$$

To solve the resulting system of ordinary differential equations (ODEs) for the deterministic part of the particle trajectories, the LSODA routine is employed provided by the `scipy.ode` module [164, 165]. LSODA stands for Livermore Solver for Ordinary Differential equations with Automatic method switching. It is designed to automatically choose between non-stiff and stiff integration methods during the solution process. For non-stiff problems, LSODA uses an Adams method, which is a multistep predictor-corrector approach that can achieve high orders of accuracy (up to 12th order under optimal conditions). For stiff problems, LSODA switches to a backward-differentiation formula (BDF) method, which is implicit and typically achieves orders up to 5. This automatic method switching is particularly valuable in our generic multiphysics framework, where the ODE system, composed of multiple force contributions, may exhibit varying degrees of stiffness in different spatial regions. The deterministic step described by equation 4.2 updates the particle state, yielding an intermediate state (position $\mathbf{x}_p^*$ and velocity $\mathbf{u}_p^*$). In the subsequent (stochastic) step, the particle's state is perturbed to account for Brownian acceleration. Specifically, the updates are given by:

$$\mathbf{x}_p(t+\Delta t) = \mathbf{x}_p^* + \frac{1}{2\,m_p}\,\mathbf{F}_b\,\Delta t^2, \qquad \mathbf{u}_p(t+\Delta t) = \mathbf{u}_p^* + \frac{\mathbf{F}_b}{m_p}\,\Delta t. \tag{4.3}$$

Therefore, within each time increment Δt, the particle's state is first advanced by integrating the deterministic drag force, and then modified by the stochastic Brownian force. This operator splitting approach, detailed in [42], allows to separately address the deterministic and stochastic aspects of particle motion.

In addition to the Python implementation, a version of CMInject was also developed in Julia (see Appendix C), in which the Langevin equations are solved directly as stochastic differential equations (SDEs) using an Euler-Heun scheme instead of the operator-splitting ODE approach employed in Python. Both implementations were tested based on a non-stiff problem and produced similar results. However, the Python framework proved to be more efficient at higher particle numbers and in higher-dimensional simulations. For these reasons, the Python version has been adopted for the primary simulations. Detailed information on the Julia implementation and a comparison between both frameworks are provided in Appendix C.

In the following section, the relevant models for the drag force and the Brownian motion implemented in CMInject are described.

4.2 Forces on nanoparticles

4.2.1 Stokes-Cunningham drag model

At low Reynolds numbers, the classical Stokes drag model is widely used to quantify the drag force acting on a spherical particle. According to Stokes' law, the drag force is directly proportional to the dynamic viscosity μ of the fluid, the particle radius r_p, and the relative velocity $\Delta\mathbf{U}$ between the particle and the surrounding fluid:

$$\mathbf{F}_{\text{stokes}} = 6\,\pi\,\mu\,r_p\,\Delta\mathbf{U}. \tag{4.4}$$

This model is fundamental in many particle-laden flow applications, as it provides a simple yet effective way to estimate the resistance a particle experiences when moving through a viscous medium.

However, the classical Stokes drag model is based on the assumption that the flow around the particle behaves as a continuum with a no-slip boundary condition on its surface. When the particle size becomes comparable to the molecular mean free path of the gas (i.e., when the particle Knudsen number Kn_p exceeds unity), these assumptions break down. Under such conditions, the gas exhibits rarefaction effects and the particle surface experiences slip, leading to a decrease in the effective drag force. To correct for these non-continuum effects, the classical Stokes drag must be modified.

The conventional Stokes drag is corrected by the Cunningham slip coefficient C_c [45]:

$$\mathbf{F}_{\text{drag}} = \frac{6\,\pi\,\mu\,r_p\,\Delta\mathbf{U}}{C_c}, \tag{4.5}$$

with

$$C_c = 1 + Kn_p\,[A_1 + A_2\exp(-A_3/Kn_p)]. \tag{4.6}$$

For calculating C_c, the particle Knudsen number Kn_p is defined as the ratio of the mean free path of the gas to the radius of the particles. The coefficients $A_1 = 1.231$, $A_2 = 0.4695$ and $A_3 = 1.1783$ were empirically obtained for nitrogen gas [166]. A further correction to this model for high Mach number flows was also provided [48]. The corrected Cunningham slip coefficient (C_{c,W_r}) is given by:

$$C_{c,W_r} = 1 + Kn_p\,[A_1 + A_2\exp(-A_3/Kn_p)](1 + \alpha_{hoc}W_r^T), \tag{4.7}$$

where W_r^T is a nondimensional number given by:

$$\begin{aligned} W_r^T &= W_r\left(1 + \frac{T_p}{T_s}\right)^{\omega}, \\ \text{with } W_r &= \frac{Ma_\infty}{\text{Re}_\infty} = Kn_p Ma_\infty^{2\omega-1}\sqrt{\frac{2}{\pi\gamma}}Ma_\infty > 1 \end{aligned} \tag{4.8}$$

Here, T_p is the particle temperature, T_s is the post-shock temperature, ω is the exponent in the power-law dependence of the viscosity ($\mu \propto T^\omega$) on the temperature, Ma_∞ is the Mach number and Re_∞ is the Reynolds number of the freestream. The unknown param-

eter α_{hoc}[2] is determined using least-square fitting from different available experiments and relevant simulations [48]. The value $\alpha_{hoc} = 1.27$ [48] is used in the current thesis (Chapter 6).

4.2.2 Molecular drag models

To reduce the dependence on empirical coefficients, analytically derived models based on the kinetic theory of gases are considered for the extremely rarefied regimes in this thesis. When the size of the nanoparticle is very small compared to the mean free path of the gas, the interactions between gas molecules and the particle can be described by considering the momentum transfer during collisions. Under the assumption that gas molecules are specularly reflected from the particle surface, the drag force is given by the Epstein [46] model:

$$\mathbf{F}_{\text{spec}} = \frac{4\,\pi}{3}\, r_p^2\, N\, m\, \bar{c}\, \Delta\mathbf{U}\ . \tag{4.9}$$

Here, N is the number density of the gas molecules, m is the molecular mass of the gas and $\bar{c}$ is the average speed of molecules in the gas. Alternatively, if gas molecules are diffusively reflected, Epstein's model becomes:

$$\mathbf{F}_{\text{diff}} = \left(1 + \frac{\pi}{8}\right)\, \frac{4\,\pi}{3}\, r_p^2\, N\, m\, \bar{c}\, \Delta\mathbf{U}\ . \tag{4.10}$$

These models, derived from the kinetic theory of gases, provide analytical approximations for the drag force in the free-molecular regime and are most applicable for low-speed flows.

The Epstein model assumes that the relative velocity between the gas molecule and nanoparticle is sufficiently small. For high-speed flows, where large relative velocities occur, the drag force model on spherical particles is extended by Baines et al. [47]. The Baines model approximates a closed-form analytical expression for both specularly and diffusively reflected atoms/molecules for intermediate and high-speed flows (high Mach numbers), given by:

$$\mathbf{F}_{\text{spec}} = \frac{\pi^{3/2}\,\rho\, r_p^2\, \bar{c}^2}{4} \left\{ \left(S + \frac{1}{2S}\right) \exp(-S^2) + \sqrt{\pi} \left(S^2 + 1 - \frac{1}{4S^2}\right) \operatorname{erf} S \right\}\ , \tag{4.11}$$

$$\mathbf{F}_{\text{diff}} = \frac{\pi^{3/2}\,\rho\, r_p^2\, \bar{c}^2}{4} \left\{ \left(S + \frac{1}{2S}\right) \exp(-S^2) + \sqrt{\pi} \left(S^2 + 1 - \frac{1}{4S^2}\right) \operatorname{erf} S + \frac{\pi S}{3} \right\}\ . \tag{4.12}$$

Here, ρ is the density of the gas and $S = \sqrt{\frac{m}{2k_B T}} \cdot \Delta\mathbf{U}$ denotes the molecular speed ratio, where k_B is the Boltzmann constant and T the temperature of the gas. The total drag

[2] hoc refers to higher-order correction.

force on the particle is assumed to be a combination of a certain fraction (α) of diffuse reflections and the remaining fraction ($1-\alpha$) are specular reflections:

$$\mathbf{F}_{\text{drag}} = (1-\alpha)\,\mathbf{F}_{\text{spec}} + \alpha\,\mathbf{F}_{\text{diff}}. \tag{4.13}$$

It is typically assumed that $\alpha = 0.9$ [46, 167, 168, 169], a value that is also adopted in this thesis. For low Mach number flows ($Ma < 0.3$), the Epstein model is employed, whereas for high Mach number regimes the drag model is switched to that of Baines et al. [47] for the cases presented in Chapter 6 and Chapter 7.

4.2.3 Relaxation of Epstein drag model

For particles traversing across low-speed transition or molecular flow regimes (i.e., DSMC regions with $Kn_B > 0.05$), comparisons with experimental data have revealed a limitation of the above-mentioned drag force models. The models overpredict the drag force in this regime due to the overestimation of impinging gas molecules that transfer momentum to the nanoparticle. Therefore, a relaxation of the drag force is necessary to accurately track particles in the flow by estimating the actual fraction of colliding molecules when particles move through a sub-cell of the simulation domain. To address this issue, an approach has been developed by the author [74].

In this approach, a sub-cell of the flow field, in which a certain number of gas molecules exist, is considered. The gas velocity distribution functions in this sub-cell are assumed to follow the Maxwell-Boltzmann distribution. Like in DSMC, certain numbers of simulation molecules are generated where each particle represents real molecules in the system that roughly have the same position and velocity. From the macroscopic flow data, such as pressure, flow velocity and temperature, velocities are assigned to the simulation molecules in the sub-cell. The relative velocity of the randomly chosen simulation molecule with respect to the nanoparticle is estimated by:

$$\mathbf{u}_{r,i} = (\mathbf{u}_i + \mathbf{U}) - \mathbf{u}_p, \tag{4.14}$$

where $\mathbf{u}_i$ is the thermal velocity of the randomly chosen simulation molecule from the Maxwell-Boltzmann distribution, $\mathbf{U}$ is the bulk velocity of the gas flow obtained from DSMC and $\mathbf{u}_p$ is the velocity of the nanoparticle.

The collision between the nanoparticle and the impinging gas molecules that have a relative velocity less than the most probable speed of the gas molecules $c'_m = \sqrt{2k_BT/m}$ in the low-speed high-Knudsen number regime is assumed to be stochastic. Thus, a gas molecule collides with the nanoparticle, if

$$1 - \exp\left(-\frac{|\mathbf{u}_{r,i}|}{c'_m}\right) > R_f\ . \tag{4.15}$$

Here, R_f is a randomly generated number from $(0, 1]$ with a uniform distribution and Eq. (4.15) filters certain impinging molecules using Monte-Carlo acception-rejection sampling. The fraction of colliding molecules P_{coll} is determined per time step and the

total drag force $\mathbf{F}_{\text{drag}}$ from Eq. (4.13) (obtained from Eqs. (4.9) and (4.10)) is relaxed accordingly:

$$\mathbf{F}_{\text{drag, relaxed}} = P_{\text{coll}} \cdot \mathbf{F}_{\text{drag}} \, . \tag{4.16}$$

This improved model enhances the accuracy of particle tracking in highly rarefied flow regimes by accounting for the actual fraction of gas molecules that contribute to momentum transfer, thereby correcting the overprediction of the standard Epstein drag model. It is applied and validated in Chapter 6 for highly rarefied cases and utilized in highly rarefied cryogenic buffer-gas scenarios in Chapter 7.

4.2.3.1 Brownian motion

The drag force estimated above is the force obtained by averaging single collisions undergone by the particle per unit time, i.e., it is the mean force acting on the particle. However, the particle trajectory is also influenced by the Brownian motion due to the nanometer size range of the particle. The Brownian motion force is defined based on a Gaussian white noise random process having a spectral intensity S_0 as:

$$\mathbf{F}_b = m_p \, \mathbf{G} \, \sqrt{\frac{\pi \, S_0}{\Delta t}} \, . \tag{4.17}$$

Here, $\mathbf{G}$ is a vector of independent Gaussian random numbers with zero mean and unit variance and Δt is the time step. The spectral intensity can be defined using the Cunningham slip correction factor as [163]:

$$S_0 = \frac{27 \, \mu \, k_B T}{4 \, \pi^2 \, r_p^5 \, \rho_p^2 \, C_c} \, , \tag{4.18}$$

where μ is the dynamic viscosity and ρ_p the density of the particle. This model is applied in conjunction with the Stokes–Cunningham drag force. Alternatively, the spectral intensity based on the kinetic theory is calculated as [170]:

$$S_0 = \left(\frac{16}{3} + \frac{2\pi}{3} \sqrt{\frac{T_p}{T}} \right) \frac{\overline{c}}{2} \, p \, \frac{m}{m_p^2} \, r_p^2 \, . \tag{4.19}$$

Here, T_p is the temperature of the particle and p is the pressure of the gas. This model is used in conjunction with the molecular drag models, i.e., for cases where empirical coefficients for the Cunningham slip correction factor are unknown.

In the process of diffuse scattering, a particle with a temperature different from that of the gas undergoes thermalization. The change in particle temperature per unit time is given by [170]:

$$\Delta \dot{T} = \frac{4p\sqrt{\pi} r_p^2}{c_p m_p} \left[\beta \beta_p^{-2} - \beta^{-1} \right] \, , \tag{4.20}$$

Here, c_p is the specific heat of the particle, β is the reciprocal of the most probable thermal speed $\sqrt{m/(2k_BT)}$ and $\beta_p = \sqrt{m/(2k_BT_p)}$. Subsequently, the particle temperature is then updated in time as:

$$T_p(t + \Delta t) = T_p(t) - \Delta\dot{T}\Delta t \ . \tag{4.21}$$

In summary, using the current framework the nanoparticle focusing behavior is studied in detail for various aerosol cases in Chapter 6 and Chapter 7. The accuracy of the entire simulation tool is evaluated by comparing simulation results with experimental data, thereby comprehensively assessing all the force models described in this chapter.

5 Evaluation of CFD, DSMC and hybrid DSMC/CFD methods on low density flows[1]

This chapter presents a detailed study on the advantages and limitations of CFD and DSMC methods for simulating rarefied gas flows, with particular emphasis on both simulation accuracy and computational performance. The hybrid DSMC/CFD methodology described in Chapter 3 is systematically evaluated. For this purpose, DSMC and CFD simulations of the flow inside a convergent-divergent nozzle (internal expanding flow) and the flow around a conical body (external shock generating flow) were carried out. The results of these simulation techniques are evaluated by comparisons with experimental data.

The DSMC simulations typically entail high computational costs. Therefore, high-performance computing techniques are often applied to reduce the time-to-solution for both pure DSMC and hybrid simulations [126, 127, 128, 130, 131]. While numerous works study the accuracy of the DSMC and CFD methods and how different parametrization, e.g., the choice and parameters for the collision model or the number of simulation particles, impact this accuracy [85, 87, 88, 89, 93, 105, 141, 145], they do not take into account the cost and effort of the methods and how much resources in terms of energy they consume. On the other hand, in studies on the computational performance of the DSMC method [126, 127, 128, 130, 131, 132], the influence of the different parametrization on the simulation results was not investigated.

Numerous studies have been devoted to analyze and compare the performance of CFD and DSMC approaches for simulating rarefied and transitional gas flows, [85, 87, 88, 89, 93, 105, 126, 127, 128, 129, 130, 131, 132, 133, 141, 145]. These works collectively explore various aspects such as solver accuracy, applicability across different flow regimes, and computational feasibility. However, a detailed explanation of the impact of the great variety of parametrization possibilities of the solvers, in particular for DSMC, is often incomplete or tailored to very specific setups that are not easily generalizable. Furthermore, the precision of the results and the performance of the DSMC method are not considered

[1] This chapter is based on the publication: S. K. Peravali, V. Jafari, A. K. Samanta, J. Küpper, M. Amin, P. Neumann and M. Breuer, "Accuracy and performance evaluation of low density internal and external flow predictions using CFD and DSMC", *Computers & Fluids* **279**, 106346 (2024) [73]. I am the principal contributor to this publication. I contributed in drafting the original manuscript and overseeing its review and editing processes. I was also deeply involved in the visualization and validation of data, the development and application of the methodology, and conducting the investigations. Additionally, I contributed in the formal analysis and conceptualization of the paper.

simultaneously in order to judge whether the accuracy is worth the amount of time and energy that the simulation consumes.

Earlier in Section 3.6, the relevant literature and open challenges were summarized. Building on that foundation, this chapter evaluates the hybrid DSMC/CFD methodology through two representative flow scenarios, examining the trade-off between accuracy and computational cost. The test cases and their corresponding flow conditions are introduced in Section 5.1. The overall simulation setup, including solver configurations for CFD, DSMC, and hybrid DSMC/CFD, is detailed in Section 5.2. The CFD solvers for the compressible flow `sonicFoam` and `rhoCentralFoam`, previously discussed in Chapter 2, are assessed for the internal nozzle flow in Section 5.3.1. The DSMC and hybrid coupling approaches described in Chapter 3 are validated against experimental data in Section 5.3.2 and Section 5.3.3 for both flow cases. The subsequent Section 5.4 also includes a systematic investigation of key DSMC parameters and their influence on both accuracy and performance, with metrics such as runtime and energy consumption reported for each setup. Finally, Section 5.5 summarizes the findings and provides an outlook toward the case studies presented in Chapter 6 and 7.

The main goals of this chapter are:

- Presenting a comprehensive study of rarefied gas flows for internal and external configurations
- Using a combination of 2D/3D configurations of DSMC, CFD and hybrid DSMC/CFD simulation
- Highlighting the effect of different parameters having major impact on the simulation such as mesh size, number of particles, time step, collision model, boundary conditions, and computational speed
- Validating and evaluating the simulations against experiments
- Reporting the performances and computational efforts of the employed approaches in terms of scalability and energy consumption

5.1 Test cases

5.1.1 Internal expanding flow (gas dynamic nozzle)

Figure 5.1 indicates the 2D simulation domain of the low density nozzle. The test case is based on the experiment by Rothe [171] where the low density flow properties are measured inside the nozzle using the electron beam fluorescence technique. The inflow boundary is located on the extreme left (line ab), i.e., at the inlet of the pressure chamber. An outflow boundary condition is assumed along the extreme right of the geometry (line fghij). The segment (aj) in Figure 5.1 is the axis of symmetry. For 2D simulations, an axisymmetric boundary condition was imposed. 3D simulations were carried using the complete geometry.

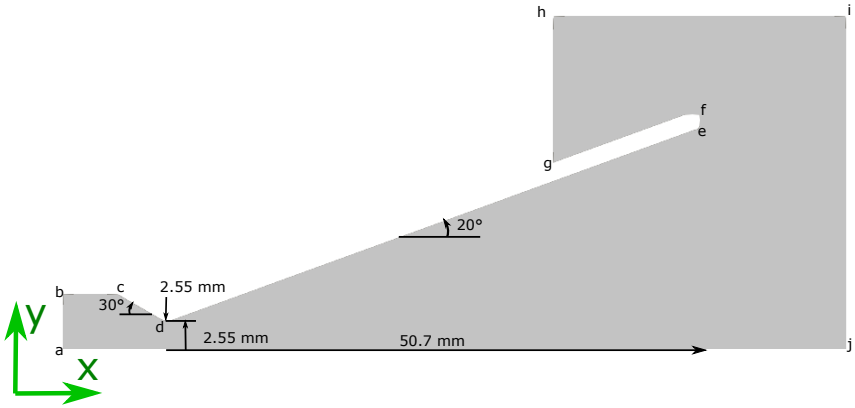

Fig. 5.1. Computational domain of the low density nozzle flow (cases i.I to i.III).

The test gas used in the simulation is nitrogen with a stagnation temperature of 300 K. Three different stagnation pressure configurations are tested according to the setup described in Table 5.1. That leads to the three internal flow cases i.I to i.III. The nozzle Reynolds number Re_N is calculated using $Re_N = \rho_o \hat{u} r_* / \mu_o$ where ρ_o is the stagnation density, $\hat{u}$ is the adiabatic speed, r_* is the radius of the throat and μ_o is the viscosity based on the stagnation condition. The Knudsen number is calculated based on the stagnation condition and the throat diameter.

Parameters	**i.I**	**i.II**	**i.III**
Test gas	N_2	N_2	N_2
Stagnation temperature, T_o [K]	300	300	300
Stagnation pressure, P_o [Pa]	474	209	141
Wall temperature, T_w [K]	300	300	300
Nozzle Reynolds number, Re_N	590	260	175
Throat Knudsen number, Kn_t	2.3×10^{-3}	6.17×10^{-3}	9.15×10^{-3}
Back pressure, P_a [Pa]	1.8	0.64	0.45

Tab. 5.1. Flow-condition parameters of the low-density-nozzle cases i.I to i.III.

5.1.2 External shock generating flow (flow over blunt and sharp conical bodies)

Figure 5.2 demonstrates the 2D computational domains of the external flow simulations considering two geometries. The first geometry is a cone-shaped half body with a blunted nose and the second one possesses a sharp nose. Both geometries are assumed to be infinitely long in positive x-direction. The symmetry line of the half body is aligned with the free-stream. For the first half body, only the first 0.05 m of the blunted nose with a radius of 6.35×10^{-3} m (0.25 in) is considered For the second half body, the first 0.09 m

of the sharp nose is taken into account. The computational domains around these bodies are depicted in Figure 5.2.

The fluid considered in both cases was pure nitrogen and the ambient conditions at different altitudes are listed in Table 5.2. Other parameters needed for CFD and DSMC simulations such as the pressure and number density were calculated correspondingly. The flow direction was in x-direction such that the left and right surfaces of the domain represent the inlet and outlet, respectively (see Fig. 5.2). For the 2D external flow, only half of the computational domain in y-direction was considered, i.e., a cut through the computational domain (x-y plane) as visible in Figure 5.2. The axisymmetric boundary condition was imposed on the line a-d.

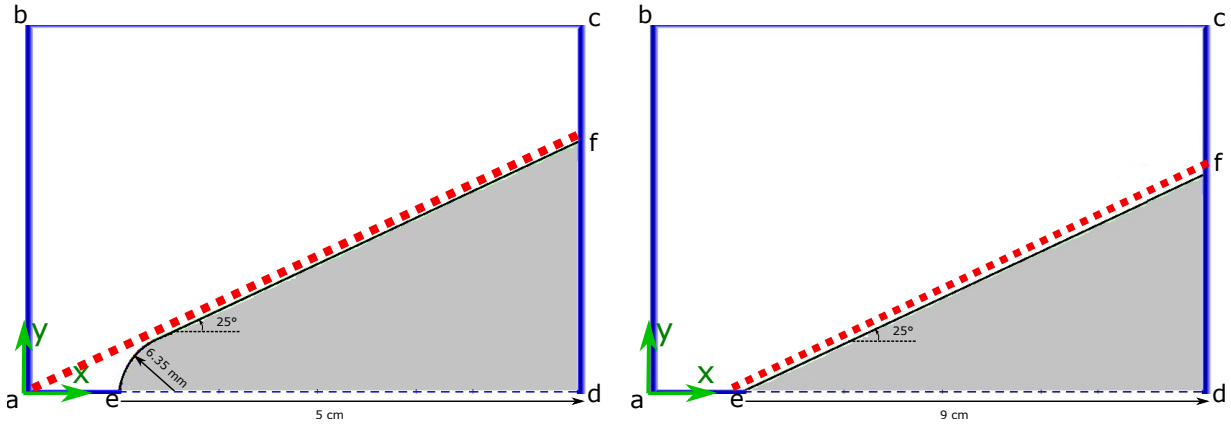

Fig. 5.2. Computational domains for the external flow test cases. (a) Half body cone with blunted nose, 2D setup. (b) cone with sharp nose, 2D setup.

Parameters	**e.I**	**e.II**
Geometry	Blunt cone	Sharp Cone
Gas mixture	N2	N2
Ambient velocity, V_∞ $[\frac{\mathrm{m}}{\mathrm{s}}]$	2764.5	2072.6
Ambient temperature, T_∞ [K]	144.4	42.61
Ambient pressure, p_∞ [Pa]	21.91	2.23
Ambient density, ρ_∞ $[\frac{\mathrm{kg}}{\mathrm{m}^3}]$	5.113×10^{-4}	1.757×10^{-4}
Mach number, M_∞	11.3	15.6
Wall temperature, T_w [K]	297.2	297.2
Knudsen number, Kn_∞	4.168×10^{-3}	1.236×10^{-2}
Reynolds number, Re_∞	4020	1862

Tab. 5.2. Flow conditions for external test cases.

5.2 Simulation settings

5.2.1 OpenFOAM

The CFD simulations for both internal and external cases are conducted on three-dimensional domains using body-fitted grids. Structured grids are generated using the `blockMesh` and `snappyHexMesh` utilities in OpenFOAM, as illustrated in Figure 5.3 and Figure 5.4. For the internal flow case (nozzle), the final grid comprises 513,035 cells. For the external flow cases, grids with 5,143,944 cells (blunt cone, case e.I) and 8,240,616 cells (sharp cone, case e.II) are used. These grid resolutions are chosen based on prior grid-independence studies, which are not detailed here, as the CFD simulations themselves are not the primary focus of this study.

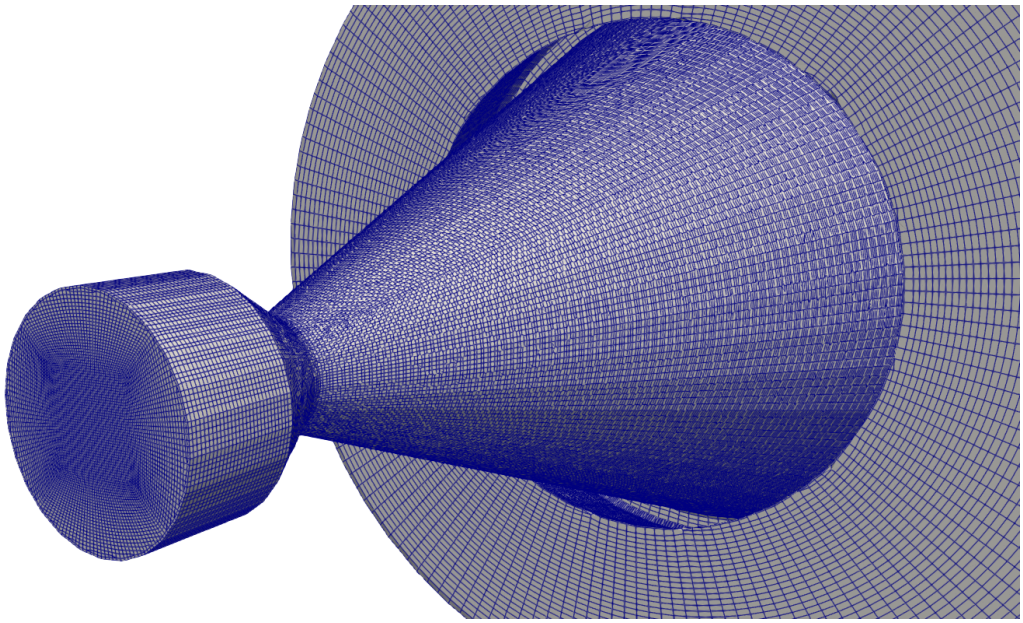

Fig. 5.3. Structured O-grid of the nozzle geometry.

The numerical discretization schemes and solution methods for each solver follow the descriptions provided in Chapter 2. These are implemented through the `fvSchemes` and `fvSolution` dictionaries in OpenFOAM (see Appendix A). The dynamic viscosity μ is calculated using Sutherland's law with a Sutherland coefficient $A_s = 1.41716 \times 10^6$ and a Sutherland temperature $T_s = 111$ K for nitrogen gas [172].

The boundary conditions assigned to the test cases are listed in Tables 5.3 and 5.4 for the internal and external flow cases, respectively.

5.2.2 SPARTA

The DSMC simulations for both internal and external flow configurations are performed using SPARTA on two-dimensional and three-dimensional uniform Cartesian grids. The baseline grid size is chosen as $\Delta x = \frac{1}{3}\lambda_{\min}$, which follows the typical resolution criterion

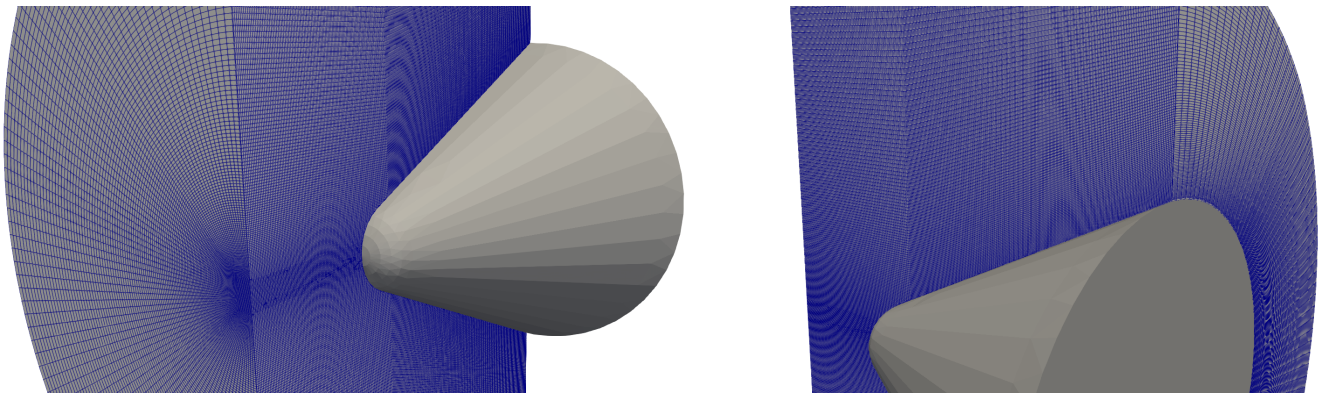

(a) (b)

Fig. 5.4. Structured grid (clipped) of a typical conical body viewed from different directions.

Boundary	**U**	**P**	**T**
Inlet	zero gradient	fixed value	fixed value
Outlet	zero gradient	wave transmissive	zero gradient
Wall	no-slip	zero gradient	fixed value

Tab. 5.3. Boundary conditions for the low-density-nozzle flow (internal).

Boundary	**U**	**P**	**T**
Inlet	fixed value	zero gradient	fixed value
Outlet	inlet outlet	wave transmissive	zero gradient
Boundaries	supersonic free-stream	zero gradient	fixed value
Solid walls	no-slip	zero gradient	fixed value

Tab. 5.4. Boundary conditions for the flow around a conical body (external flow).

for DSMC simulations. Here, λ_{min} denotes the minimum mean free path within the DSMC domain and is listed for each case in Table 5.5. Additionally, the effect of varying grid sizes is examined and discussed in Section 5.4.2.

The no-time-counter (NTC) method is employed for collision sampling (see Section 3.3), using both the variable-hard-sphere (VHS) and variable-soft-sphere (VSS) molecular models. Internal energy exchange is modeled using the Larsen and Borgnakke (L-B) approach, implemented with both constant and variable rotational relaxation [43]. In this study, vibrational modes and chemical reactions are assumed to be frozen. The specific molecular collision parameters used in the simulations are listed in Table 3.1.

For the variable relaxation model, the rotational relaxation parameter ϕ_{rot} in SPARTA is computed using Equation (3.23). The required parameters in this expression are obtained from experimental data reported by Parker [107] and Lordi and Mates [108].

Gas-surface interactions are modeled using the approaches described in Section 3.2, specifically the Maxwell and Cercignani-Lampis-Lord (CLL) models. The Maxwell model is evaluated under fully diffusive, fully specular, and mixed reflection conditions, as detailed in Section 5.4.4. The CLL model is applied to represent fully diffusive scattering with incomplete energy accommodation, enabling an investigation into the influence of the thermal accommodation coefficient on wall interactions.

5.2.3 Hybrid DSMC/CFD

Hybrid simulations were conducted for the internal cases (i.I to i.III) using the methodology outlined in Section 3.5. The corresponding simulation settings from Section 5.2.1 and Section 5.2.2 were applied to the CFD and DSMC regions, respectively. The breakdown of the continuum assumption was evaluated using the breakdown Knudsen number Kn_B, calculated according to Equation (3.34). When $Kn_B > 0.05$, a breakdown of the continuum is assumed, and the DSMC computational domain is generated by partitioning the CFD domain from the breakdown interface to the outflow boundary.

5.3 Results

5.3.1 Evaluation of CFD solver: `sonicFoam` vs. `rhoCentralFoam`

To assess the relative advantages and limitations of the pressure-based and density-based approaches, the performance of the `sonicFoam` and `rhoCentralFoam` solvers is evaluated using the internal expanding flow case (case i.I). This case involves a supersonic flow expanding from a nozzle into vacuum, a scenario that closely resembles the flow physics encountered in aerodynamic lens systems. This problem is characterized by high-speed compressible flows, with substantial pressure and temperature gradients, making it a suitable and rigorous test for comparing the solvers.

To evaluate the performance differences between the two solvers, the Mach number contours obtained from the simulations are shown in Figure 5.5, where the upper half displays results from the pressure-based solver `sonicFoam`, and the lower half corresponds to the density-based solver `rhoCentralFoam`. It is observed that `rhoCentralFoam` predicts consistently higher Mach numbers, particularly near the centerline.

Figure 5.6 (a) presents the centerline Mach number profiles as a function of the non-dimensional axial distance x/R_t, where x is the distance from the nozzle throat and R_t is the throat radius. The results show that `rhoCentralFoam` predicts a monotonic acceleration of the flow from the throat to the exit, while `sonicFoam` shows a peak Mach number of approximately 3 at $x/R_t \approx 12.5$ followed by a slight deceleration.

Figure 5.6(b) shows the corresponding centerline temperature profiles normalized by the stagnation temperature T_0. The `rhoCentralFoam` solution shows a monotonic decrease in temperature, which aligns well with the experimental data of Rothe [171]. In contrast, `sonicFoam` predicts a minimum temperature near $x/R_t \approx 12.5$, followed by a rise toward the exit, deviating significantly from the experimental trend.

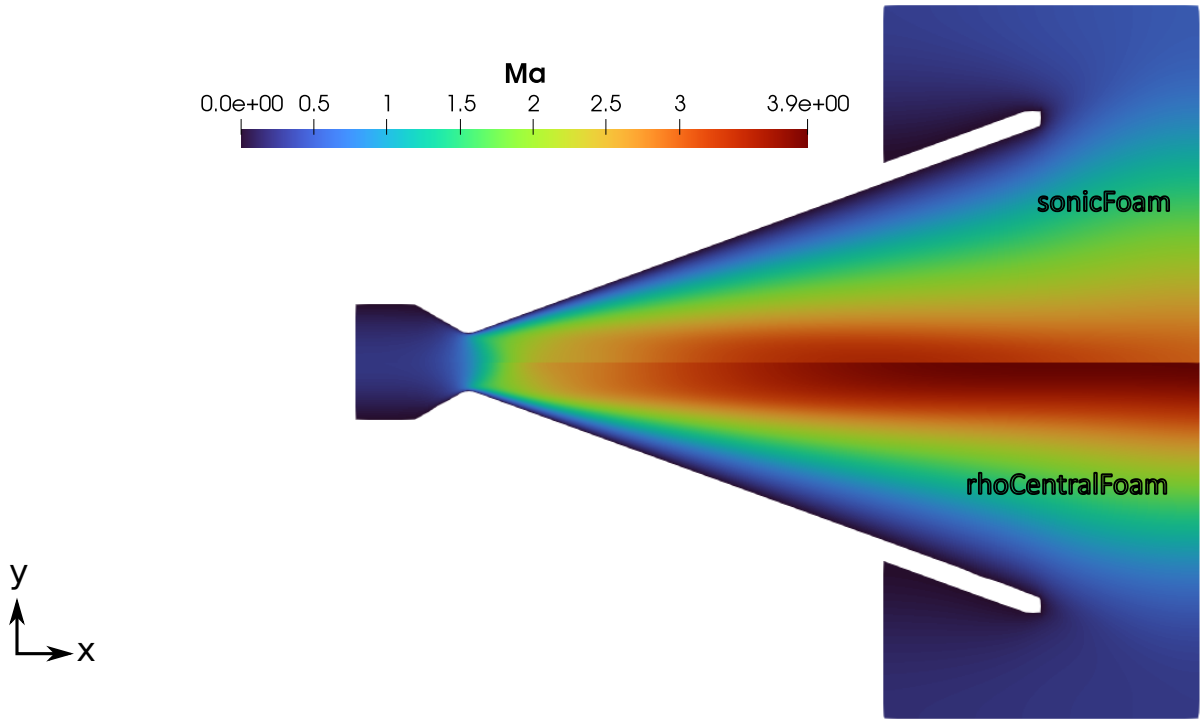

Fig. 5.5. Comparison of Mach number contours obtained by the `sonicFoam` solver (upper) and `rhoCentralFoam` solver (lower).

Overall, these results demonstrate that `rhoCentralFoam` provides more accurate predictions of the nozzle expansion, particularly in high-speed compressible flows. This improved performance is attributed to its density-based formulation, which inherently handles shock waves, steep gradients, and compressibility effects more robustly through central-upwind schemes. In contrast, `sonicFoam` relies on the pressure-velocity coupling that can struggle to capture sharp expansions or rarefaction waves accurately in supersonic flows.

For the simulations presented in the following sections, the term “Openfoam" will be used interchangeably with results obtained by using the density-based solver `rhoCentralFoam`, unless stated otherwise.

5.3.2 Internal flow: CFD, DSMC and hybrid DSMC/CFD

Simulations were performed for the test cases presented in Table 5.1 using the continuum approach (`rhoCentralFoam`), the DSMC method and the hybrid DSMC/CFD. The full DSMC simulations are inefficient in the low Knudsen regime ($Kn < 0.05$) and demand very high computational effort. Therefore, the hybrid DSMC/CFD method was used in order to accelerate the simulations. The results obtained by the continuum approach were used to estimate the breakdown Knudsen number Kn_B (Eq. (3.34)). By determining Kn_B throughout the simulation domain, it was observed that the continuum breakdown occurred in the simulation domain right after the throat. Hence, the interface between the continuum and DSMC domain was positioned at the throat using the approach described

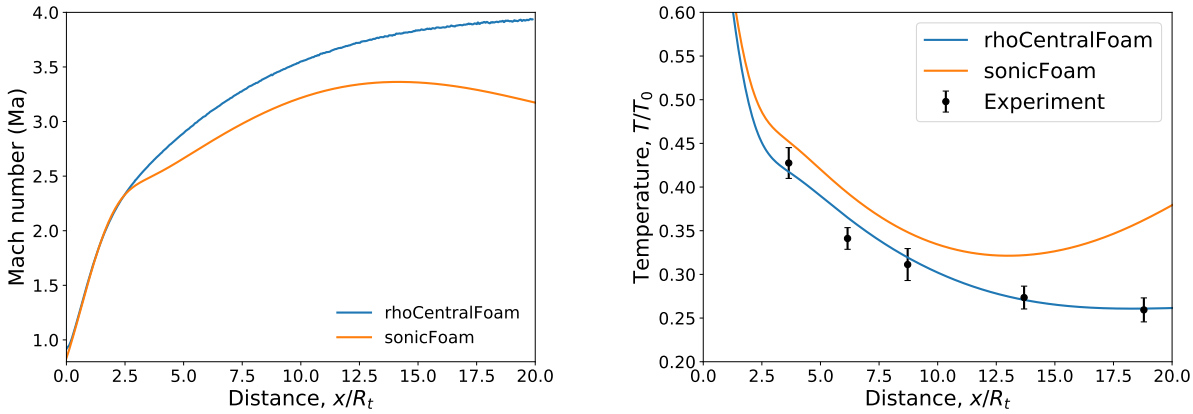

(a) (b)

Fig. 5.6. (a) Centerline Mach number profiles from throat to exit of the nozzle. (b) Comparison of temperature variation along the centerline of the nozzle.

in Section 3.5. The continuum simulations were performed for a 3-D simulation domain and the hybrid DSMC/CFD using both the 2D axisymmetric and 3D configuration. The simulation results were validated against experiments conducted by Rothe [171] and the deviations are presented in the following figures. The sensitivity studies concerning different simulation parameters are described in Section 5.4. Due to the limited availability of experimental data, the cases i.I and i.III were studied in more detail than case i.II, where only the centerline temperature data is available.

Figure 5.7 to 5.11 show various flow parameters obtained using the continuum approach and the hybrid DSMC approach. For the purpose of validation, the corresponding experimental data [171] are included. Figure 5.7 (a) and (b) show the centerline density profiles in the nozzle for cases i.I and i.III, respectively. Here, the densities ρ were normalized by the stagnation density ρ_o and this ratio was plotted against the non-dimensional axial distance.

The radial variation of densities normalized by the maximum cross-sectional density ρ_c found at the axis is studied at the cross-sectional position $x/R_t = 13.7$ from the throat for case i.I in Figure 5.8 (a) and for case i.III in Figure 5.8 (b). The radial density profiles are also studied for other cross-sectional positions depicted in Figure 5.18 in Section 5.4. The density profiles obtained by the hybrid DSMC method show good agreement with the experimental data compared to the continuum method. It should be noted that the error limits in the measured experimental densities reported by Rothe [171] are ± 10 % along the centerline and ± 5 % for the relative densities along the cross-sections.

Figure 5.9 shows the centerline temperature profiles of cases i.I and i.III, respectively. The equilibrium temperature was calculated by the continuum method and the translational and rotational temperatures were predicted by the hybrid DSMC method. Similar to the densities, all temperatures were normalized by the stagnation temperature T_o and plotted against x/R_t. For case i.I, where $Re_N > 500$, the computed temperatures from all three models agree well with the experimental data, while for $Re_N < 300$ there are

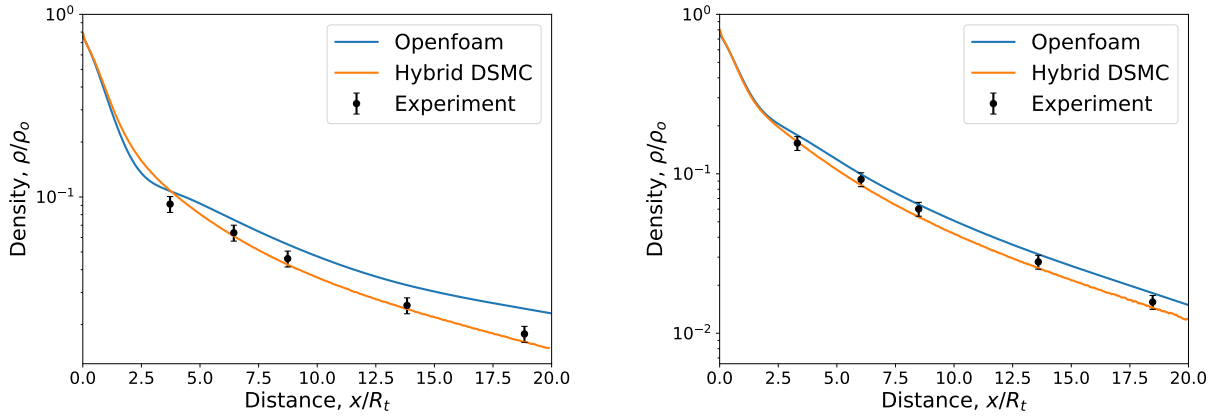

Fig. 5.7. Comparison of density variation along the nozzle centerline: (a) Case i.I, (b) Case i.III.

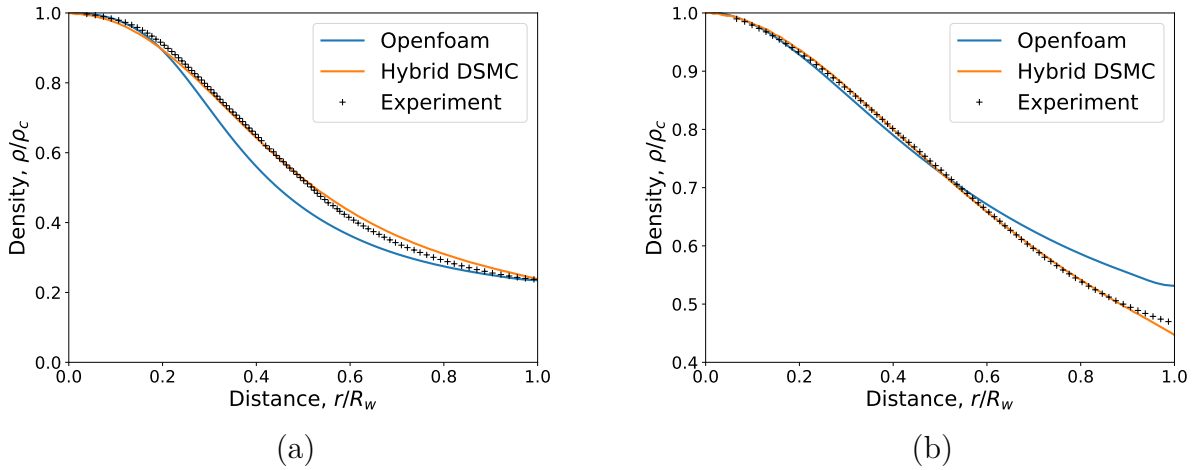

Fig. 5.8. Comparison of density variation along the radial direction at the cross-section $x/R_t = 13.7$ from the throat for the cases (a) i.I and (b) i.III.

significant differences: Unlike the case i.I ($Re_N > 500$) where the temperatures decrease monotonically from the throat to the exit of the nozzle (Figure 5.9 (a)), in the cases i.II and i.III ($Re_N < 300$) the temperatures reduce to a minimum at $x/R_t \approx 6$ and increase toward the exit of the nozzle (see Figure 5.9 (b) and Figure 5.13. This is a result of stronger rarefaction effects where the flow gets thermalized due to viscous dissipation, i.e., due to more molecule-surface collisions than molecule-molecule collisions. This effect also has an influence on the Mach number profiles shown in Figure 5.10. However, it can be observed that the rotational temperatures predicted by DSMC match best with the measurements as the experimental data [171] are rotational temperatures.

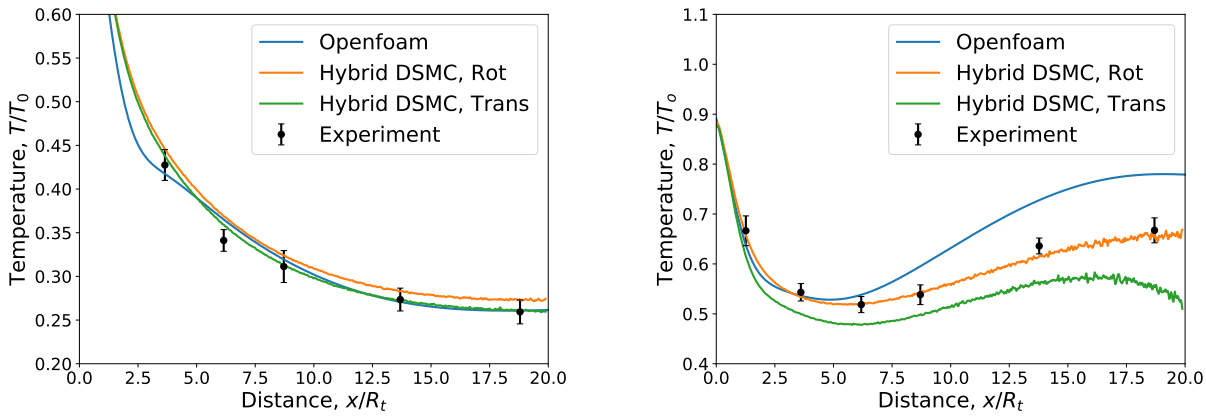

(a) (b)

Fig. 5.9. Comparison of temperature variation along the nozzle centerline for the cases: (a) i.I and (b) i.III.

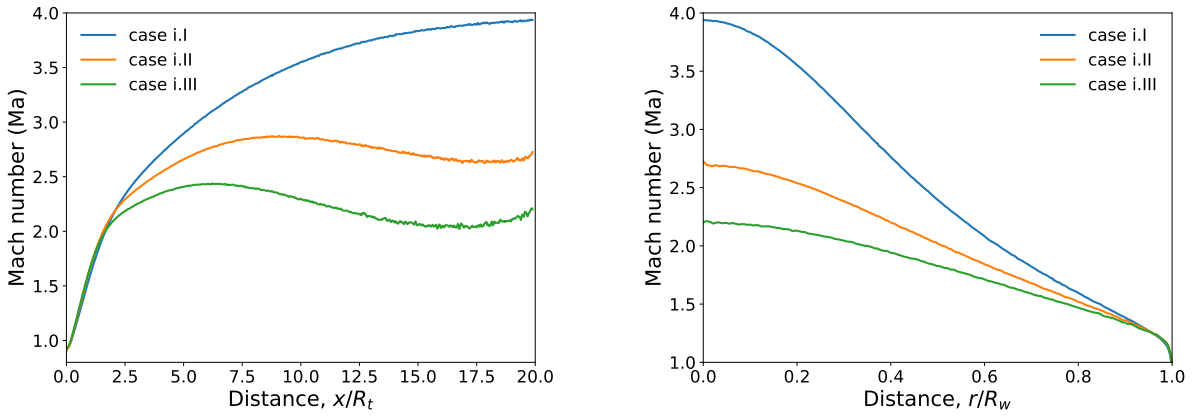

(a) (b)

Fig. 5.10. (a) Centerline Mach number profiles from throat to exit. (b) Radial Mach number profiles at the exit plane of the nozzle.

Figure 5.11 shows the normalized temperature variation against the radial distance normalized by the cross-sectional radius at $x/R_t = 13.7$ from the throat. The rotational temperatures are again in good agreement with the experimental data. The rotational temperature is always greater than the translational temperature due to flow expansion [171]. The equilibrium temperature obtained by the continuum method can be compared with the translational temperatures from the hybrid DSMC method. The differences between these two temperatures, particularly for $Re_N < 300$, and the differences in densities observed above are due to the inaccuracy of the continuum method in the rarefied flow regimes.

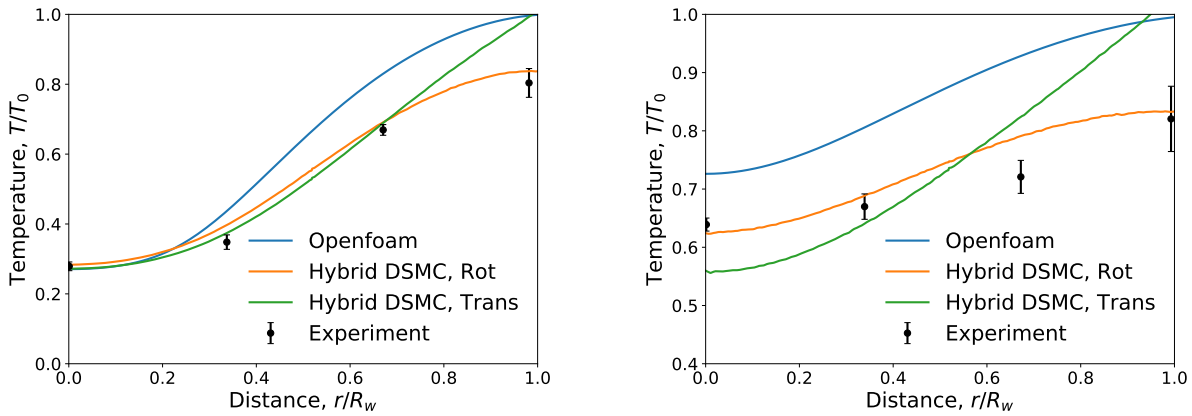

Fig. 5.11. Comparison of temperature profiles in the radial direction at a non-dimensional distance $x/R_t = 13.7$ from the throat for the cases (a) i.I and (b) i.III.

5.3.3 External flow: CFD and DSMC

External flow simulations were carried out for the test cases listed in Table 5.2 using pure CFD and DSMC methods. The flow is assumed to be laminar, which is in line with the fact that the Reynolds number is relatively small. As described earlier, the results for the continuum approach were used to estimate the breakdown Knudsen number Kn_B ((Eq. (3.34))). By determining Kn_B throughout the simulation domain, it is found that near the surface of the external bodies, Kn_B is relatively small ($Kn_B < 0.004$). This is due to a shock wave formed around the bodies which eventually increases the pressure and the density inside the shock layer. The pressure coefficient C_p is used as a quantity for validating the external flow cases. In Figure 5.2 the dotted red lines indicate the measurement line, along which the results are evaluated.

Figure 5.12 shows the variation of C_p on the surface plotted against the axial distance x for cases e.I and e.II, respectively. Due to the near-continuum flow in the vicinity of the surface, both continuum and DSMC methods show similar trends in the results and reasonably match the experimental data [120, 173, 174]. However, the DSMC results show a smoother variation in C_p. Furthermore, there is a significant difference in the results of the methods near the stagnation region ($x \approx 0$ cm to 0.5 cm). This is because the DSMC method predicts a much thicker shock layer around the body compared to the continuum method particularly near the stagnation region. This phenomenon is subject to further investigations. Sensitivity studies of different simulation parameters are described in Section 5.4.

5.4 Sensitivity of DSMC parameters

The results presented in Section 5.3.2 and 5.3.3 show the level of accuracy of the DSMC method in resolving rarefied gas flows. However, as mentioned in Chapter 3, several

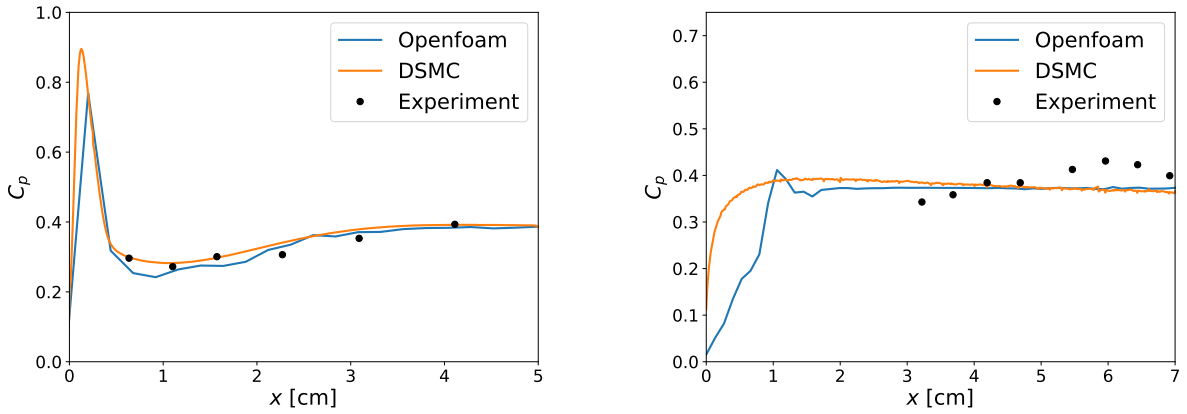

Fig. 5.12. Comparison of the pressure coefficient C_p over the surface of the body for the cases (a) e.I and (b) e.II.

simulation parameters are responsible for attaining these accurate results. In this section, the sensitivity of the results with respect to different DSMC simulation parameters is presented. Although the simulations for the internal flow cases were carried out using the hybrid method, only the DSMC domain, i.e., the region where $Kn_B > 0.05$, is considered for this parameter study.

5.4.1 Effect of simulation particle number

In order to accurately describe the rarefied gas flow, it is important to have a sufficient number of simulation particles in the simulation domain and per grid cell. These represent the distribution of the actual gas molecules and are necessary to preserve the statistical accuracy and resolution of molecular collisions in the simulation. In SPARTA, this property is controlled by the keyword `fnum`. The parameter `fnum` sets the ratio of real molecules to the simulation particles. Therefore, the smaller the value of `fnum`, the greater the number of simulation particles and the simulation accuracy. Once the number of simulation particles crosses a certain threshold, the accuracy of the simulation reaches convergence in results. Using much smaller values of `fnum` compared to this threshold value increases the computational cost as in DSMC the computational cost scales linearly with the number of simulation particles [94]. Therefore, it is very important to choose a trade-off value of `fnum` to optimize the computational costs while ensuring the accuracy of the simulation.

The simulation domain was discretized with regular grids and the grid cell size, e.g., Δx, of the simulation is chosen according to the criterion mentioned in Section 5.2.2, i.e., $\Delta x \leq \frac{1}{3}\lambda_{min}$.

The present convergence study varying `fnum` has been performed for a uniform grid of size Δx. The simulation particles were created using the `fnum` parameter and were distributed such that each cell has roughly the same number of particles. Figure 5.13 (a) shows the effect of the parameter `fnum` on the predicted rotational temperature for the

2D internal flow case i.II. A value of `fnum` $\leq 5 \times 10^{15}$ is required to reach convergence and agreement with the experimental data for the 2D axisymmetric configuration. Likewise, Figure 5.14 (a) shows the effect of `fnum` on the predicted pressure coefficient C_p for the 2D external flow case e.I. Here a value of `fnum` $\leq 1 \times 10^{17}$ is required for convergence and a reasonable agreement with the experimental data. Using smaller values of `fnum` increases the number of simulation particles and thereby the computational cost. Hence, the above mentioned values of `fnum` are chosen as a trade-off for the simulation of the flow cases.

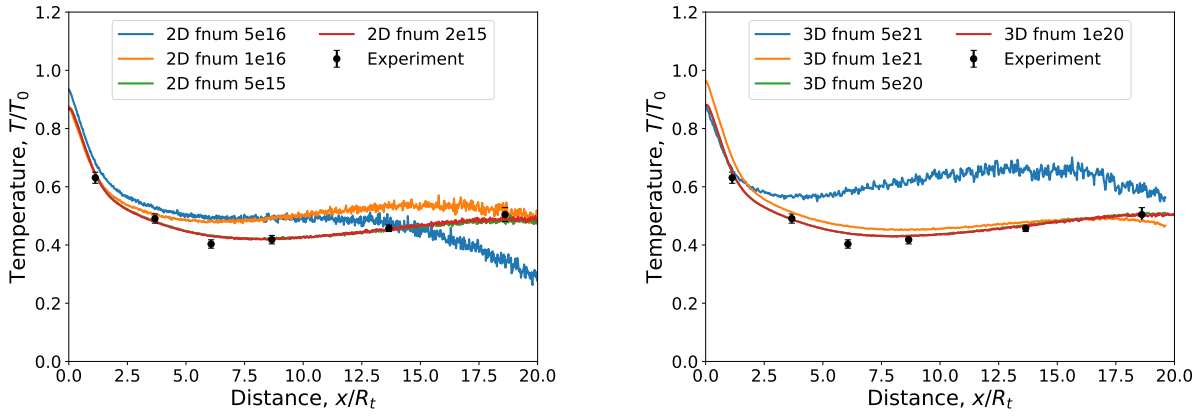

(a) (b)

Fig. 5.13. Effect of `fnum` on centerline rotational temperatures for case i.II. (a) 2D, (b) 3D.

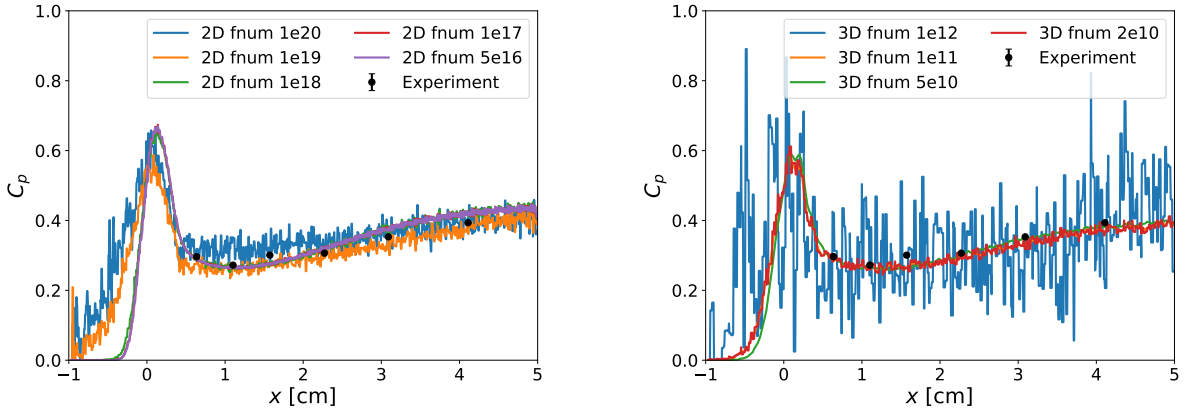

(a) (b)

Fig. 5.14. Effect of `fnum` on the pressure coefficient C_p for case e.I. (a) 2D (b) 3D.

5.4.2 Effect of DSMC grid size

A convergence study has also been performed with respect to the grid resolution of the DSMC simulation. The uniform regular grid is coarsened until the maximum grid size $\Delta x \leq \lambda_{min}$ is reached keeping the `fnum` value constant (trade-off `fnum`). Figure 5.15 shows the results achieved by the different grid sizes for case i.II and e.I, respectively. In the limit $\Delta x \leq \lambda_{min}$ there are no significant deviations between the calculations. Based on these cases, the optimal value of the grid size is $\Delta x \approx \lambda_{min}$ with `fnum` $\leq 5 \times 10^{15}$ for the internal and `fnum` $\leq 1 \times 10^{17}$ for the external 2D axisymmetric configurations. Compared to the previous configuration $\Delta x \approx \frac{1}{3}\lambda_{min}$ these parameters increased the simulation efficiency roughly by a factor of 3.5 for the internal case i.II and by a factor of 4.25 for the external case e.I. The 3D simulations are also carried out with $\Delta x \approx \lambda_{min}$ and the corresponding trade-off value of `fnum` is $\leq 5 \times 10^{20}$ for the case i.II and $\leq 1 \times 10^{11}$ for the case e.I, see Figure 5.13 (b) and Figure 5.14 (b).

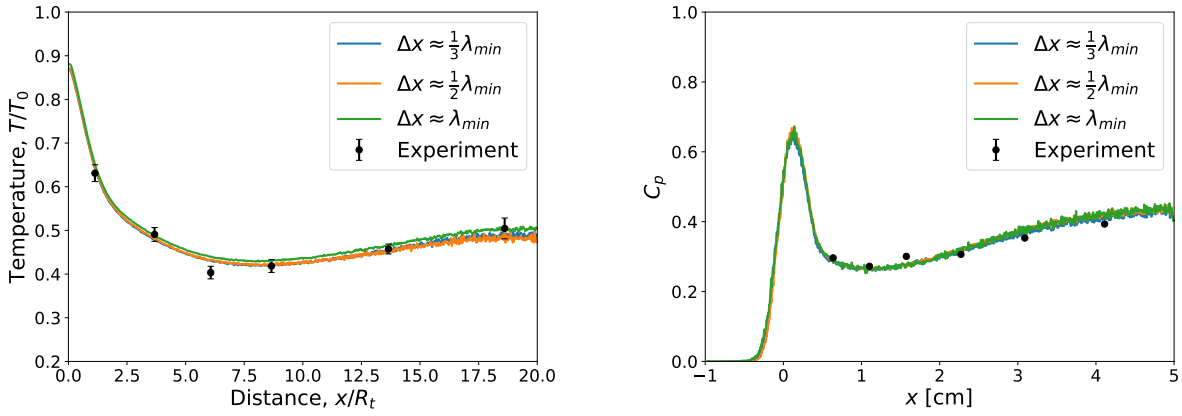

(a) (b)

Fig. 5.15. Effect of grid resolution on (a) centerline rotational temperatures for case i.II and (b) pressure coefficient C_p for case e.I.

The number of simulation particles and the computational effort could be further reduced without compromising the computational accuracy by using an adaptive mesh refinement technique. However, this technique is not considered in the thesis.

5.4.3 Effect of time step

The choice of the time step is another parameter, which can significantly affect the solution of the DSMC method. In a DSMC simulation, the time step Δt must be chosen in relation to the mean collision time t_{mct} [92]. The time step is estimated according to the following equation:

$$\Delta t \ \leq \ t_{\mathrm{mct}} \ = \ \frac{\lambda}{\bar{v}} \, . \tag{5.1}$$

Here, $\bar{v}$ represents the average thermal speed of the molecules, which is determined from the kinetic theory of gases, $\bar{v} = \sqrt{(8\,K_B\,T)/(\pi\,m)}$. In DSMC, a smaller time step requires a larger number of time steps needed to achieve a steady-state solution, corresponding to increased CPU time. Using much larger values of the time step may also increase the CPU time [175] since in DSMC the probability of collisions between two particles increases with the size of the time step. Therefore, a trade-off value of the time step Δt has to be estimated similar to the parameters in the previous subsection. The convergence study is performed by varying the time step Δt using the trade-off values of `fnum` and Δx. For the calculation of the mean collision time t_{mct} in Eq. (5.1), the mean-free-path value $\lambda = \lambda_{min}$ is chosen. The corresponding values of λ_{min} and t_{mct} estimated for different test cases are tabulated in Table 5.5. Figure 5.16 (a) shows the effect of the time step on the centerline rotational temperature of case i.II. For this case, it can be seen that in the limit of $\Delta x \leq t_{\text{mct}}$ there is no significant change observed in the results, which supports the assumption of Eq. (5.1). Figure 5.16 (b) depicts for case i.I the radial variation of the density near the throat region, where the density is higher since it is near to the continuum region and also due to the presence of compression waves near the throat. Here, it is obvious that a time-step value of $\Delta t \leq 0.7\ t_{\text{mct}}$ is required to attain converged results. Figure 5.16 (c) shows a similar trend in the calculation of C_p for case e.I particularly near the vertex region, where the density increases drastically due to the presence of a shock wave. Therefore, an optimal time-step value of $\Delta t = 0.7\ t_{\text{mct}}$ was chosen. This value increases the simulation efficiency by a factor of 1.1 for case i.I and by a factor of 1.2 for case e.I compared to the recommended value, i.e., $\Delta t = 0.25\ t_{\text{mct}}$.

Case	λ_{min} [m]	t_{mct} [s]
i.I	1.95e-5	4.3e-8
i.II	4.44e-5	1e-7
i.III	6.6e-5	1.5e-7
e.I	1.7e-6	3.5e-9
e.II	1.5e-5	3.16e-8

Tab. 5.5. Values of the minimum mean free path λ_{min} and the mean collision time t_{mct} estimated based on CFD calculations.

5.4.4 Gas-surface interactions

For the internal flow cases, the simulations are performed using various gas-surface interaction models described in Section 3.2. The surface collisions are treated as either fully specular, fully diffusive or a combination of both. Figure 5.17 (a) and (b) show the effect of these surface collision models on the centerline densities for cases i.I and i.III, respectively. In both cases, the simulation with a completely diffusive gas-surface interaction matches well with the experimental results. The simulations performed with a specular gas-surface interaction model yield a faster expansion of the flows compared

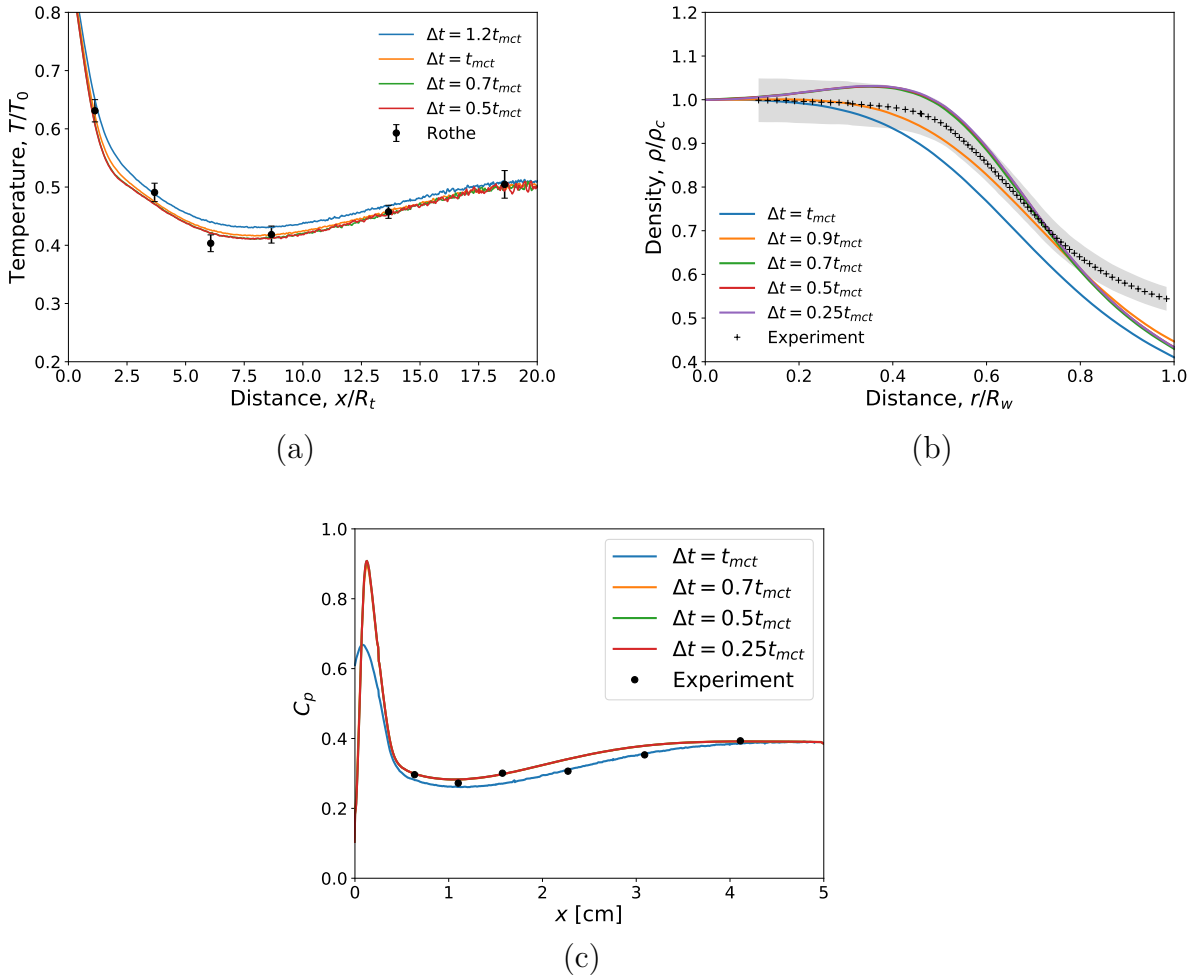

Fig. 5.16. Effect of time step on (a) centerline rotational temperatures for case i.II, (b) radial density variation at cross-section $x/R_t = 3.7$ for case i.I and (c) pressure coefficient C_p for case e.I.

with the experiment and the simulation relying on the diffuse surface interaction. For simulations with the surface interactions modeled by the combination of 50 % diffusive and 50 % specular collisions, the centerline density curve lies in between the completely diffusive and completely specular simulations. As the proportion of specular collisions increases, the curve shifts toward the completely specular simulation curve and vice-versa.

The effect of the gas-surface interactions is also studied regarding radial variations of the density at three different cross-sections of the nozzle. Figure 5.18 shows these distributions at the non-dimensional distances of $x/R_t = 3.7$ and $x/R_t = 6.2$ from the throat for cases i.I and i.III, respectively. Here, the densities are normalized by the corresponding density value at the axis ρ_c. The gray shaded regions in the plots represent the error margin in the experiments [171]. Similar trends as observed for the centerline data are visible in the results, i.e., the simulations with the diffusive-surface-interaction model matches well

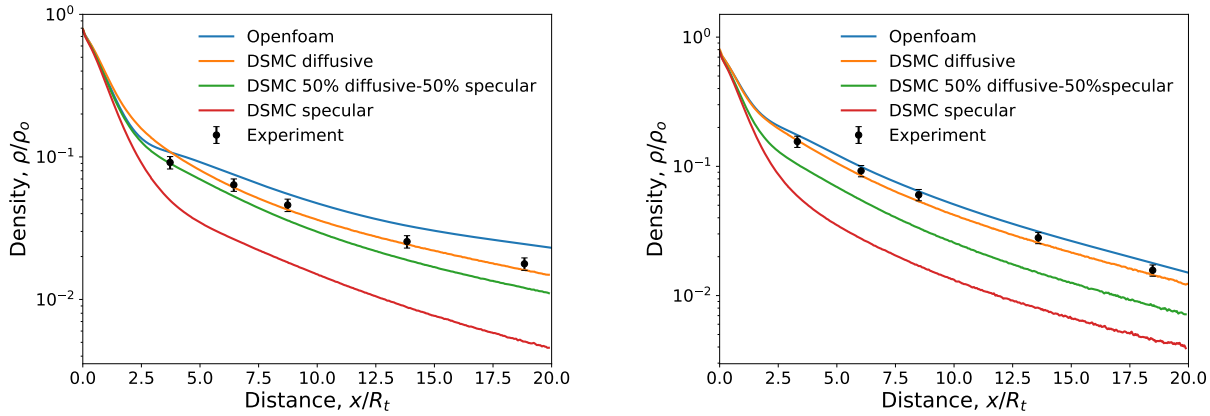

Fig. 5.17. Effect of gas-surface interactions on densities along the nozzle axis for the cases (a) i.I and (b) i.III.

with the experiment. For case i.I at the cross-section $x/R_t = 3.7$, which is close to the nozzle throat, there is a slight deviation of the simulation results in comparison with the experimental density trend shown in Figure 5.18 (a). The density first increases until a radial distance of $r/R_w = 0.4$ and then reduces with the distance toward the wall. This density hump is due to the presence of a weaker compression wave near the throat [105], which is also captured well by the continuum simulation. Furthermore, the density values do not coincide with the experiment near the nozzle wall. This deviation could be due to the collisional quenching effects of the electron beam technique used by Rothe [171], which reduces the quality of density measurements at higher pressure levels. As the flow of case i.I progresses in the downstream direction, the simulations match well with the experiments due to low pressure levels. Furthermore, for case i.III the quenching effects are reported to be negligible [171], which explains the good agreement of the simulation results with the experiments shown in Figure 5.18 (b) and (d). For the external flow cases shown in Figure 5.19, the gas-surface interaction models with fully diffusive and the interaction models consisting of fractions of specular collisions lead to a closer agreement with the experiments. Although the interaction models which are biased toward specular (e.g., 10 % diffusive and 90 % specular collisions) showed the best agreement with the experiments, the values of these specular to diffuse fractions can be case-specific and difficult to estimate. Therefore, it can be a safe option to assume the completely diffuse interaction model. Nevertheless, these two particular cases must the studied in more detail in the future.

Another important parameter in modeling the gas-surface interaction is the thermal accommodation coefficient. As described in Section 3.2, this parameter quantifies the energy exchange between the surface and the gas. For gas-surface interactions, which are fully diffusive, this parameter has a negligible effect on the density. However, it has an influence on the temperature. Figure 5.20 (a) and (b) show the effect of the thermal accommodation coefficient on the rotational temperature at the cross-section $x/R_t = 13.7$

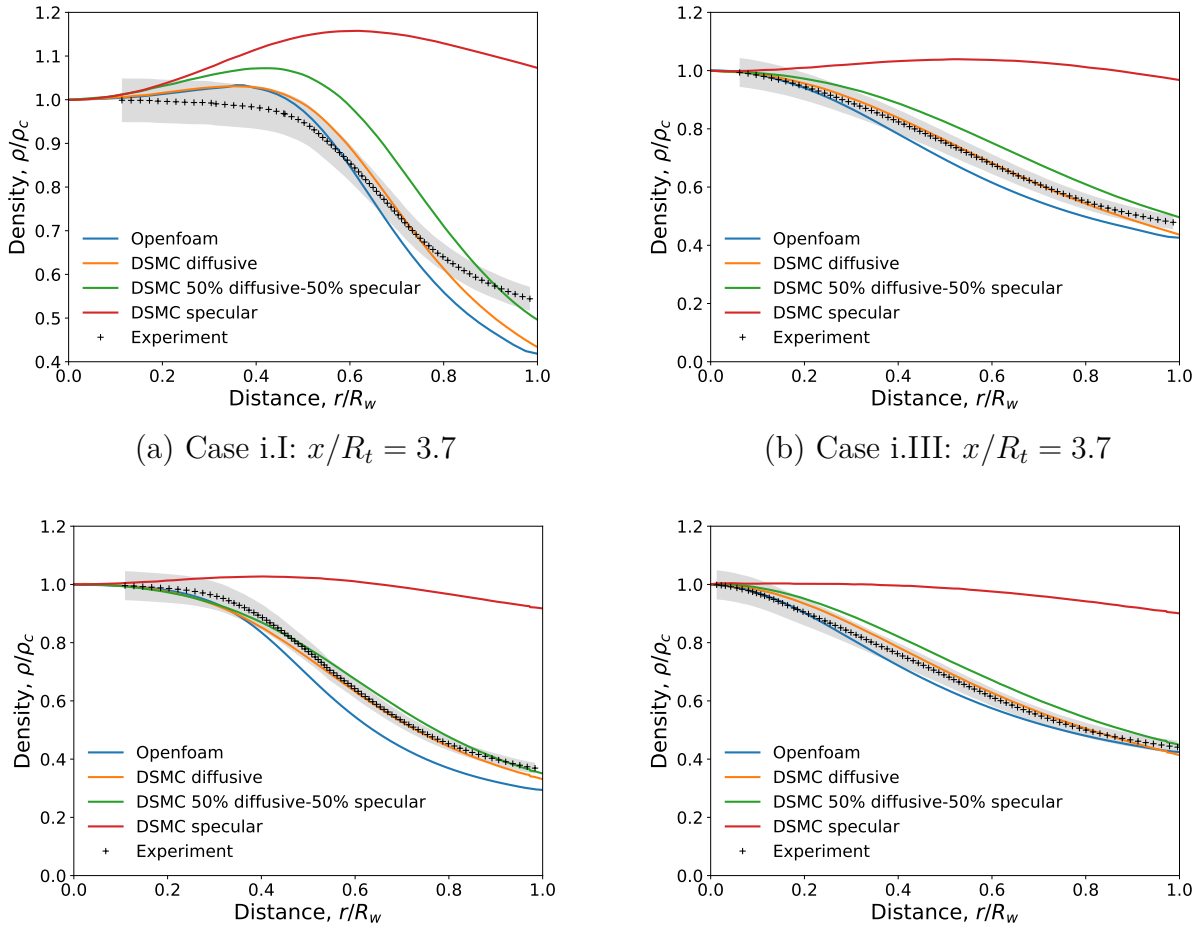

(a) Case i.I: $x/R_t = 3.7$

(b) Case i.III: $x/R_t = 3.7$

(c) Case i.I: $x/R_t = 6.2$

(d) Case i.III: $x/R_t = 6.2$

Fig. 5.18. Effect of gas-surface interactions on densities at different cross-sections for case i.I (left column) and case i.III (right column).

for cases i.I and i.III, respectively. The thermal accommodation coefficient only mildly affects the centerline temperature. However, near the wall it has a significant influence. It can be seen that the fully diffusive gas-surface interaction model with an accommodation coefficient of 0 % (adiabatic wall) was in close agreement with the experiment. As the value of the thermal accommodation coefficient increases, the temperatures near the wall increase and diverge from experiments. Although not shown, the effect of grid refinement near the surface on the results (Figure 5.17 – 5.20) was also studied. The grid near the wall was refined in the range of $\Delta x = \lambda_{min}$ to $\frac{1}{3}\lambda_{min}$ and within this limit the grid refinement has a negligible effect on the results.

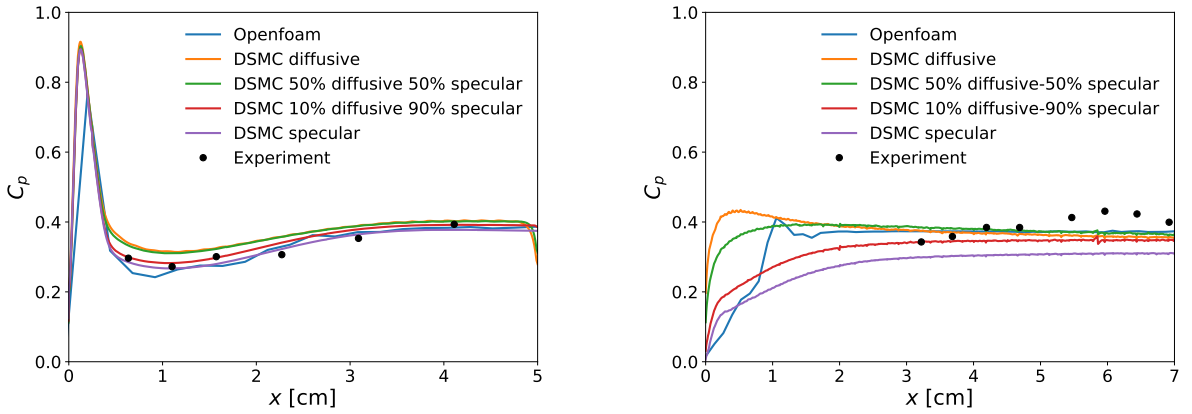

Fig. 5.19. Effect of gas-surface interactions on C_p for the cases (a) e.I. and (b) e.II.

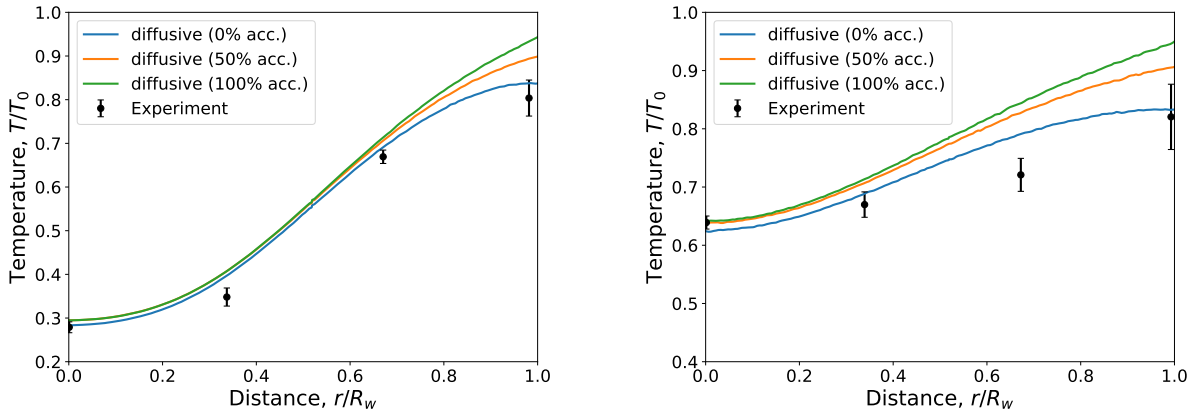

Fig. 5.20. Effect of thermal accommodation coefficient on the rotational temperature at the cross-section $x/R_w = 13.7$: (a) case i.I and (b) case i.III.

5.4.5 Collision models and energy exchange models

More sensitivity studies have been conducted considering the choice of the molecular models (i.e., VHS and VSS) and the energy exchange models (constant and variable relaxation). According to the evaluation in Section 5.4.4, the fully diffusive gas-surface interaction model with 0 % thermal accommodation is used in this study for the internal flow cases. The Maxwellian gas-surface interaction model with 10 % diffusive and 90 % specular is used for external flow cases. Figure 5.21 shows the comparison of the various parameters obtained using different molecular and energy exchange models with the experimental data for cases i.III and e.I, respectively. It can be seen that the results predicted by these different models lie within the experimental error estimates. However,

in order to rank the best DSMC simulation configuration for internal flows, the accuracy is quantified on the basis of the error estimation given by:

$$\text{error} = \frac{\psi_{\text{simulation}} - \psi_{\text{experiment(mean)}}}{\psi_{\text{experiment(mean)}}}, \tag{5.2}$$

where ψ can be any flow quantity such as the rotational temperature. Again, the collision and energy exchange models have a negligible effect on the density.

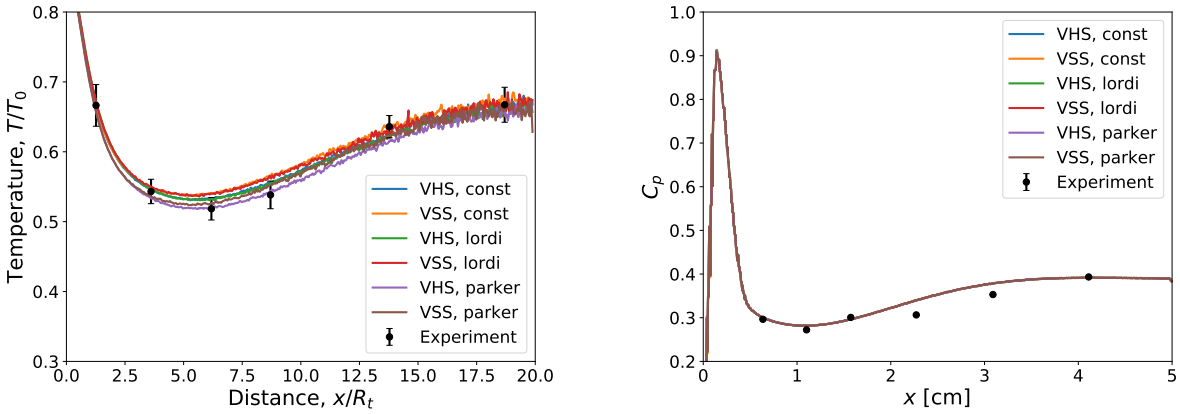

(a) (b)

Fig. 5.21. (a) Centerline rotational temperature profiles predicted with different collision models for case i.III. (b) Comparison of C_p distribution for various collision models for case e.I.

The simulation configuration with the variable hard-sphere model with a variable rotational relaxation (obtained using parameters from [107]) yield the best result for internal flow cases. For external flow cases the best result is achieved with the variable soft-sphere model with variable relaxation (obtained using parameters from [107]). However, in terms of performance the variable hard-sphere model with a constant rotational collision number (i.e., $\phi_{rot} = 0.2$) is the best choice for both internal and external cases as the simulation speed is roughly 1.5 times higher than the latter. More details on the simulation performance are discussed in Section 5.4.7.

5.4.6 DSMC sampling

As mentioned in Section 3.4, the macroscopic flow properties shown above are obtained in the DSMC method by averaging the microscopic properties per grid cell. However, DSMC being a probabilistic method is very much prone to statistical fluctuations. The statistical noise in the flow field is typically filtered out by time averaging of the cell properties to obtain mean macroscopic properties. This procedure is performed after a steady state of the flow is established. In Figures 5.13 and 5.14, it was evaluated that a sufficient number of particles (defined in terms of `fnum`) is required to obtain reliable macroscopic

values. Furthermore, it can be observed from these figures that using less particles than the trade-off values also induces statistical noise. In this section, the statistical error associated with DSMC according to the effect of the number of particles per cell N_c and the number of time steps N_T used for averaging is studied. Here, the root-mean-square (rms) error is used as an indicator to quantify the statistical fluctuations. The relative root-mean-square error ϵ_ψ in dimensionless form is given by:

$$\epsilon_\psi = \sqrt{\frac{1}{N_{cell}} \sum_{i=1}^{N_{cell}} \left(\frac{\psi_i - \psi_{ref,i}}{\psi_{max}} \right)^2} . \tag{5.3}$$

Again, ψ can be any macroscopic property where ψ_{max} is its maximum value in the flow field and N_{cell} is the total number of grid cells in the simulation domain. ψ_i and $\psi_{ref,i}$ represent the computed and the reference solutions in the grid cell i. A sample size S is defined as the product of N_c and N_T through which a macroscopic property is sampled. In the study, it was observed that the translational temperature had a higher sensitivity to the statistical fluctuations and hence it is chosen to describe the results. The rms-error ϵ_T based on the translational temperature is determined for different values of S obtained by varying N_c and N_T, see Figure 5.22. The reference solution used to estimate the rms-error has a sample size of $S = 2700\,k$ ($N_c = 270$, $N_T = 10,000$) for the internal flow and $S = 1800\,k$ ($N_c = 180$, $N_T = 10,000$) for the external flow case. Peak temperatures of 300 K and 4100 K were used for normalizing the rms-errors for internal and external cases, respectively.

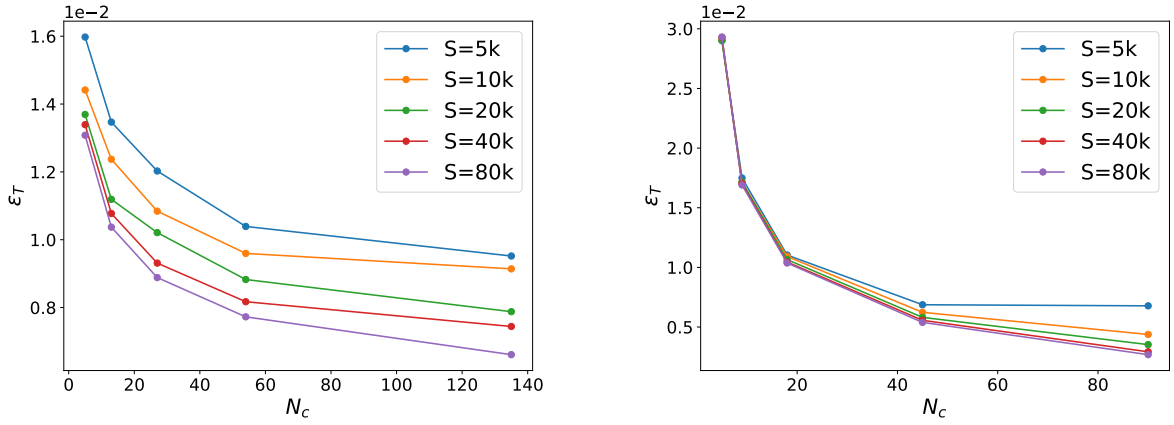

Fig. 5.22. RMS error ϵ_T based on the translational temperature for (a) case i.III and (b) case e.I.

Figure 5.22 shows that increasing N_c has a major effect in reducing the statistical errors. For a fixed value of N_c the rms-error reduces until it reaches an asymptotic value. This trend was also observed in the study by Chen and Boyd [142]. The computational cost for a particular sample size S is observed to be constant for small to large values of N_c.

Therefore, it is advantageous to use greater values of N_c for a specific S leading to the smallest rms-error at given CPU-time resources.

5.4.7 Computational performance and energy consumed

This section deals with the performance and computational costs of the DSMC simulations running on the high-performance computer HSUper at the Helmut-Schmidt University. HSUper consists of 581 nodes in total, 571 compute nodes with 256 GB RAM per node, 5 nodes with 1 TB RAM per node and 5 nodes with 2 NVIDIA A100 GPUs. Each node contains two sockets equipped with Intel Xeon Platinum 8360Y (36 cores, 2.4 GHz) processors, hence 72 physical cores or 144 virtual CPUs via hyperthreading. The memory is provided by 16×16 GB DDR4 RDIMM 3200 MHz ECC-registered modules. HSUper utilizes InfiniBand HDR, 100 Gb/s, non-blocking fat tree networking. The test cases with the optimized simulation setup (i.III and e.I) were used to study the performance.

The energy consumption of the CPU and DRAM reported in the following are based on the running average power limit [176] as well as the CPU time of the job reported by the SLURM workload manager. In order to keep the result comparable for internal and external flow cases with different configurations, the run-time is normalized in all cases to 1 core/node. SPARTA uses a hierarchical Cartesian grid, which is not a body-fitted grid. Since a big portion of the grid points is therefore outside the computational domain and without simulation particles, the usage of load balancing methods is necessary to optimize computational efforts.

Figure 5.23 compares the strong scaling results on 1 core up to 144 cores equivalent to 2 nodes on HSUper using static and dynamic load balancing for the internal and external cases. The dynamic load balancing had a huge impact on the speedup of the simulation. The effect of the dynamic load balancing is stronger for the internal case than for the external flow because the external case is a hypersonic flow and due to the very high flow velocity the computational domain gets saturated very quickly with sufficient simulation particles. Thus, the static load balancing at the beginning of the simulation already leads to good results contrary to the internal case where the flow velocity is much smaller than in the external case and the simulation needs therefore a much longer time to reach the steady-state solution. In Figure 5.23 (c) and (d), a similar behavior is also observed in the energy consumption results, which is strongly related to the run-time.

Weak scaling is achieved by varying the parameter `fnum`, e.g., the number of particles is increased by a factor of three when running on three cores, compared to the single-core case. The results also shown in Figure 5.23 are in full agreement with the argumentation given for the strong scaling results. Note that the `fnum` parameter decreases correspondingly as the number of cores increases, e.g., the `fnum` value for 1 core is decreased by a factor of 3 for 3 cores. So the number of simulation particles increases for 3 cores and the number of simulation particles per core remains the same as for 1 core. The `fnum` parameter is set for 9, 18, 36 and 72 cores, correspondingly. Note that in Figure 5.23 (d) for the internal test case, the weak scaling configuration starts from a different number of particles on 1 core than the strong scaling configuration ($\texttt{fnum} = 5 \times 10^{15}$) in Figure 5.23 (c).

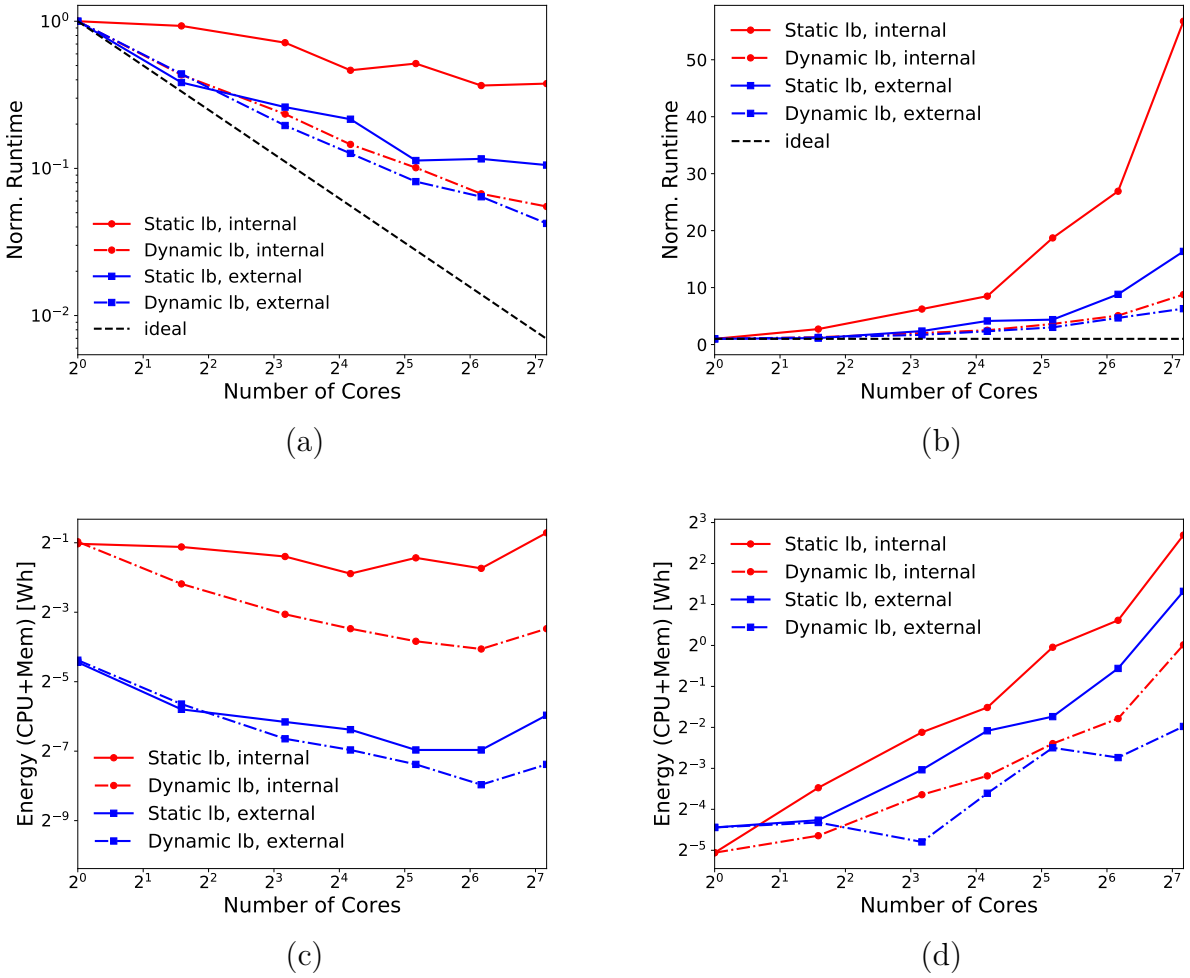

Fig. 5.23. Scaling results on up to 144 cores. Left column: strong scaling. Right column: weak scaling. (a) & (b) normalized run-time. (c) & (d) energy consumption for one time step.

Figure 5.24 demonstrates the strong scaling results on 1 to 16 nodes (i.e. up to 1152 cores). It has to be mentioned that all 72 cores of each HSUper node are occupied for the simulation. Unlike in Figure 5.23 (c) and (d), the energy consumption on more than one node increases constantly in Figure 5.24 (c) and (d). By using a few processors of a node, the other processors of the node are in the idle mode and still consume energy. Therefore, using more cores of one node, which leads to a smaller run-time may, require less energy, because the reduction of the computation time may compensate the effect of using more cores. Figure 5.24 (c) shows that this is not the case when using more than one node. Considering simulations using 1 or 2 nodes, if the speedup of the simulation from 1 to 2 nodes would be exactly 2, then the energy consumption would be the same, since the speedup of the simulation would fully compensate the additional energy consumption of more nodes. But as can be seen in Figure 5.24 (a), the speedup of the simulation from 1

to 2 nodes is less than two. So the computational time reduction can not compensate the energy consumption of the additional node and therefore the total energy consumption increases by a factor of 2.

It can be summarized that since an entire node is always allocated exclusively, the faster the simulation is finalized on it, the less energy is used and this rationalizes the decrease in energy consumption up to 72 cores. For more cores the energy consumption increases, because more nodes are allocated. Based on this explanation, in the SPARTA cases it is necessary in terms of energy consumption to always fully use all cores of a node as long as runtime decreases are observed. The weak scaling results in Figure 5.24 are in full agreement with the argumentation given for the strong scaling.

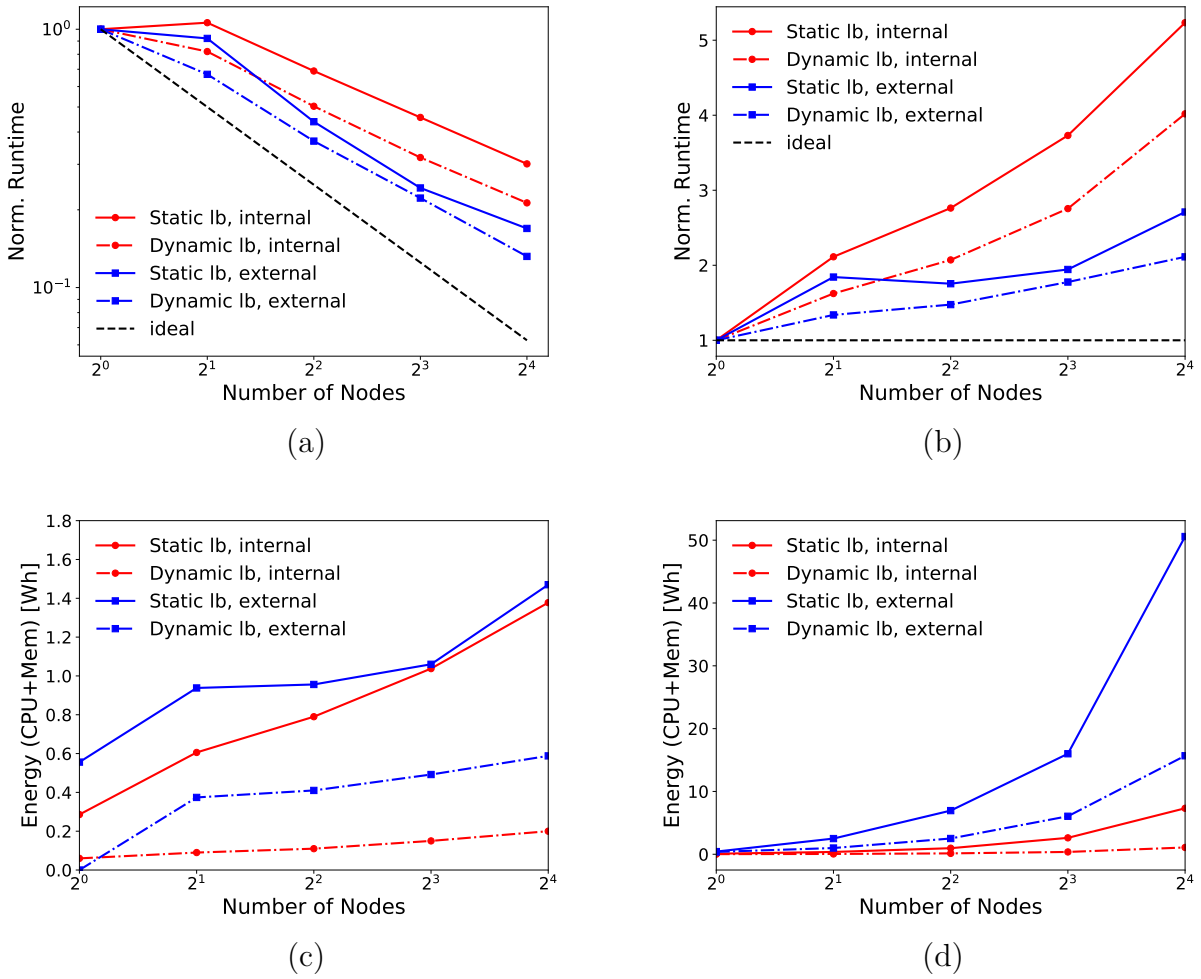

Fig. 5.24. Scaling results on 1 to 16 nodes. Left column: strong scaling. Right column: weak scaling. (a) & (b) normalized run-time. (c) & (d) energy consumption for one time step.

5.5 Conclusions

The rarefied nitrogen gas flow through a convergent-divergent nozzle (internal flow) and over a conical body (external flow) were numerically investigated using a continuum-based Navier-Stokes solver and a stochastic Boltzmann solver (DSMC) for different Knudsen- and Reynolds-number regimes. The CFD solvers, `sonicFoam` and `rhoCentralFoam`, were first evaluated for their predictive capability in high-speed compressible flow scenarios. The numerical results were validated against the available experimental data. In the higher Knudsen number range ($Kn > 0.1$), the DSMC method demonstrated superior accuracy in predicting state properties such as density, pressure, and rotational temperature. However, in the continuum regime ($Kn < 0.1$) the Navier-Stokes solver exhibited higher accuracy and computational efficiency than the DSMC method. Consequently, for internal-flow cases encompassing variable Knudsen number regimes, a one-way-coupled hybrid approach combining the Navier-Stokes and the DSMC solver was preferred to accurately resolve the flow in the entire domain while mitigating computational costs.

The sensitivity study of the DSMC simulations unveiled several essential insights, particularly regarding parameters such as the ratio of real molecules to simulation particles `fnum`, the grid size, the time step, the sampling and the surface and molecular collision models:

- Threshold values for `fnum` or the number of particles to approach optimal simulation accuracy were investigated and are reported for both internal and external flow cases in 2D and 3D configurations.
- The grid dependence study revealed that varying grid sizes Δx of the DSMC domain in the range of the minimum mean free path λ_{min} have negligible effects on the results.
- From the time step sensitivity study, it was found that the value of the time step Δt must definitely be a fraction of the mean collision time t_{mct}. For resolving near-continuum flow regions in DSMC domains, Δt values of 0.7 t_{mct} or smaller are required. However, for highly rarefied regions the time-step size can be relaxed to $\Delta t = t_{\mathrm{mct}}$.
- Gas-surface interactions play a major role in obtaining accurate results. For all cases the results obtained with the fully diffusive interaction model (isotropic scattering) showed good agreement with the experiments. Furthermore, the adiabatic nature of the wall in the internal-flow scenarios necessitates the utilization of a diffusive model with incomplete thermal accommodation, accomplished through the CLL model.
- The sensitivity study on molecular and energy exchange models did not yield major significance on the results and all predictions lie within the experimental margins. However, from the performance point of view, the VHS collision model with constant relaxation is found to have a higher computational speed for all cases.
- The statistical error analysis of the DSMC method showed that the translational temperature had the highest sensitivity to statistical fluctuations. The study favored

the use of more particles per cell N_c compared to the number of sampling time steps N_T for a specific sample size $S = N_c \times N_T$. This approach significantly reduces statistical errors while maintaining the same computational costs for the sample size.

In addition, performance studies concerning both strong and weak scaling were conducted to analyze the computational speedup and the energy consumption of DSMC simulations. This investigation revealed that the dynamic load balancing feature of SPARTA provided the most efficient solution. The iterative study exploits an optimal parametric setup for hybrid DSMC/CFD simulations without compromising the computational efficiency.

This benchmarked hybrid methodology holds great potential for simulating molecular beam experiments, particularly those involving gas flows spanning a wide Knudsen number range. In single-particle imaging (SPI) experiments, molecular beams are typically generated using devices such as aerodynamic lens systems or cryogenic buffer gas cells to deliver nanoparticles into vacuum [35, 36]. For this purpose, the hybrid DSMC/CFD methodology has been integrated into the simulation framework developed in this work to accurately capture such multiscale flow phenomena in aerosol injection systems used for SPI. The validation of this integrated framework is presented in Chapters 6 and 7, along with its application to study gas-particle interactions and support the optimization of injector designs.

6 Simulating nanoparticles through an Aerodynamic Lens Stack injector [1]

This chapter presents the validation of the improved simulation framework for predicting nanoparticle beam characteristics as they pass through an Aerodynamic Lens Stack (ALS). The typical ALS design and its integration in SPI experiments were detailed in [37]. Achieving high-quality particle beams in SPI applications requires maximizing particle density at the interaction point to increase hit rates while minimizing carrier gas density to reduce background scattering. This dual requirement often necessitates shifting the particle beam focus away from the ALS exit. Experimentally optimizing ALS designs across a broad parameter space is challenging and time-consuming. Computational modeling offers a fast and efficient alternative for exploring the influence of key parameters, such as inlet pressure, flow rate, and carrier gas properties on particle-beam focusing and transport.

The simulation approach is based on the hybrid DSMC/CFD methodology coupled with Lagrangian particle tracking. The individual components of the simulation framework were described in the preceding chapters: Chapter 2 introduced the CFD solver for continuum gas flows, Chapter 3 described the DSMC and hybrid DSMC/CFD methods for rarefied regimes, and Chapter 4 focused on modeling particle transport under multiscale flow conditions.

The objective of this chapter is to validate the predictive simulation strategy for ALS systems and to show that it remains accurate across a wide range of operating conditions and flow regimes. This work builds on the previously validated hybrid DSMC/CFD framework described in Chapter 5, initially benchmarked using gas-dynamic nozzle configurations [171], and now extended to ALS systems. The full simulation pipeline is applied to representative ALS geometries to assess the predictive accuracy of particle beam profiles under varying experimental conditions, including different particle sizes and inlet pressures. Simulation results are compared with experimental measurements [34] to evaluate accuracy and reliability. Furthermore, predictions obtained using the hybrid flow fields are contrasted with those based solely on CFD, thereby revealing the limitations of continuum-based approaches in the presence of rarefaction.

Of particular interest is the focusing behavior of nanoparticles in transitional and free-molecular regimes, which remains largely unexplored [156]. These regimes challenge the

[1] This chapter is based on the publication: S. K. Peravali, A. K. Samanta, M. Amin, P. Neumann, J. Küpper and M. Breuer, "An improved simulation methodology for nanoparticle injection through aerodynamic lens systems", *Physics of Fluids* **37** (3), 033380, (2025) [74]. I am the principal contributor to this publication. I contributed in drafting the original manuscript and overseeing its review and editing processes. I was also deeply involved in the visualization and validation of data, the development and application of the methodology, and conducting investigations. Additionally, I contributed in the formal analysis and conceptualization of the paper.

applicability of continuum-based models and require physically accurate descriptions of molecular interactions. In this work, the gas flow is resolved using a hybrid DSMC/CFD approach for multiscale regimes, while various molecular drag models are evaluated – including the correction scheme proposed in Chapter 4, which improves the drag estimation under low-speed, highly rarefied conditions. For cases where the entire ALS domain exceeds the continuum breakdown threshold, full-domain DSMC simulations are conducted to capture the rarefied gas dynamics more reliably.

The structure of this chapter is organized as follows. Section 6.1 describes the test case configurations used for the simulations, along with the corresponding experimental setup and procedures. Section 6.2 outlines the numerical setup, including solver configurations for both CFD, DSMC and the hybrid variant. Section 6.3 presents the results and discussion, beginning with a representative case that illustrates the post-processing workflow and validation strategy. The subsequent sections, Section 6.3.1 and Section 6.3.2, evaluate the hybrid flow modeling approach and the drag force models introduced in Chapter 4 by comparing simulated and experimental particle beam profiles. Section 6.3.1 focuses on a case operating in the multiscale regime, where both continuum and rarefied flow regions coexist. The hybrid DSMC/CFD method is employed to resolve transitional gas dynamics and to predict the nanoparticle beam evolution, with results compared against pure CFD predictions to assess the benefit of hybrid modeling. Section 6.3.2 examines a highly rarefied flow scenario in which the entire domain exceeds the continuum breakdown threshold. The DSMC method is used within the full domain, and its predictions are compared with those from pure CFD. Additionally, the drag force correction scheme proposed in Chapter 4 for low-speed, highly rarefied flows is evaluated against alternative models.

6.1 Test case and experimentation

The nanoparticle beams were generated using the experimental setup shown in Figure 6.1. Polystyrene spheres (PS) were aerosolized at pressures of about 10^5 Pa and passed through a differentially-pumped skimmer assembly to reduce gas-load and pressure in the experiment. The particles were focused, through an ALS, into the ultra-high vacuum detection chamber ($p \approx 10^{-1}$ Pa). These experiments were carried out for different ALS inlet-gas pressures (p_{in}) and different particle sizes summarized in Table 6.1 along with the flow Knudsen numbers (Kn) and particle Knudsen numbers (Kn_p) at the inlet of the ALS.

It can be seen that for the particle size of 25 nm, the experiments were conducted at different inlet pressures compared to the particles sizes 69 nm and 42 nm. This difference is due to the higher divergence of the 25 nm particle beam at pressures below 50 Pa, where reliable data could not be collected. For this reason, experiments with these smaller nanoparticles ($\leq$ 25 nm) were carried out over a higher pressure range than those with larger particles [34].

The particle beam profiles were obtained through particle-localization microscopy [177] at different distances from the exit of the ALS. Detailed descriptions of the ALS geometry

used in the experiment, the experimental procedure, and the analysis of the experimental data were described elsewhere [34].

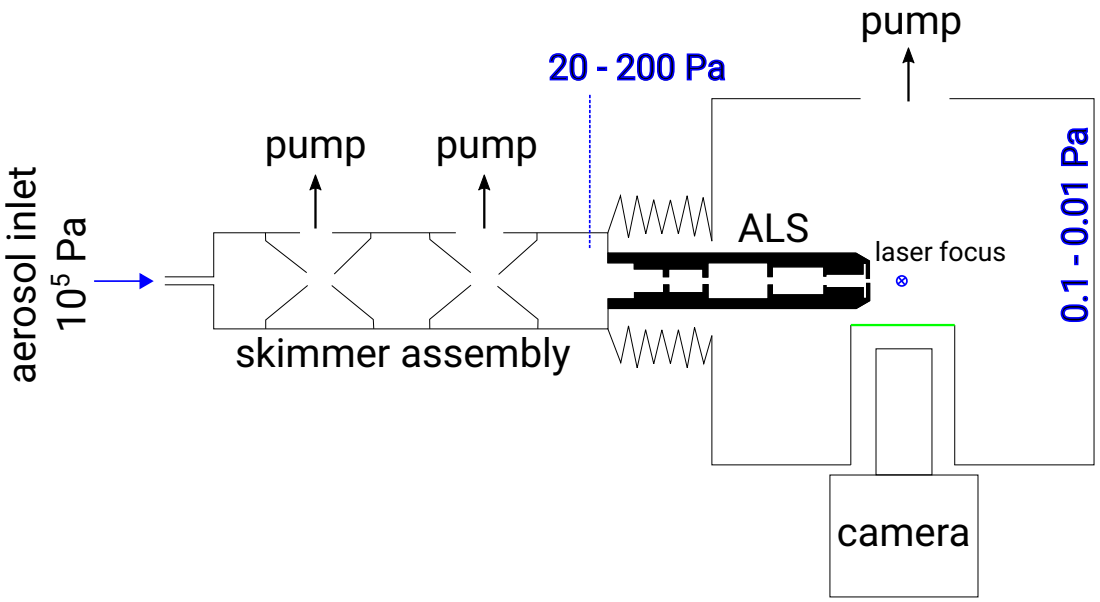

Fig. 6.1. Schematic of a typical experimental setup used in the particle-beam evolution measurements [34]. The setup consists of a double skimmer setup with adjustable pumping, an aerodynamic-lens-stack assembly for particle-beam generation, and the optical scattering setup and particle-localization microscopy inside a high-vacuum chamber.

Particle size (nm)	Inlet pressure, p_{in} (Pa)	Kn	Kn_p
69	180	0.0241	523.87
	55	0.0788	1714.50
	20	0.2168	4714.88
42	180	0.0241	860.65
	55	0.0788	2816.68
	20	0.2168	7745.87
25	200	0.0213	1279.196
	150	0.0289	1735.075
	50	0.086	5205.225

Tab. 6.1. Gas-flow and particle parameters of the experiments.

6.2 Simulation settings for fluid flow

In the experimental setup considered, the particle volume fraction in the gas–particle mixture is very low. Consequently, particle–particle interactions and the influence of

particles on the gas flow are assumed to be negligible. This allows for a decoupled treatment of gas and particle dynamics. A two-step approach, as described in Chapter 4, is therefore adopted to compute the gas–particle behavior. The gas flow field is resolved using CFD, DSMC, or the hybrid DSMC/CFD method depending on the local Knudsen number regime, as introduced in Chapters 2 and 3. The relevant models for particle transport, including drag and other forces, are discussed in detail in Chapter 4.

6.2.1 CFD

For the experiments with higher inlet pressures, i.e., when the Knudsen numbers Kn of the flow field throughout the ALS and near its exit are small ($Kn < 0.1$) the flow can be described as continuum ($0 < Kn < 0.01$) or in a slip regime ($0.01 < Kn < 0.1$). For these regimes, the flow field can be computed by solving the Navier-Stokes equations. The continuum gas flow field is computed using the finite-volume software OpenFOAM [49]. Since the flow through the ALS transits from subsonic to supersonic speeds in the streamwise direction, the flow has to be assumed as compressible. The density-based transient solver (`rhoCentralFoam`), which was evaluated in Chapter 5 was utilized. Detailed information on the solver settings, e.g., discretization, interpolation and algorithms can be found in Chapter 2. These are implemented through the `fvSchemes` and `fvSolution` dictionaries in OpenFOAM (see Appendix A). The boundary conditions for the simulation case are presented in Table 6.2.

Boundary	**U**	**P**	**T**
Inlet	zero gradient	fixed value	fixed value
Outlet	zero gradient	wave transmissive	zero gradient
Wall	no-slip	zero gradient	fixed value

Tab. 6.2. Boundary conditions for the ALS flow.

Since in this case the Reynolds number is very low ($Re < 10$), the flow is assumed to be laminar and thus a turbulence model is not required. Furthermore, the transport properties are estimated using the Sutherland transport model with a Sutherland coefficient $A_s = 1.41716 \times 10^6$ and a Sutherland temperature $T_s = 111$ K for nitrogen gas [172].

For simulating gas flows through ALS geometries [34, 37] using CFD, computational grids are generated using the `blockMesh` and `snappyHexMesh` utilities in OpenFoam. Since the ALS geometries are axisymmetric, structured body-fitted standard 3D O-grid type grids are generated as shown in Figure 2.1. The vacuum chamber in this simulation is represented by a cylindrical mesh of radius 5 mm and length of 10 mm from the ALS exit ($z = 0$). Here, the wave transmissive outlet boundary condition is applied [73].

The entire ALS mesh contains a total of approximately 2.44×10^6 cells, which is based on grid-independence studies as shown in Figure 6.2. In this grid study, the root-mean-square error (RMS-error) of the ALS centerline velocity magnitude ϵ_U is calculated. By comparing results obtained by different grid resolutions with the reference simulation

conducted on a fine grid consisting of 10×10^6 cells, it is obvious that the applied grid is appropriate.

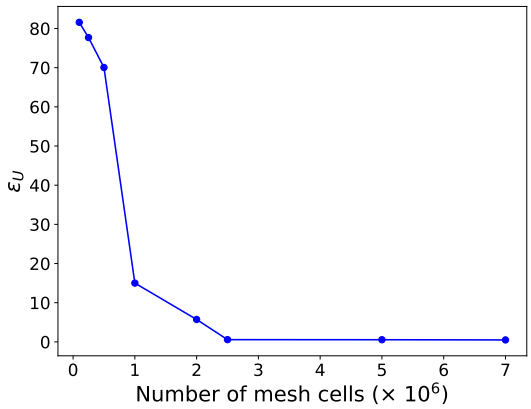

Fig. 6.2. Grid-independence study of the ALS grid.

Numerical convergence is ensured by monitoring key parameters such as pressure, velocity, and temperature – until they reach a steady state during the transient simulation.

6.2.2 DSMC

The pressure at the inlet of the ALS is one of the major tuning factors of particle injection in SPI experiments. Sometimes very low inlet pressures $p_{in} < 50$ Pa are used to reduce the background X-ray scattering. For such low pressures, the gas flow corresponds to a large mean free path between gas molecules and the Knudsen number is larger than 0.1. Pure CFD simulations cannot capture the flow physics of such a rarefied gas. To resolve the flow field in these regimes, the direct simulation Monte Carlo (DSMC) method presented in Chapter 3 is often a good choice [43]. The evaluation study presented in Chapter 5 established practical guidelines for conducting accurate and computationally efficient DSMC simulations, which are followed in the present work. The DSMC simulator SPARTA [90] uses a Cartesian grid unlike OpenFoam. To adequately resolve the rarefied flow domain and to assure a grid that fits to the entire range of flow Knudsen numbers, a regular grid of size $\Delta x = 5 \times 10^{-5}$ m is used. The time step Δt used in the simulation is calculated by $\Delta t = 0.7\,\Delta x/\overline{v}$ where $\overline{v} = \sqrt{8k_BT/(\pi\, m)}$ is the mean thermal speed of the gas molecules. This calculation yields an approximate time step of 1×10^{-7}s. The fully diffusive (isotropic scattering) gas-surface interaction model is used to model the interaction between ALS walls and the gas. The no-time-counter (NTC) method is employed for collision sampling along with VSS molecular model. The Larsen and Borgnakke model with constant relaxation is applied to handle the internal energy exchange [73]. The number of DSMC particles per grid cell $N_c \approx 1650$ is used and the number of sampling time steps N_T used were $40,000$ thereby giving a sample size $S = N_c \times N_T = 66 \times 10^6$.

6.2.3 Hybrid DSMC/CFD

As previously discussed in Chapter 3, while the DSMC method is highly effective for rarefied gas flows, it becomes increasingly inefficient in near-continuum regimes due to elevated collision rates and the need for extensive averaging to suppress statistical noise. In such cases, continuum-based solvers like those based on the Navier-Stokes equations remain more practical and computationally efficient. For experiments with intermediate pressures at the ALS inlet, i.e., 50 Pa $\leq$ p_{in} $\leq$ 180 Pa, it was observed that the flow through the ALS has a variable Knudsen number regime, i.e., it changes from continuum to transition and free-molecular-flow regime. Therefore, the hybrid DSMC/CFD methodology described in Section 3.5 was employed to address the limitations of applying either method alone. The respective simulation settings outlined in Sections 6.2.1 and 6.2.2 were applied to the CFD and DSMC regions. The transition between continuum and rarefied regimes was determined using the breakdown Knudsen number, Kn_B, calculated according to Eq. (3.34). A breakdown of the continuum assumption was assumed wherever $Kn_B > 0.05$, and the domain was accordingly partitioned. This approach enabled the construction of a smooth, contiguous multiscale flow field (see Figure 3.5). The accuracy and computational efficiency of this hybrid methodology were validated in the previous chapter (Chapter 5) using a gas-dynamic nozzle case, demonstrating that it provides a reliable balance between predictive accuracy and computational cost.

6.2.4 Particle transport

The particle trajectories are computed using a Langevin framework based on the simulation tool `CMInject`, described in Chapter 4. A one-way coupling between the particulate phase and the fluid phase is employed, where the fluid exerts forces on the particles, but the particles do not influence the flow. This assumption is justified by the low particle volume fraction [148], and it also permits neglecting particle-particle collisions [149], thereby simplifying the simulation procedure. `CMInject` reads flow field data from CFD, DSMC, or hybrid DSMC/CFD simulations, provided in the form of Cartesian regular grid data, and uses it to evaluate the forces on particles. Multiple drag models are applied depending on the local flow regime, as described in Sections 4.2.1 to 4.2.3. Due to the extremely small size of the particles, Brownian motion is non-negligible and is modeled as described in Section 4.2.3.1.

6.3 Results and discussion

The numerical methodologies described are utilized to simulate the particle-beam evolution at different conditions presented in Table 6.1. Figure 6.3 exemplarily shows the flow field and the corresponding nanoparticle trajectories throughout the computational domain for the 25 nm polystyrene spheres (PS) at an inlet pressure of $p_{in} = 150$ Pa. Here, r represents the radial and z the axial coordinate of the flow domain. The flow field predicted by the hybrid DSMC/CFD method is depicted by the axial velocity v_z representing the main

flow direction and the particle trajectories are calculated by molecular drag force models (Section 4.2.2).

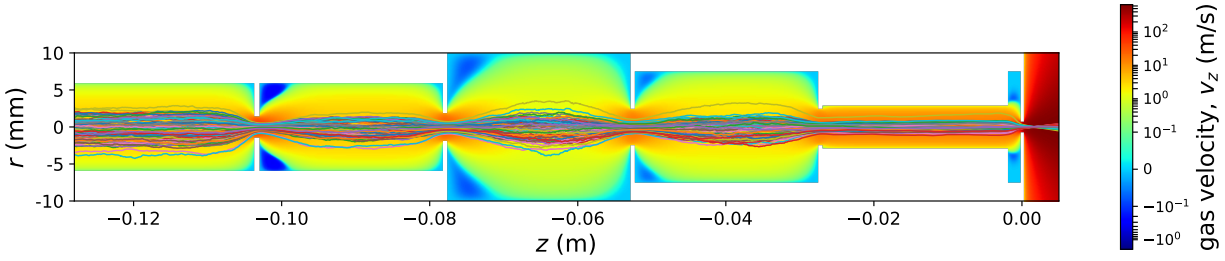

Fig. 6.3. Simulated trajectories (colored lines) of the 25 nm PS through the aerodynamic-lens stack drawn on top of the gas-flow field (p_{in} = 150 Pa) visualized by the axial velocity in a logarithmic color scale.

The exit of the ALS is at $z = 0$. The flow domain defined by $z > 0$ represents the vacuum chamber, where the gas flow from the ALS expands at supersonic speeds. Figure 6.4 (a) is the zoomed-in view of Figure 6.3, which shows the simulated particle trajectories focusing (converge to a minimum beam width) and de-focusing inside the vacuum chamber. In the vacuum chamber, the particle beam widths are measured at different positions starting at $z = 1$ mm and onwards. The particle beam evolving from the exit of the aerodynamic lens has a Gaussian-like distribution [34]. Therefore, the width of the particle beam is designated by the full-width at half-maximum (FWHM). The widths of the simulated particle beam at the corresponding experimental positions are compared with the experimental data in Figure 6.4 (b). In the current case, the beam profiles obtained by simulation show good agreement with the experimental data.

For every experimental case in Table 6.1, 10^4 particles were simulated with an initial radial velocity of $v_r = 0$ and an axial velocity following a normal distribution with a zero mean and a standard deviation of 10 m/s. The particles are positioned at the ALS inlet with a Gaussian distribution centered around $r = 0$ and FWHM of 0.0023 m. For particle numbers above 1000, the simulated beam profiles do not change significantly. Thus, with ten times more particles, it is ensured that the statistics are fully converged.

However, the level of accuracy of the simulation shown above highly depends on choosing the right modeling approach, which also varies for different experimental conditions such as inlet pressure or particle size. Potential sources of error include experimental uncertainties – such as differences between the measured upstream pressure and the actual inlet pressure. For every test case, results are averaged and both the mean and standard deviation are estimated to quantify this uncertainty as shown in Figure 6.4 (b). Other sources of error include limitations in the numerical models (e.g., approximations in the drag force models and the flow modeling approach) and variations in boundary conditions. To ensure a reliable flow modeling approach, necessary steps have been taken to minimize these discrepancies through careful calibration of simulation parameters and sensitivity analyses. For details, refer to Peravali et al. [73].

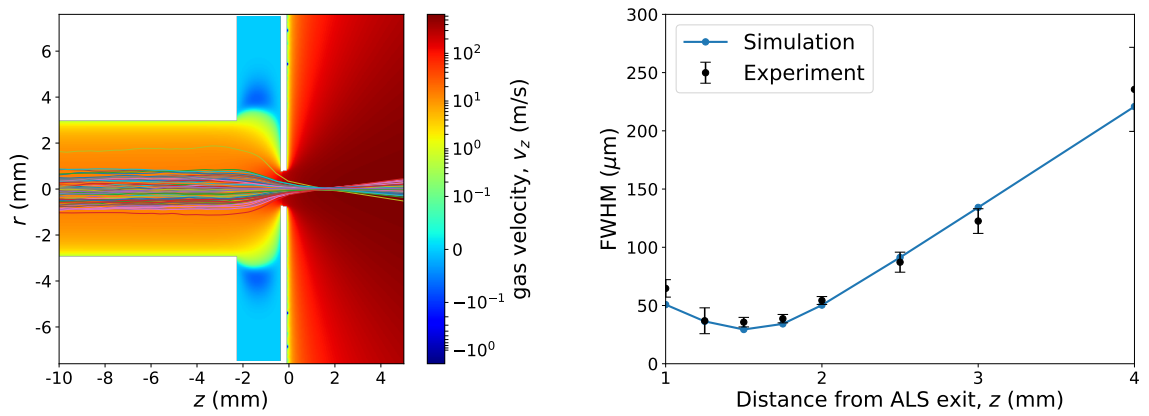

(a) (b)

Fig. 6.4. (a) Zoom-in view of the ALS-exit into the high-vacuum chamber of Figure 6.3, including simulated particle trajectories from the ALS exit into vacuum; (b) Particle-beam-size evolution (FWHM) of 25 nm PS at an inlet pressure of $p_{in} = 150$ Pa.

In the following subsections, the numerical approaches and models for the drag force mentioned in Chapter 4 are evaluated for different flow conditions by comparing the experimental particle beam evolution in the vacuum chamber with the simulated particle beam profile.

6.3.1 Multiscale regime

For the test cases having variable Knudsen number regimes, the flow field is simulated using the hybrid DSMC/CFD approach described in Section 3.5. To understand, where the transition from continuum to the rarefied regime takes place, Figure 6.5 (a) depicts the distribution of the breakdown Knudsen number Kn_B in the vicinity of the ALS exit for an exemplary case from above. Obviously, for the case of the inlet pressure $p_{in} = 150$ Pa the threshold of $Kn_B = 0.05$ is reached directly at the narrowest point of the outlet. Thus, the entire domain beyond the outlet has to be predicted via DSMC. Figures 6.5 (b) to 6.5 (d) show what happens if the classical CFD solver is used in this region despite the violation of the continuum assumption. The largest deviations between the results predicted by pure CFD and the hybrid DSMC/CFD approach is visible for the temperature and the Mach number. For the hybrid method, large Mach numbers are reached 5 mm behind the ALS exit, whereas the CFD simulation predicts a sub-critical flow with $Ma < 1$. These large deviations in the flow field have to be taken into account when discussing the results of the particle trajectories.

Furthermore, a comparison of the computational costs reveals that the pure DSMC method is nearly 16 times more expensive than the hybrid DSMC/CFD approach, and its flow field exhibits higher statistical noise in low-Knudsen and low-Mach number regions, which necessitates additional simulations for statistical averaging and/or the use of more particles to filter out the noise, thereby further increasing the computational costs.

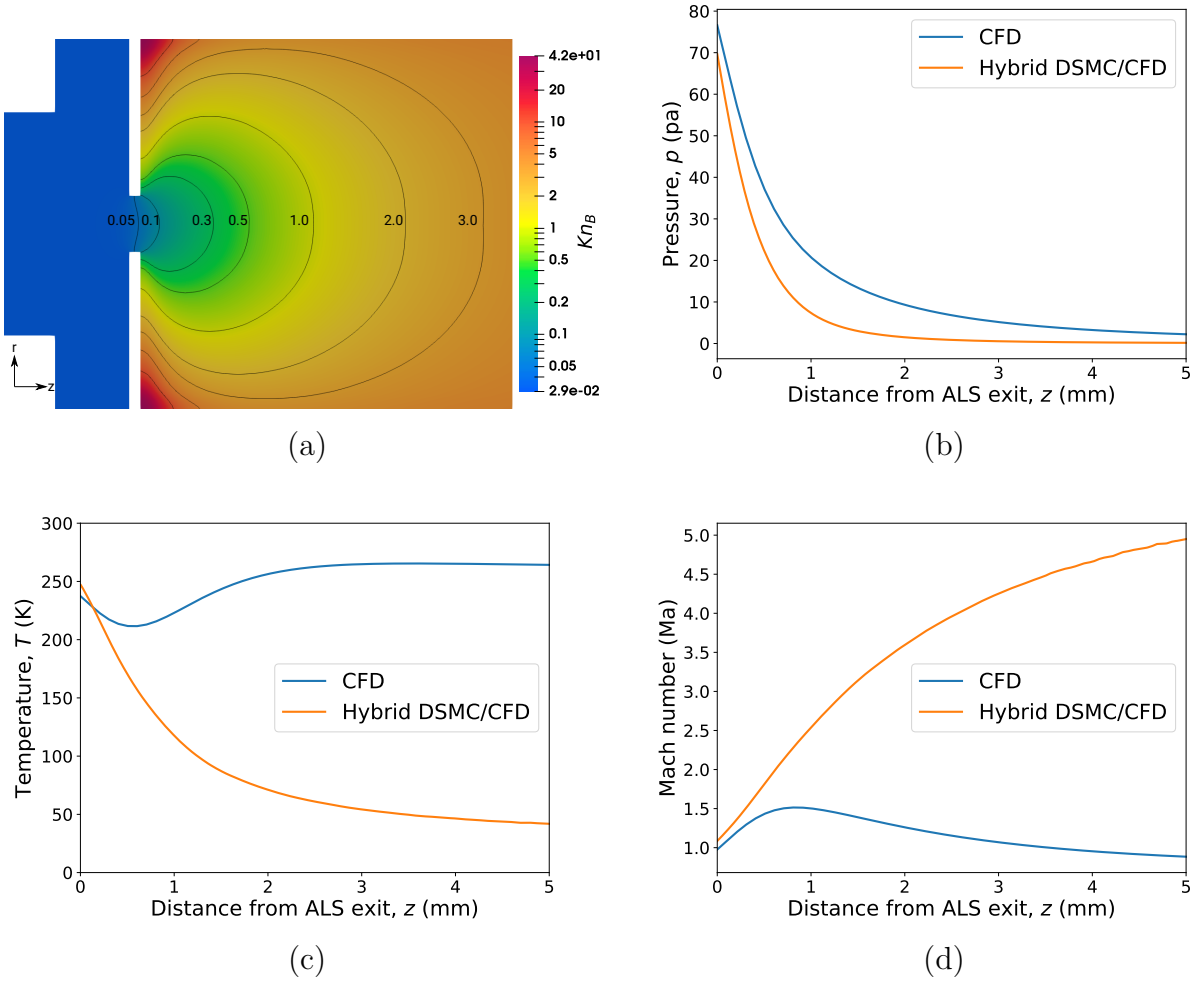

Fig. 6.5. (a) Continuum breakdown in the ALS depicted by the breakdown Knudsen number contour Kn_B for an inlet pressure of p_{in} = 150 Pa; Comparison of the different distributions along the ALS centerline: (b) pressure; (c) temperature; (d) Mach number.

The particle trajectories are subsequently predicted and evaluated like above for 69 nm and 42 nm PS. Since the test cases have very high particle Knudsen numbers (see Table 6.1), the corresponding molecular drag force models are chosen based on the Mach number (Ma) of the flow. For $Ma < 0.3$, the Epstein [46] model (Eqs. (4.9) and (4.10)) is used and for $Ma > 0.3$ the drag model switches to Baines et al. [47] (Eqs. (4.11) and (4.12)). However, it is observed that there are no significant deviations between the results achieved with these molecular drag models and the Stokes-Cunningham model (along with the correction to high Mach number flows [48]) .

Figures 6.6 to 6.8 show the particle beam widths at different positions behind the ALS exit for particle sizes of 69 nm, 42 nm and 25 nm, respectively. The predicted data are given for different inlet pressures shown in Table 6.1. The results predicted by the hybrid

DSMC/CFD method show very good agreement with the experimental data for all particle sizes (i.e., focusing-defocusing behavior and focus position) compared with the pure CFD. This is due to the difference in flow fields predicted in the rarefied domain between the CFD and hybrid methods, as shown in the exemplary Figure 6.5. The particle beam widths computed based on the pure CFD code deviate significantly from the experiment as the inlet pressure reduces.

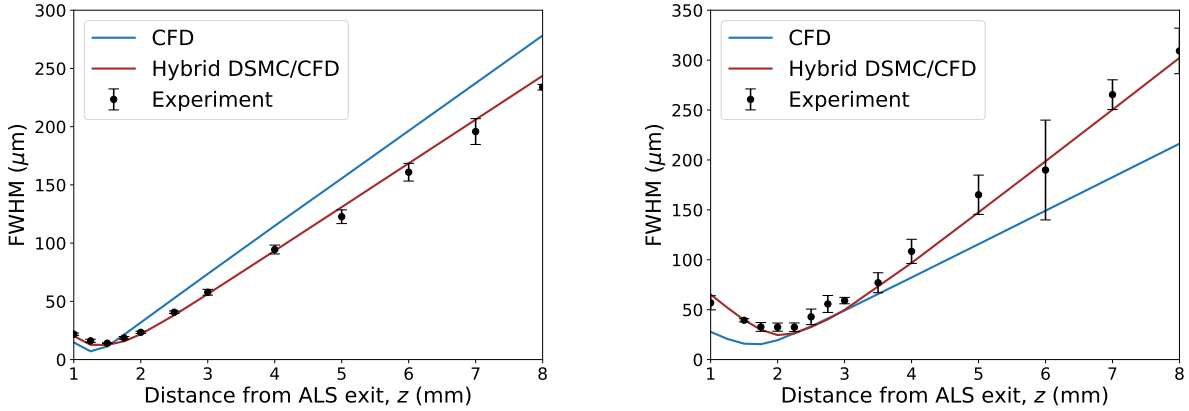

(a) 180 Pa (b) 55 Pa

Fig. 6.6. Particle-beam-size evolution (FWHM) of 69 nm PS at two different inlet pressures.

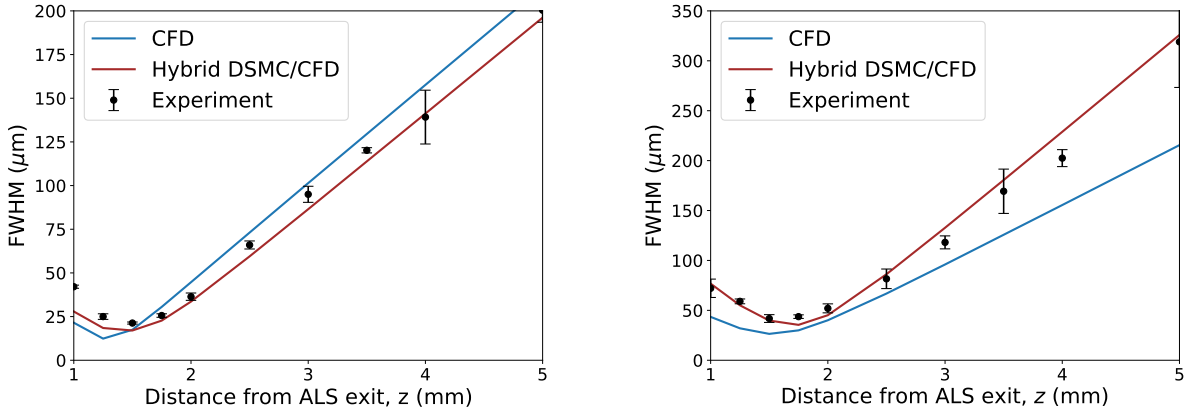

(a) 180 Pa (b) 55 Pa

Fig. 6.7. Particle-beam-size evolution (FWHM) of 42 nm PS at two different inlet pressures.

Accurately estimating the correct focus size and focus position is crucial for quantifying the efficiency of an ALS. Table 6.3 shows the differences in focus size (w_{err}) and focus position (z_{err}) relative to the experimental values for both methods, CFD and hybrid DSMC/CFD. It clearly demonstrates the significant error reduction achieved by incorporating the hybrid approach. Overall, it is evident from Figures 6.6, 6.7, and 6.8 that the

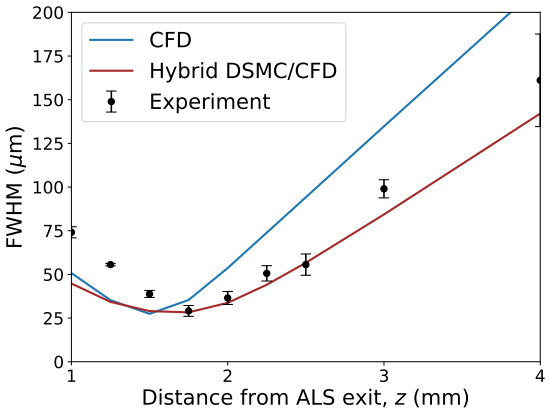

(a) 200 Pa

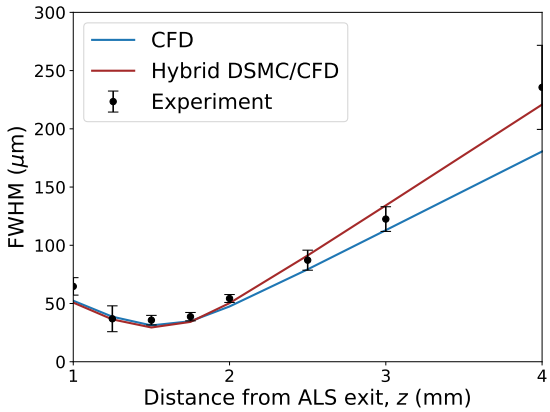

(b) 150 Pa

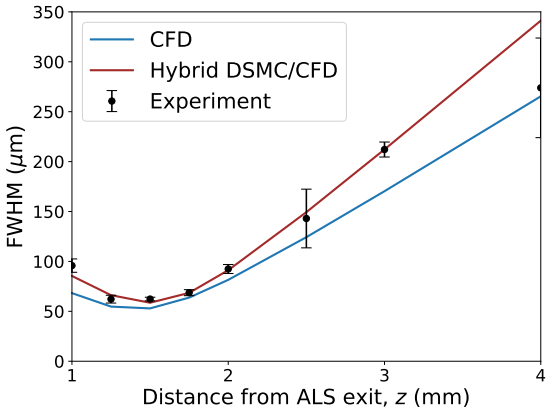

(c) 50 Pa

Fig. 6.8. Particle-beam-size evolution (FWHM) of 25 nm PS at three different inlet pressures.

error associated with the hybrid DSMC/CFD approach falls well within the experimental uncertainty range, further supporting its validity.

Additionally, Appendix B.1 shows a case with 25 nm gold nanoparticles (AuNP) where the hybrid DSMC/CFD methodology could predict the experimental trend quite well, too. Furthermore, the impact of Brownian diffusion on the beam widths is demonstrated. As visible, simulations without the Brownian force model (Eq. (4.20)) show a drastic reduction in beam widths, clearly indicating the necessity of including Brownian diffusion in the model.

6.3.2 Highly rarefied regime

For the test cases with an inlet pressure of $p_{in} = 20$ Pa mentioned in Table 6.1, the maximum global and local Knudsen numbers are evaluated to be greater than 0.1. Therefore, for these test cases it is ideal to use the pure DSMC approach. Nevertheless, Figure 6.9 depicts a direct comparison between the pure CFD results and the DSMC data. The

Particle Size (nm)	p_{in} (Pa)	w_{err} (%)		z_{err} (%)	
		CFD	Hybrid	CFD	Hybrid
69	180	49.57	9.21	16.66	0.0
	55	52.54	12.09	12.50	0.0
42	180	41.84	17.21	16.66	0.0
	55	36.76	14.98	16.66	0.0
25	200	5.73	2.80	14.28	0.0
	150	12.60	6.44	0.0	0.0
	50	11.99	6.41	0.0	0.0
Average		30.1	9.9	11.0	0.0

Tab. 6.3. Differences in focus size (w_{err}) and focus position (z_{err}) relative to the experimental values for various particle sizes and inlet pressures. The values are provided for both CFD and hybrid DSMC/CFD methods.

pressure and Mach number distributions along the ALS centerline and behind its exit are shown. As expected, the deviations are found to be even larger than in the multiscale case discussed above. In the DSMC-predicted flow field, the flow reaches a sonic condition ($Ma = 1$) at the throat/ALS exit (commonly referred to as "choking"), a feature that is not captured by pure CFD in this regime. This circumstance has a significant impact on the evolution of the particle trajectories discussed below.

Once a smooth sampled flow field is established using DSMC, the particle trajectory calculations are carried out for 69 nm and 42 nm PS. Like in the cases described in the previous section, the corresponding molecular drag force models are chosen based on the Mach number of the flow (Eqs. (4.9) / (4.10)) or (Eqs. (4.11) / (4.12)). Furthermore, the relaxed drag force model based on Monte-Carlo sampling (Eq. (4.16)) described in Section 4.2.3 has also been used in place of the Epstein [46] model.

Figures 6.10 (a) and 6.10 (b) show the particle beam widths at different distances from the ALS exit for particle sizes of 69 nm and 42 nm, respectively. In addition to the pure DSMC method, for comparison purposes the underlying flow fields are also simulated using pure CFD.

The results predicted by CFD are not in good agreement with the experimental data for both particle sizes. Here, both the focus position and the width of the particle beam are underpredicted. According to the large deviations observed in the flow fields predicted by pure CFD (see Figure 6.9), this outcome is not astonishing. In the case of DSMC, the particle beam evolution shows a similar trend as the experimental data, where the position of the focus is predicted in reasonable agreement with the measurements. However, the beam widths are underpredicted due to the overestimation of the drag force in this regime. Therefore, the molecular drag is relaxed according to Equations (4.15) and (4.16). Obviously, this corrected drag force yields a much better agreement with the experimental data for both particle sizes, predicting both the beam widths and the focus position quite well.

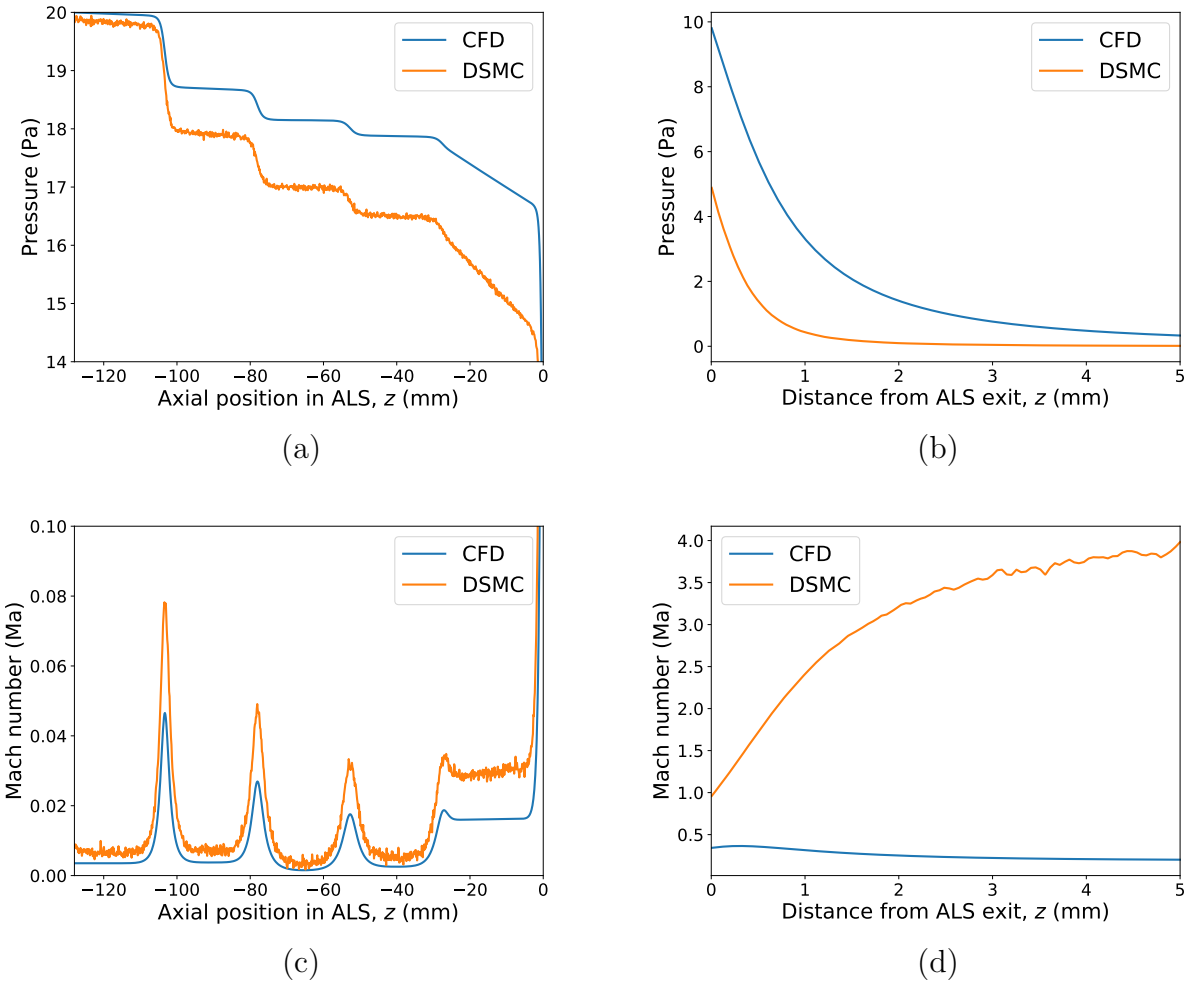

Fig. 6.9. Comparison of different distributions along the ALS centerline for the case of an inlet pressure $p_{in} = 20$ Pa: (a) pressure inside ALS; (b) pressure behind the exit of ALS; (c) Mach number inside ALS; (d) Mach number behind the exit of ALS.

Table 6.4 summarizes the difference in focus size (w_{err}) and in focus position (z_{err}) relative to experimental values for predictions obtained using CFD, DSMC, and DSMC with a relaxed drag model. The table clearly demonstrates that the improved methodology (DSMC with relaxed drag model) substantially reduces the relative errors compared to the other approaches.

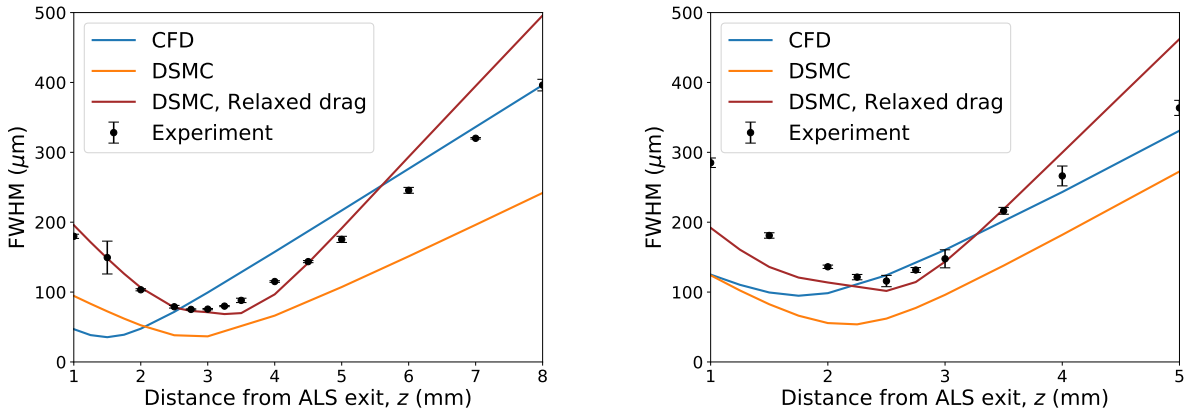

(a) 69 nm (b) 42 nm

Fig. 6.10. Particle-beam-size evolution (FWHM) of PS at an inlet pressure of 20 Pa for two different particle sizes.

Particle	w_{err} (%)			z_{err} (%)		
size (nm)	CFD	DSMC	DSMC relaxed	CFD	DSMC	DSMC relaxed
69	53.14	51.54	2.92	45.45	8.3	4.16
42	18.92	48.88	16.28	40.0	10.0	0
average	36.0	50.2	9.6	42.7	9.1	2.1

Tab. 6.4. Differences in focus size (w_{err}) and focus position (z_{err}) relative to the experimental values for various particle sizes and inlet pressures. The values are provided for both CFD, DSMC and DSMC with relaxed drag model.

6.4 Conclusions

An enhanced and accurate numerical methodology was proposed and implemented for simulating nanoparticle injection through aerodynamic lens systems. The framework captures both the carrier gas flow and the resulting particle trajectories. A hybrid molecular-continuum approach was employed to resolve the gas dynamics across a wide range of Knudsen numbers, ranging from high-density regions within the lens system to the highly rarefied flow during expansion into the vacuum chamber.

Coupling CFD and DSMC allowed for limiting the use of the much more CPU-time intensive molecular model only to those regions, which can not be accurately predicted by the continuum mechanics approach. For the prediction of the particle trajectories, drag force models from the literature were evaluated including molecular drag models. For particles traversing through transitional regimes at the boundary between continuum and molecular flow, an additional correction factor was derived, taking into account the probability that a fraction of the molecules does not collide with a particle in a sub-cell.

The entire methodology was applied to nine different experimental configuration, three particle sizes and three inlet pressures, spanning a wide parameter space. In the multiscale regime, the hybrid DSMC/CFD approach proves to be superior to the pure CFD method. No significant deviations between the results achieved with the molecular drag models and the Stokes-Cunningham model were observed. Quantitatively, the average relative error in the focus size was reduced from 30.1 % with pure CFD to 9.9 % with the hybrid method, while the relative error in the focus position decreased from about 12 to 16 % to nearly 0 %. For the highly rarefied cases, the incorporation of DSMC with the relaxed drag model further decreased the errors, i.e., the average relative error in the focus size was reduced from 36.0 % (using pure CFD) to 9.6 %, and the relative errors in the focus position decreased to 0 or 4.2 %, respectively, thereby achieving excellent agreement with the experimental data [34] – a performance unattainable by classical models. However, this model requires validation against different gas flow conditions, e.g., multi-species gas, and over a wide range of temperatures, 4 to 300 K, and particle sizes, 1 to 25 nm.

7 Aerodynamic Lens Stack injector with cryogenic cooling: Toward efficient focusing of protein-sized nanoparticles[1]

This chapter is concerned with advancing aerosol injection techniques to enable the efficient focusing of protein-sized nanoparticles and macromolecules (< 100 nm) for single-particle imaging (SPI) experiments. Delivering small particles such as individual proteins, remains particularly challenging due to their low inertia and high diffusivity, especially at room temperature [34]. These particles tend to closely follow the carrier gas streamlines and are significantly affected by Brownian motion, which increases beam divergence and results in substantial particle losses. This makes it difficult to generate well-collimated particle beams with high hit rates at the X-ray interaction point for SPI.

A promising strategy to overcome these limitations is to reduce the carrier-gas temperature, thereby diminishing Brownian diffusion and improving particle collimation. The cryogenic buffer-gas beam (CBGB) technology offers a pathway for generating cold, slow, and intense molecular and nanoparticle beams [179, 180]. In this method, inert gases such as helium or neon are cooled to cryogenic temperatures (typically 4-20 K) and passed through a cryogenic buffer-gas cell (BGC), where the temperature of the target particles approaches that of the surrounding gas. This process enables rapid cooling of the suspended particles. For SPI experiments, BGCs have been used to shock-freeze large nanoparticles (> 200 nm) to temperatures below their glass transition (133 K) within microseconds, preserving their structural integrity during injection [35].

Further experimental developments combined the BGC with an Aerodynamic Lens Stack (ALS), forming the BGC-ALS injector system [34]. This hybrid injector has demonstrated the ability to produce dense, focused nanoparticle beams with diameters down to 88 nm. However, the behavior of smaller particles (< 20 nm) in such cryogenic multiscale environments remains poorly understood, primarily due to experimental challenges, particularly the difficulty to optically detect small particles [34].

[1] This chapter is partly based on the publication: S. K. Peravali, A. K. Samanta, M. Amin, P. Neumann, J. Küpper and M. Breuer, "Exploitation of continuum and kinetic theory approaches for the simulation of particle beam experiments", *Proc. 33rd Int. Symp. Rarefied Gas Dyn.*, Springer Nature (2025) [178], and on a manuscript in preparation: S. K. Peravali, L. Worbs, J. He, A. D. Estilore, A. K. Samanta, P. Neumann, M. Breuer and J. Küpper, "Aerodynamic-lens-stack injector with cryogenic cooling: Toward efficient focusing of protein-sized nanoparticles", planned for submission to *Phys. Rev. Fluids*. In both works, I served as the principal contributor, responsible for drafting the manuscripts, visualizing and validating simulation data, developing and applying numerical methodologies, and overall conceptualization.

To overcome these experimental limitations, numerical simulations offer an efficient and informative alternative. Previous studies have explored particle dynamics in buffer-gas environments using a variety of approaches, including random-walk particle tracking [180, 181], continuum CFD [35, 182, 183, 184], DSMC [185, 186, 187], and self-consistent mean-field DSMC (SCMFD) [188, 189] methods. In the present work, a hybrid DSMC/CFD approach coupled with Lagrangian particle tracking, validated in Chapter 6, is employed to model particle behavior in cryogenic injector systems.

This chapter begins by validating the multiscale simulation methodology under cryogenic conditions. Specifically, DSMC simulation parameters – including molecular collision models and gas-surface interaction models – are tested based on a benchmark case of helium flow over a flat plate [190] and compared with experimental data. Following this, the full simulation pipeline is applied to the cryogenic buffer-gas cell, where the injection of 200 nm particles is predicted and validated against experimental results, demonstrating the accuracy of the framework under cold, rarefied conditions. The methodology is then applied to the combined BGC-ALS system, simulating 88 nm particles at two cryogenic temperatures of 4 K and 80 K. These results are again evaluated against experimental measurements to confirm the framework's predictive reliability under multiscale, cryogenic flow conditions. With this validation in place, the simulation framework is further applied to investigate the focusing behavior of smaller particles, specifically 10 nm in diameter, under similar cryogenic conditions – providing deep insights into the design of aerosol injection systems for the efficient delivery of protein-sized nanoparticles in SPI experiments.

7.1 Rarefied cryogenic helium flow over a flat plate

In Chapter 5, the DSMC simulation parameters introduced in Chapter 3 were tested and validated for nitrogen gas at room temperature, and subsequently applied to rarefied ALS flows in Chapter 6. In this section, the applicability of the DSMC simulation parameters is further evaluated under cryogenic conditions by simulating helium flow over a canonical rarefied flow test case, i.e., the flow over a flat plate [190].

At cryogenic temperatures, especially for light gases such as helium, quantum effects can become non-negligible [191]. However, in this study, only classical intermolecular scattering models, i.e., VHS/VSS are employed. This test case is performed specifically to assess the validity and applicability of these classical models in cryogenic regimes, despite the potential limitations arising from neglected quantum effects.

A schematic of the two-dimensional flat-plate flow domain with a size of 50.8×25.4 mm is shown in Figure 7.1, where the flow progresses from the inlet to the outlet along the streamwise direction x, with y denoting the transverse direction. In the corresponding experiment, the flow is produced by a free-jet expansion from a 25.4 mm diameter orifice – establishing the free-stream conditions at the leading edge of the flat plate. These free-stream parameters are summarized in Table 7.1.

Boundary conditions for the various surfaces of the domain are implemented using the available options in SPARTA, as described in Section 3.2. The flat plate is modeled as a solid surface held at a constant temperature of 296 K, with fully diffusive gas-

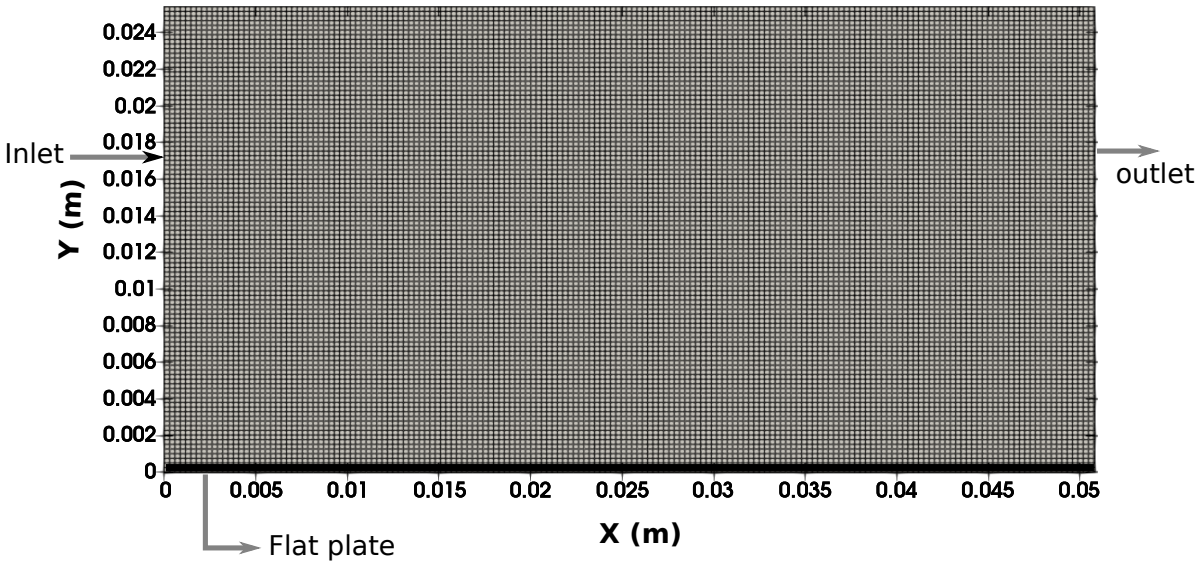

Fig. 7.1. 2D simulation domain of the flat plate test case including the grid.

Stagnation pressure, P_0	1330 Pa
Stagnation temperature, T_0	296 K
Temperature, T_∞	10.7 K
Pressure, P_∞	0.3379 Pa
Velocity, U_∞	1723 m/s
Density, ρ_∞	1.52×10^{-5} kg/m^3
Surface temperature, T_w	296 K
Number density, n_∞	2.21×10^{21} m^{-3}
Mean free path, λ_∞	1.286×10^{-3} m

Tab. 7.1. Flow conditions at the leading edge of the flat plate.

surface interaction. The top boundary of the domain, like the outlet, is treated using an outflow condition. The computational domain is discretized using a uniform grid size of $\Delta x_{cell} = 0.3\ \lambda_\infty$, as illustrated in Figure 7.1 leading to 132×66 number of grid points. Intermolecular collisions in the flow are modeled using the VSS approach, with simulation parameters for helium gas listed in Table 3.1. The Larsen-Borgnakke model with constant relaxation is utilized. For the helium gas the rotational number is set to zero due to its monoatomic nature. Vibration and chemical reactions are assumed to be frozen in the present study and thus not modeled. Furthermore, the CFD simulation was also carried out on the same grid. The settings of this simulation are detailed in Appendix D.

Figure 7.2(a) and (b) present the velocity and temperature contours from the CFD simulation, while Figure 7.3(a) and (b) show the corresponding results from the DSMC simulation. Consistent with the observations in the external shock-dominated cases dis-

cussed in Chapter 5, the DSMC results exhibit a noticeably thicker shock layer over the flat plate compared to the CFD predictions.

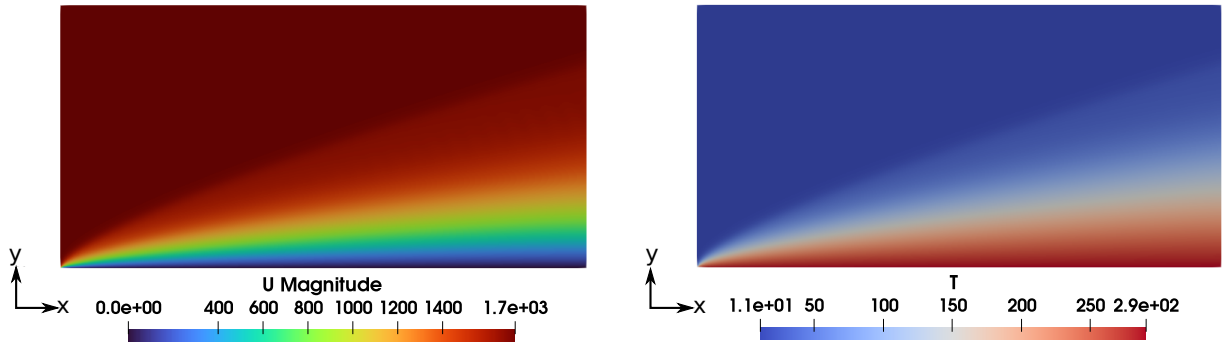

(a) (b)

Fig. 7.2. Results of CFD simulation: (a) Velocities of the flowfield above the flat plate. (b) Temperature of the flow field above the flat plate.

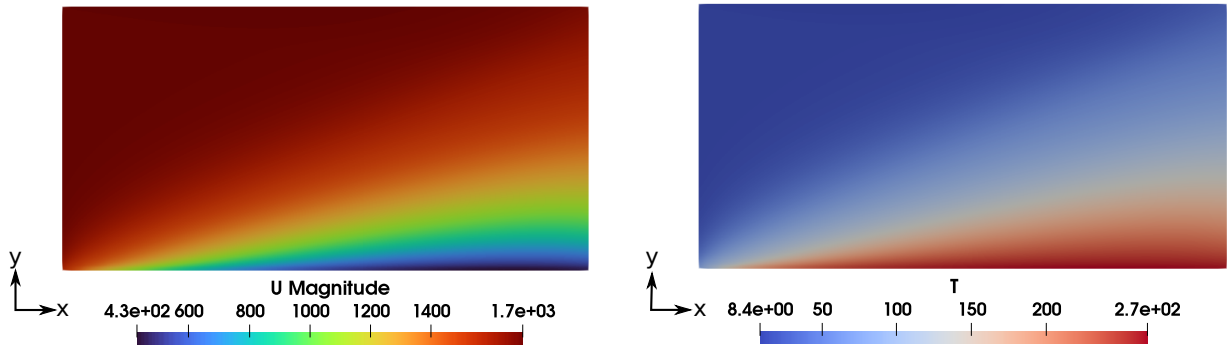

(a) (b)

Fig. 7.3. Results of CFD simulation: (a) Velocities of the flow field above the flat plate. (b) Temperature of the flow field above the flat plate.

Figure 7.4 presents the velocity and temperature profiles as a function of the wall-normal distance at a stream-wise location of $x = 2.5$ mm from the leading edge of the flat plate. The gas properties are normalized by their respective free-stream values, i.e., U_∞ for the velocity and T_∞ for the temperature. Similarly, the wall-normal coordinate y is normalized using the free-stream mean free path λ_∞. The DSMC simulation, employing classical intermolecular collision models, captures the experimental trends in both velocity and temperature profiles [190]. Obviously, a slip velocity appears at the surface. In contrast, the CFD simulation applying a no-slip condition at the surface fails to reproduce the behavior observed experimentally in this rarefied regime. Based on this evaluation, all simulations presented in the following sections are performed using classical intermolecular scattering models, specifically the VSS approach.

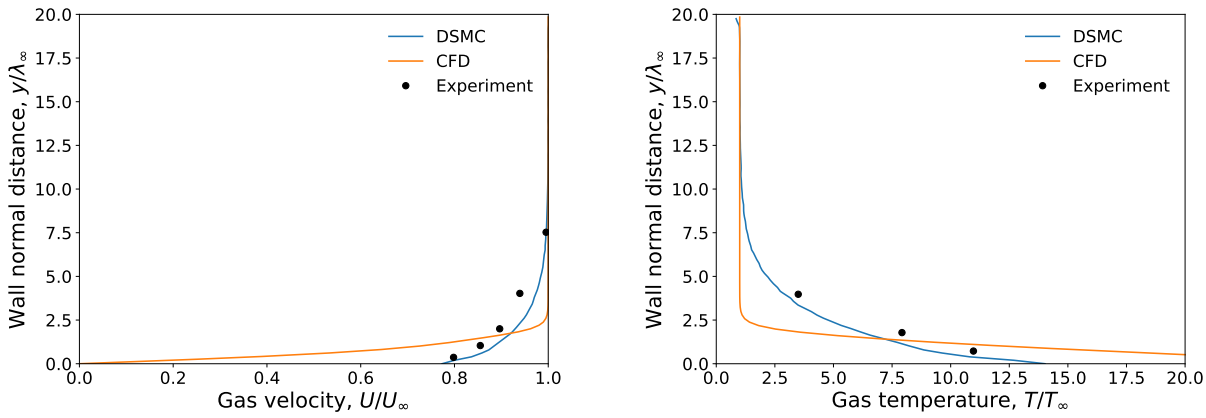

Fig. 7.4. Results of the DSMC simulation (a) Velocities of the flow field above the flat plate. (b) Temperature of the flow field above the flat plate.

7.2 Simulation methodology for buffer-gas injectors

The gas-particle dynamics within various buffer-gas injector configurations are investigated using the multiscale simulation methodology introduced in Chapters 3 and 4 and validated in Chapter 6. The simulation proceeds in two stages. First, the 3D steady-state flow field is computed using the one-way coupled hybrid DSMC/CFD approach described in Section 3.5. For flow regions within the continuum or slip regime ($Kn_B < 0.05$), the compressible Navier-Stokes equations are solved using the `rhoCentralFoam` solver in OpenFOAM, which was evaluated in Chapter 5. The corresponding numerical settings including discretization schemes, interpolation methods, and solver algorithms are described in detail in Chapter 2. These configurations are defined via the `fvSchemes` and `fvSolution` dictionaries in OpenFOAM (see Appendix A). An exemplary 3D simulation domain of the buffer-gas injector with aerodynamic lens stack (BGC-ALS) is illustrated in Figure 7.5. Helium enters the BGC through the designated inlet (colored in dark red) at a specified flow rate and exits via two outlets. Nanoparticles are introduced through a capillary transport tube, which is shown in the figure to indicate the concept but is not included in the simulation domain. The vacuum chambers are modeled as cylindrical domains (colored in purple) extending from both outlet boundaries to capture the pressure drop and flow expansion into high-vacuum conditions. The boundary conditions for the simulation setup are summarized in Table 7.2. In the case of a standalone buffer-gas cell configuration, outlet 2 is retained while the ALS component is removed.

For the CFD simulations, the computational meshes are generated using the `blockMesh` and `snappyHexMesh` utilities available in OpenFOAM. These tools are used to create structured, body-fitted 3D grids for both the standalone BGC and the combined BGC-ALS domains, as illustrated in Appendix D. The standalone BGC mesh consists of approximately 4.7×10^6 cells, while the BGC-ALS configuration results in a mesh with around 6.87×10^6 cells.

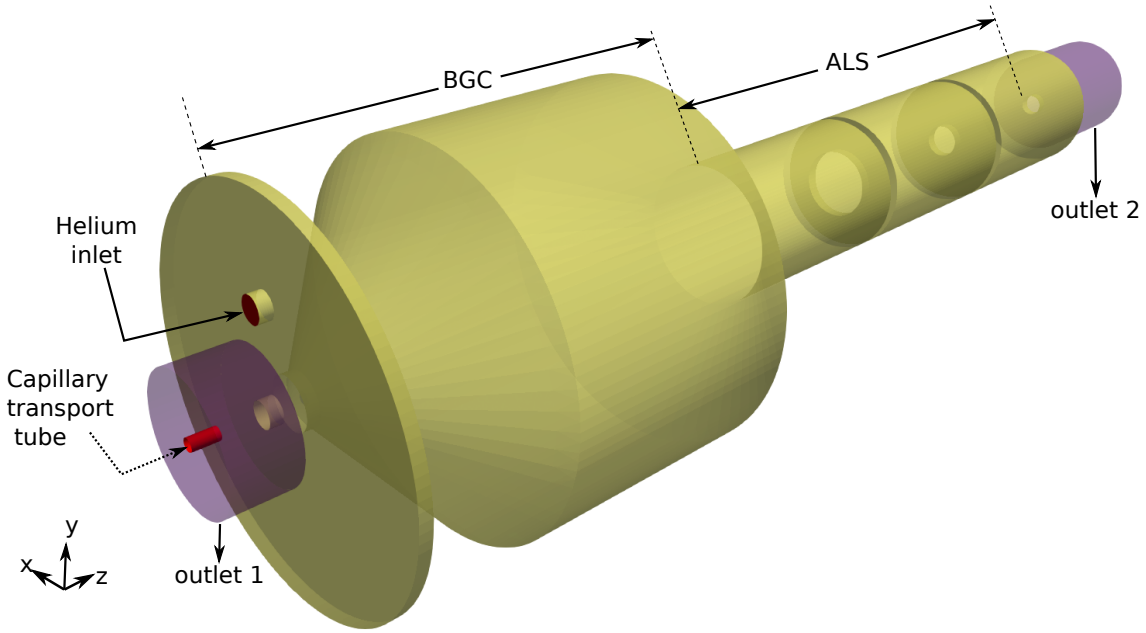

Fig. 7.5. Computational domain of the BGC-ALS injector.

Boundary	U	P	T
Inlet	flowRateInletVelocity	fixed value	fixed value
Outlet 1	zero gradient	wave transmissive	zero gradient
Outlet 2	zero gradient	wave transmissive	zero gradient
Wall	no-slip	zero gradient	fixed value

Tab. 7.2. Boundary conditions for the buffer-gas flow.

The flow is assumed to be laminar due to the low Reynolds number ($Re < 10$), and therefore no turbulence modeling is required. Given the lack of Sutherland coefficients for helium at cryogenic conditions, a constant-transport model (`constTransport`) [60] is employed, where the dynamic viscosity and Prandtl number are held fixed. These values are selected based on helium properties at the corresponding gas temperatures, taken from the NIST technical note [192], with the specific values used in the simulations summarized in Appendix D.

In the rarefied regions ($Kn_B > 0.05$), the DSMC method is applied using the VSS collision model and Larsen-Borgnakke internal energy redistribution, as previously validated in Section 7.1. To ensure sufficient resolution across the entire range of local Knudsen numbers in the rarefied flow domain, a uniform Cartesian grid with cell size $\Delta x = 5 \times 10^{-5}$ m is employed. The simulation time step Δt is determined by the relation $\Delta t = 0.7\ \Delta x/\overline{v}$, where $\overline{v} = \sqrt{8k_BT/(\pi\ m)}$ denotes the mean thermal speed of gas molecules. Gas-surface interactions are modeled using a fully diffusive (isotropic scattering) boundary condition. For statistical convergence in the DSMC simulations, approximately 226 particles per cell

are used. A total of 200,000 time steps are sampled, resulting in an overall sample size of $S = N_c \times N_T = 45.2121 \times 10^6$. The domain is partitioned based on the breakdown Knudsen number Kn_B, as defined in Equation (3.34), ensuring a smooth transition between continuum and kinetic regimes and yielding a contiguous multiscale flow field; an exemplary domain decomposition is illustrated in Figure 3.5. The computed flow data are stored on a uniform Cartesian grid for the use in particle trajectory simulations.

Particle transport is modeled using the CMInject framework described in Chapter 4. Given the dilute nature of the particle phase, only one-way fluid-particle coupling is considered. The drag force acting on the particles is computed using molecular drag models [46, 47], and Brownian motion is incorporated as described in Section 4.2.3.1.

7.3 Cryogenic buffer-gas cell (BGC)

The cryogenic buffer-gas cell (BGC) was designed to rapidly cool nanoparticles, such as biomolecules and proteins, below their glass-temperature at ∼133 K within nano- or microseconds [35]. This shockfreezing process is sufficiently fast to preserve the biomolecules structural integrity. The cooled particles are extracted into a collimated particle stream under high-vacuum conditions. In the injector, cold helium gas, cooled down to 4 K, serves as the carrier gas. In this section, the simulation framework is validated using experimental data for 220 nm polystyrene particles, based on the BGC geometry and flow conditions reported in [35].

Figure 7.6 illustrates the helium flow field within the cryogenic buffer-gas cell (BGC) – simulated using the hybrid DSMC/CFD methodology for a helium inlet flow rate of 25 $\mathrm{ml_n/min}$. The flow is visualized by streamlines, colored according to the Mach-number magnitude. Helium enters the BGC through the inlet located at the top of the thin inlet disk on the left side of the main cell (see Figure 7.5). Particles of 220 nm diameter were injected through a capillary transport tube [35], passed through the BGC starting from outlet 1, and were eventually extracted through outlet 2. For the simulation, particles were introduced at a location 3 mm upstream of outlet 1, with initial velocities specified as $v_r = 6$ m/s in the radial direction and $v_z = 56$ m/s in the axial direction. The spatial distribution at injection follows a Gaussian profile centered at $r = 0$, with a full width at half maximum (FWHM) of 0.5 mm. The initial particle temperature is assumed to be at room temperature. A total of 10,000 particles were simulated using the CMInject framework as described in Section 7.2, enabling accurate prediction of particle dynamics under cryogenic conditions. These initial injection conditions were adopted from previously performed capillary simulations reported by Samanta et al. [35].

Figure 7.7 shows the contour plot of the breakdown Knudsen number Kn_B for the representative BGC–ALS case depicted in Figure 7.6. A threshold of $Kn_B = 0.05$ is used to demarcate regions where the continuum assumption begins to fail. In the vicinity of the injector exits, this threshold is exceeded, indicating the onset of rarefied flow behavior. Based on this assessment, the hybrid framework applies CFD in zones where $Kn_B < 0.05$, while DSMC is activated in regions beyond this limit to resolve molecular-level effects. Although the area upstream of outlet 1 exhibits locally higher Kn_B values, it is still treated

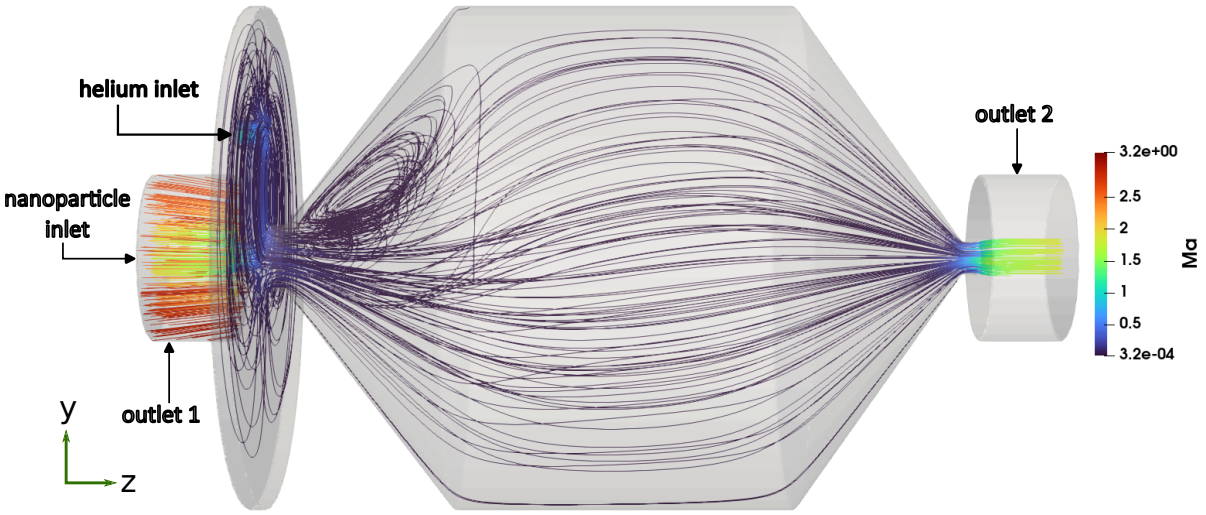

Fig. 7.6. Streamlines of the flow field inside the cryogenic buffer-gas cell, colored by the Mach-number magnitude, as simulated using the hybrid DSMC/CFD method.

using CFD. Validation studies confirm that this treatment does not significantly affect the accuracy of downstream particle transport, thereby allowing for a more computationally efficient domain decomposition without sacrificing solution fidelity.

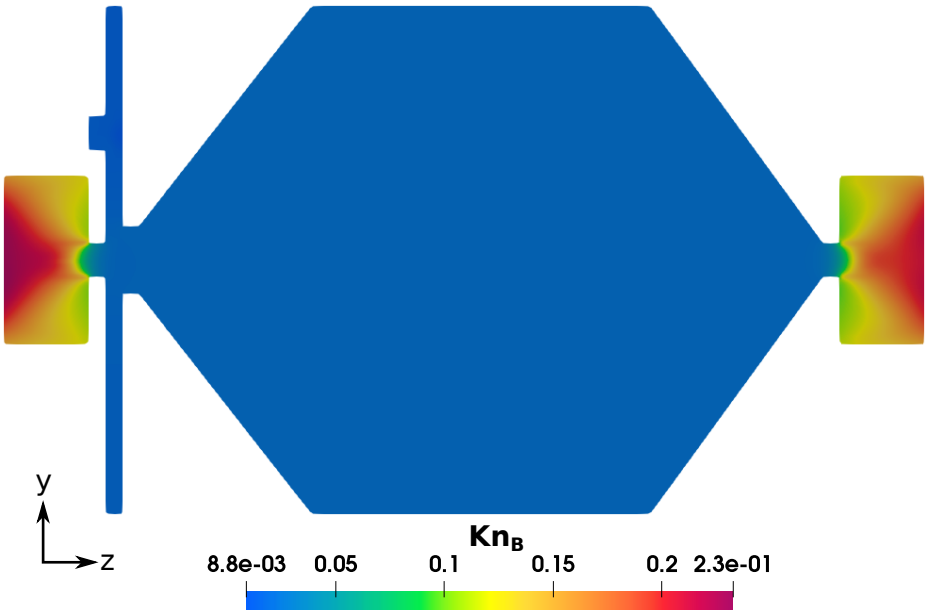

Fig. 7.7. Continuum breakdown in the BGC depicted by the breakdown Knudsen number contour Kn_B for an inlet flow rate of 25 $\mathrm{ml_n/min}$.

Figure 7.8 shows the particle beam widths (FWHM) of 220 nm polystyrene particles measured 10 mm downstream of outlet 2 as a function of the helium flow rate, capturing the effects of varying pressures and velocities. The simulations are conducted at a helium flow temperature of 4 K. The simulation results align well with experimental data [35], accurately reproducing the observed trends.

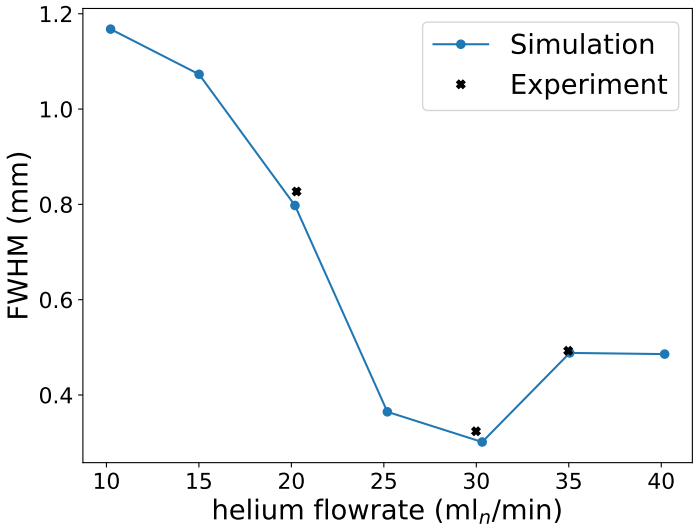

Fig. 7.8. Predicted particle beam widths (blue spheres) for 220 nm-diameter polystyrene spheres as a function of the helium flow rate, compared to experimental data (black crosses) [35].

7.4 ALS with cryogenic cooling (BGC-ALS)

Building on the previous investigations of cryogenic buffer-gas cell (BGC) injectors and room-temperature aerodynamic lens systems, experimental advancements have demonstrated that combining these approaches, i.e., integrating an aerodynamic lens stack (ALS) with a cryogenic BGC – can significantly improve the focusing of smaller particles (diameters < 100 nm) [34]. This hybrid injector configuration enhances nanoparticle delivery by leveraging the reduced carrier-gas temperature to suppress thermal diffusion and improve beam collimation.

Figure 7.9 depicts the helium flow field within the BGC-ALS system, simulated using the hybrid DSMC/CFD methodology at a helium inlet flow rate of 15 $\mathrm{ml_n/min}$ and a temperature of 4 K. The details of the simulation methodology applied are provided in Section 7.2. The flow field is represented by streamlines, with colors indicating the Mach-number magnitude. Helium enters the system through the inlet on the upper side of the thin inlet disk at the left of the main cell. Particles of 88 nm diameter were introduced through outlet 1 via a capillary transport tube [34], traversed the BGC-ALS system, and were subsequently extracted through outlet 2. For the simulation, particles were injected

at a position 3 mm upstream of outlet 1 with an initial axial velocity of $v_z = 31$ m/s and no radial velocity component. The spatial distribution of the injected particles followed a Gaussian profile centered at $r = 0$ with a full width at half maximum (FWHM) of 0.5 mm. The initial particle temperature is assumed to be at room temperature. A total of 10,000 particles were tracked using the CMInject framework, as described in Section 7.2. These initial injection parameters were adopted from capillary injection simulations previously reported in [34], ensuring a realistic representation of particle entry conditions.

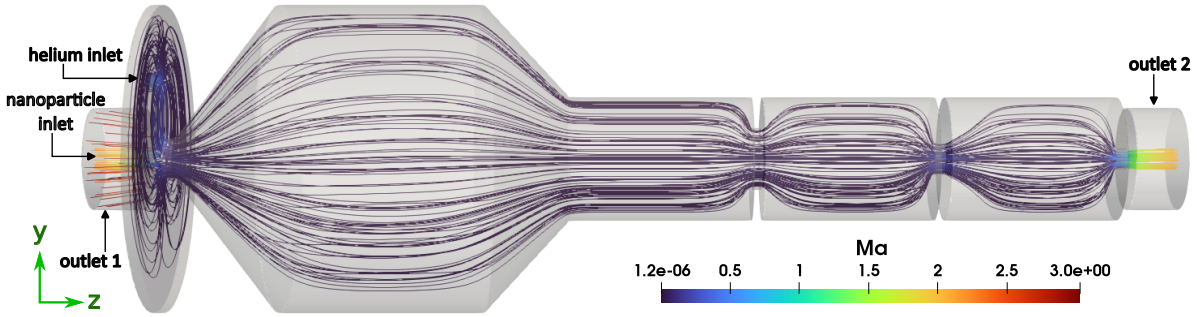

Fig. 7.9. Streamlines of the flow field through the combined setup of BGC and ALS, colored by the Mach-number magnitude, as simulated using the hybrid DSMC/CFD method for an inlet flow rate of 15 $\mathrm{ml_n/min}$.

Figure 7.10 illustrates the contour of the breakdown Knudsen number Kn_B for the exemplary case shown in Figure 7.9. The threshold value of $Kn_B = 0.05$, used to delineate the transition from continuum to rarefied flow, is reached in the region surrounding the injector exits. Accordingly, the hybrid simulation framework employs CFD in regions where $Kn_B < 0.05$ and uses DSMC where $Kn_B > 0.05$ to ensure accurate resolution of rarefied gas effects. Although the region upstream of outlet 1 exceeds the Kn_B threshold, it is still modeled using pure CFD. Numerical tests confirm that this approximation has negligible influence on the downstream particle beam evolution, thus justifying the use of CFD for improved computational efficiency in that portion of the domain.

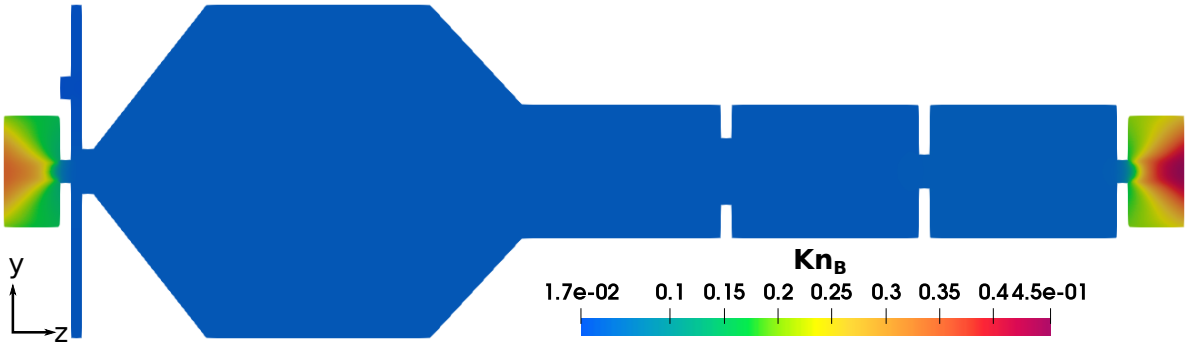

Fig. 7.10. Continuum breakdown in the BGC-ALS depicted by the breakdown Knudsen number contour Kn_B for an inlet flow rate of 15 $\mathrm{ml_n/min}$.

Figure 7.11 (a) presents the evolution of the particle beam widths (FWHM) at various distances downstream of the BGC-ALS exit (final lens) for helium flow rates of 10 ml_n/min and 15 ml_n/min. The beam widths are compared with experimental measurements taken 6 mm, 8 mm, and 10 mm downstream of the exit [34]. The simulation results show very good agreement with the experimental data, accurately capturing the particle beam focusing behavior.

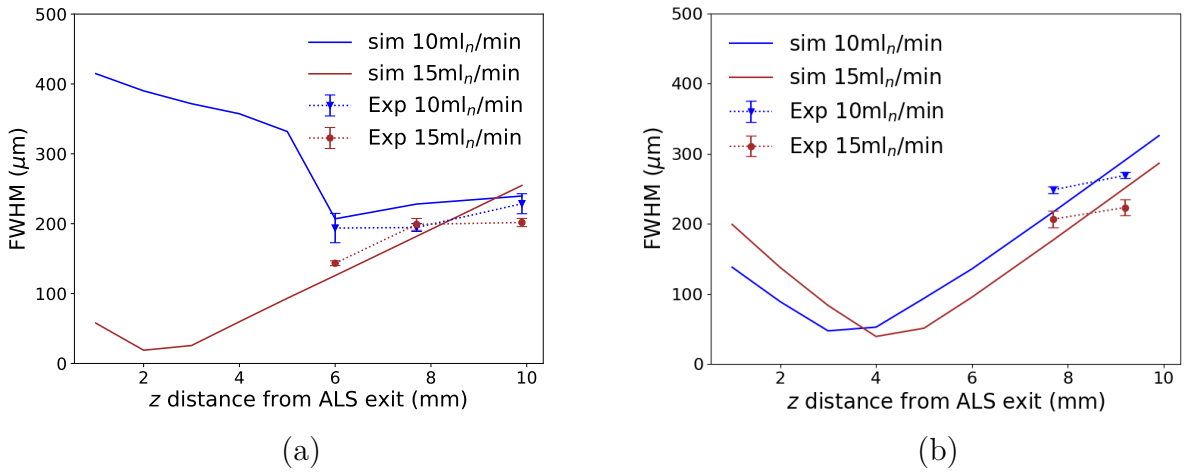

Fig. 7.11. Simulated evolution of the particle beam size (FWHM) for 88 nm-diameter polystyrene spheres at different flow rates of helium, compared to experimental data [34]: (a) at 4 K, (b) at 80 K.

Figure 7.11 (b) shows the corresponding simulation results for a higher helium temperature of 80 K at the same flow rates of 10 and 15 ml_n/min. The particle beam widths are compared with experimental measurements taken 8 mm and 10 mm downstream of the BGC-ALS exit. The simulated trends align well with the experimental data, demonstrating the predictive capability of the simulation framework across a wide temperature range.

7.5 Toward focusing of protein-sized particles

Experimental characterization of nanoparticle beams becomes increasingly challenging as the particle size decreases. For particles smaller than 20 nm, particularly around 10 nm, conventional optical detection techniques face significant limitations due to weak scattering signals [34]. As a result, the focusing behavior of such small particles in cryogenic, multiscale flow environments remains poorly characterized. In this section, the dynamics of 10 nm particles are investigated using numerical simulations based on a framework that has been previously validated for larger particle sizes under comparable cryogenic conditions.

7.5.1 Comparison of BGC and BGC-ALS injector performance for 88 nm and 10 nm nanoparticles

To evaluate the influence of aerodynamic lens stack (ALS) integration on the focusing performance of small nanoparticles, simulation results are compared for two injector configurations: the standalone cryogenic buffer-gas cell (BGC) and the combined BGC-ALS setup. As discussed earlier, significant experimental progress has been achieved in focusing particles smaller than 100 nm using the BGC-ALS configuration [34], which also served previously as a benchmark for validating the simulation framework. In this analysis, the carrier gas flow field computed from earlier simulations at a helium flow rate of 15 ml_n/min is reused to simulate the particle trajectories.

Figure 7.12 (a) compares the evolution of the particle beam width (FWHM) of 88 nm particles at various distances downstream of the injector exit. The results show that adding the ALS to the BGC shifts the focus position farther downstream – from approximately 1 mm in the standalone BGC case to around 2 mm in the BGC-ALS configuration. Beyond this focal point, the BGC-ALS setup maintains narrower beam widths over an extended range, demonstrating improved collimation even during the defocusing phase.

The comparison is then extended to smaller 10 m particles. Figure 7.12 (b) presents the evolution of the particle beam width (FWHM) at various distances downstream of the injector exit, again for a helium flow rate of 15 ml_n/min. For these smaller particles, the BGC-ALS configuration achieves a beam focus around 1 mm closer to the injector exit – compared to the BGC-only setup. Notably, the BGC-ALS setup also yields a narrower beam width at its focus position. However, in the region between 2 mm and 4 mm downstream of the exit, the BGC-ALS beam is slightly broader than that of the BGC. Beyond 5 mm, the BGC-ALS configuration results in consistently narrower beam profiles, particularly at 6 mm, 8 mm, and 10 mm – locations typically used for experimental detection. This indicates that while ALS integration results in narrower beams at downstream positions, further design optimization of the ALS geometry or operating parameters are necessary to effectively collimate such small particles for SPI applications.

7.5.2 Focusing 10 nm particles at different temperatures

To assess the influence of the carrier-gas temperature on nanoparticle focusing, this section investigates the performance of the BGC-ALS configuration at three representative thermal conditions: 4 K, 80 K, and room temperature. Since Brownian motion and gas viscosity are strongly temperature-dependent, varying the gas temperature directly impacts the focusing and diffusive spreading of the particle beam. The simulations are performed using the identical flow rate of 15 ml_n/min and geometry across all cases to evaluate the injector's robustness and efficiency over a broad temperature range.

Figure 7.13 (a) presents the evolution of particle beam widths (FWHM) at various distances downstream of the BGC-ALS exit. A clear trend emerges: lower gas temperatures result in significantly narrower particle beams, highlighting the effectiveness of cryogenic operation in suppressing thermal diffusion and improving beam collimation.

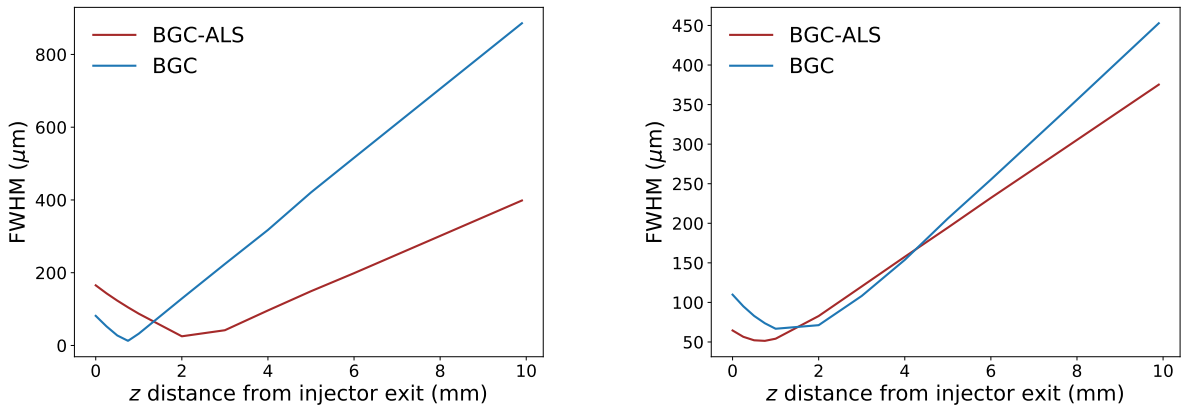

Fig. 7.12. Comparison of particle beam size evolution (FWHM) between BGC and BGC-ALS setups with an inlet helium flowrate of 15 ml_n/min (a) for 88 nm polystyrene spheres. (b) for 10 nm polystyrene spheres.

However, in the BGC-ALS configuration, this improvement cannot be attributed solely to the reduction in Brownian motion. Temperature-induced changes in gas viscosity also modify the flow regime. Despite the same inlet flow rate, each case exhibits different flow characteristics. For the 4 K case, the number density before the aerodynamic lens section is 3.54×10^{22} m^{-3}, with a corresponding Knudsen number of 0.0334. At 80 K, the number density is 1.55×10^{22} m^{-3} and $Kn = 0.132$, while at room temperature it is 8.58×10^{21} m^{-3} with $Kn = 0.27$. Therefore, to achieve a flow regime comparable to that of the low-temperature condition particularly with respect to the Knudsen number, a higher inlet flow rate is required at elevated temperatures to maintain an equivalent number density of the gas.

To isolate the effect of Brownian motion resulting from temperature variations, it is essential to study the particle beam evolution under consistent flow regimes, i.e., at identical gas number densities. Achieving this by adjusting the inlet flow rate to maintain the same Knudsen number across different temperatures requires an iterative and computationally intensive process. To simplify the analysis while preserving control over the Knudsen regime, additional simulations were conducted for the ALS component alone from the BGC-ALS injector, using a fixed inlet number density $n_{in} = 1 \times 10^{22}$ m^{-3} for all three temperatures (4 K, 80 K, and room temperature). Particles were introduced at the ALS inlet following a Gaussian spatial distribution with an initial beam width of 4×10^{-3} m and no initial velocity. The initial particle temperature is assumed to be equal to the corresponding gas temperature.

Figure 7.14 shows the flow fields at different temperatures and the corresponding trajectories of 10 nm nanoparticles through the ALS. Here, r represents the radial and z the axial coordinate of the flow domain. The effect of Brownian diffusion becomes apparent when comparing particle trajectories at various temperatures. At room temperature, increased diffusion causes poor focusing, with some particles failing to traverse the ALS

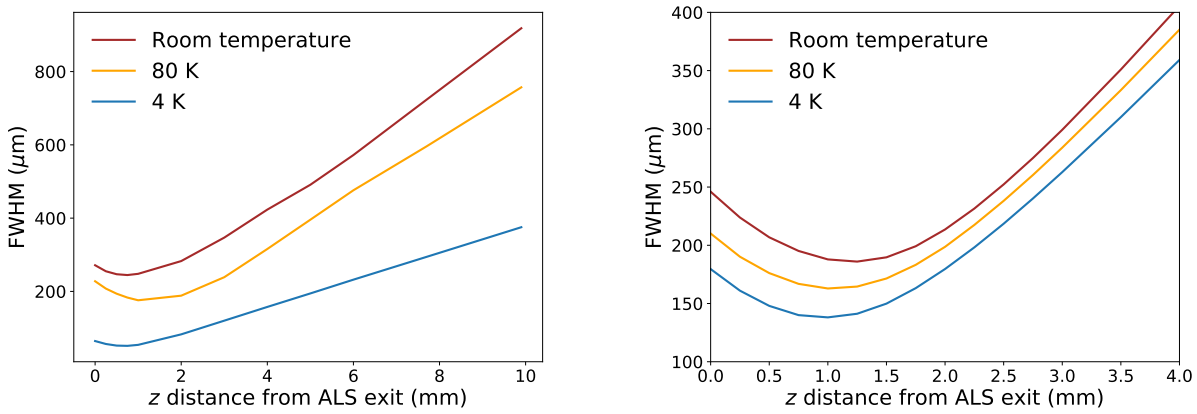

Fig. 7.13. Simulated evolution of particle beam widths (FWHM) for 10 nm diameter polystyrene particles at different helium flow temperatures: (a) through the BGC-ALS configuration with a constant inlet flow rate of 15 ml_n/min; (b) through the ALS component alone with a fixed inlet number density of 1×10^{22} m^{-3}.

completely. As the temperature decreases, Brownian motion is suppressed, resulting in improved confinement and more effective transmission of particles through the lens system. Reducing the gas temperature thus not only enhances beam collimation but also significantly improves particle transmission efficiency.

Figure 7.13 (b) presents the evolution of the particle beam width (FWHM) along the downstream distances of the ALS exit. The results confirm that lower gas temperatures yield narrower particle beams, even when the flow regime is held constant. These findings demonstrate the extent to which beam collimation can be improved purely through temperature control, independent of flow regime variations.

7.6 Conclusions

This chapter presented a detailed numerical investigation on the performance of cryogenic buffer-gas injectors, focusing on their ability to efficiently deliver protein-sized nanoparticles for single-particle imaging (SPI) applications. The multiscale simulation framework, comprising a hybrid DSMC/CFD methodology for gas dynamics and the Lagrangian CMInject tool for particle tracking, was employed to model gas-particle interactions under highly rarefied, cryogenic conditions. The approach builds upon the framework validated earlier for room-temperature ALS injectors and extends its application to helium flows at low temperatures.

The simulation methodology was first benchmarked using a canonical rarefied flat-plate flow problem at cryogenic temperatures to evaluate the applicability of classical intermolecular collision models (VSS with Larsen-Borgnakke) under conditions where quantum effects may become relevant. Notably, the classical scattering models were found

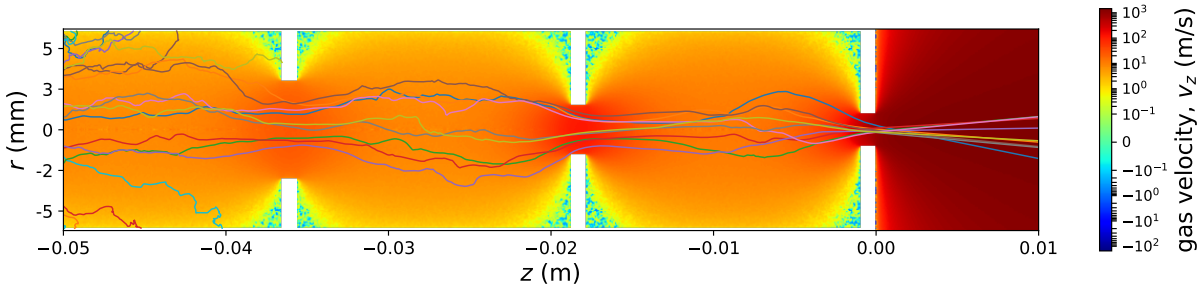

(a) Room temperature

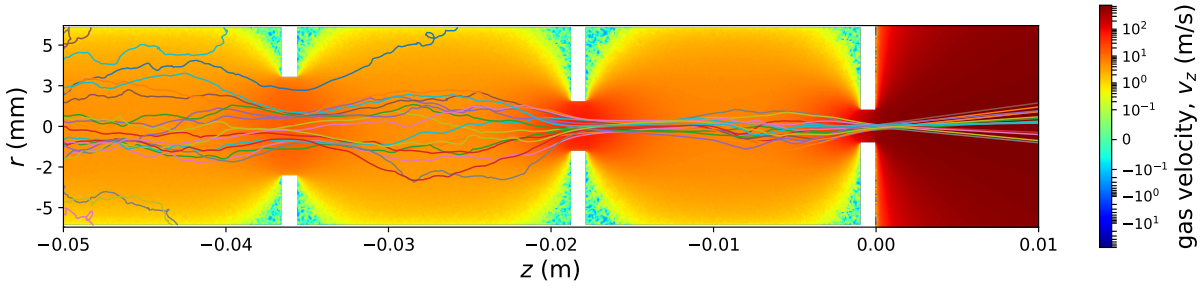

(b) 80 K

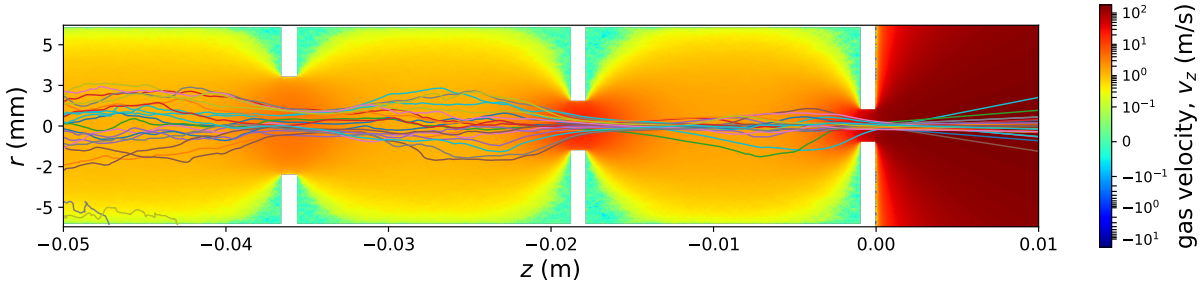

(c) 4 K

Fig. 7.14. Simulated trajectories (colored lines) of the 10 nm PS through the aerodynamic-lens stack drawn on top of the gas-flow field ($n_{in} = 1 \times 10^{22}$ m^{-3}) visualized by the axial velocity in a logarithmic color scale.

to adequately capture experimental trends, even in regimes where quantum phenomena could potentially influence the flow behavior. The validated framework was then applied to simulate two key injector configurations: the standalone cryogenic buffer-gas cell (BGC) and the combined BGC-Aerodynamic Lens Stack (BGC-ALS) system. For the BGC configuration, helium flow at 4 K was modeled and combined with particle tracking of 220 nm polystyrene spheres, while the BGC-ALS configuration was validated using 88 nm polystyrene particles at both 4 K and 80 K. In both cases, the simulations showed good agreement with experimental measurements, demonstrating the predictive accuracy and

robustness of the multiscale simulation pipeline across a wide range of cryogenic operating conditions.

Beyond validation, the study explored the behavior of smaller 10 nm particles, representative of proteins, highlighting the challenges associated with focusing such low-inertia particles due to strong Brownian motion and low drag. Comparative simulations showed that while the BGC-ALS configuration offers superior beam collimation over the BGC-only design for 88 nm particles, its performance for 10 nm particles is more limited, with broader beam widths and less pronounced focusing. These findings underscore the need for further injector optimization, especially in lens design, flow rate tuning, and geometric configuration, when targeting particles smaller than 20 nm.

Furthermore, the effect of carrier-gas temperature on focusing was systematically examined. Results confirmed that lower temperatures lead to narrower particle beams due to reduced thermal diffusion and changes in flow viscosity. However, it was also shown that to fairly isolate the impact of Brownian motion, simulations at different temperatures must maintain constant number densities of the gas flow, which in turn requires different inlet flow rates due to varying gas properties.

In summary, this chapter establishes the applicability and limitations of the current hybrid simulation methodology for cryogenic injection systems and provides physical insight into the design and operation of injectors optimized for nanoparticles smaller than 100 nm. These results lay the groundwork for future studies aimed at tailoring ALS geometries and buffer-gas cell parameters to meet the stringent requirements of SPI experiments targeting smaller macromolecules and proteins.

8 Conclusions and outlook

This thesis established a comprehensive simulation methodology for the predictive modeling and optimization of nanoparticle injection systems, with a particular focus on aerodynamic lens stacks (ALS) as used in single-particle diffractive imaging (SPI). By addressing the multiscale nature of gas flows within and beyond these injectors – ranging from continuum to free molecular regimes – this work overcomes the constraints of traditional single-regime solvers, providing a validated computational framework suitable for both theoretical investigations and experimental injector design.

A key foundation of this research was the detailed evaluation of classical computational fluid dynamics (CFD) methods based on the continuum assumption and direct simulation Monte Carlo (DSMC) methods for simulating low-density gas flows where the continuum assumption breaks down. Canonical test cases, including internal nozzle flows and external conical body flows were used to assess the accuracy and applicability of each solver. In the CFD evaluation, both pressure-based and density-based approaches were first validated on the internal nozzle expansion case, with the density-based solver `rhoCentralFoam` demonstrating superior performance in capturing steep gradients and compressibility effects, making it more suitable for high-speed flows. For internal flows, DSMC outperformed CFD in resolving rarefaction-induced effects such as viscous dissipation from flow thermalization dominated by molecule-surface collisions and non-equilibrium phenomena like rotational freezing, where rotational and translational temperatures decouple due to rapid expansion. For external hypersonic flows, the Knudsen number near the surface decreases due to shock-induced compression, placing the region closer to the continuum regime; both CFD and DSMC showed good agreement near the surface, although DSMC predicted a consistently thicker shock layer due to its ability to capture non-equilibrium effects. These studies established the operational limits and complementary strengths of each method in flow regimes and geometries relevant to aerosol injector applications.

To overcome the limitations of both single methods, a hybrid DSMC/CFD framework was constructed. This one-way coupling approach uses the CFD simulation to provide boundary conditions for the DSMC prediction, while backward coupling is not considered. This is justified for gas flows in aerosol injectors used in SPI experiments, where rarefaction arises mainly from gas expansion and the impact of the rarefied region on the upstream flow is minimal, allowing for improved computational efficiency without compromising accuracy. The coupled procedure was validated against experimental data and has shown to offer a highly efficient and accurate solution across multi-regime flows. The domain decomposition into CFD and DSMC regions was guided by an established continuum breakdown criterion based on local and global Knudsen numbers. While such criteria have been used in earlier studies, their consistent and practical implementation in the context of nanoparticle injector geometries demonstrated the framework's adaptability.

A comprehensive sensitivity analysis of the DSMC method was conducted on the canonical test cases to understand the influence of key numerical parameters on the accuracy achieved. These included the number of simulation particles per cell, the grid resolution, and the time step size, all of which were shown to impact statistical convergence and computational costs. The effect of gas-surface interaction models and molecular collision models (e.g., VHS vs. VSS, constant vs. variable relaxation) was systematically assessed, revealing their significance in predicting near-wall behavior and thermodynamic properties. In addition, statistical error analyses – based on root-mean-square deviation metrics – were performed to quantify the noise inherent in DSMC simulations and to establish optimal sampling strategies. This parameter space exploration not only provided best-practice guidelines for the DSMC solver configuration but also enhanced the robustness and reliability of the hybrid methodology. The selective application of molecular simulations only in regions, where it is necessary to maintain accuracy, significantly reduced computational costs without compromising predictive fidelity.

Furthermore, performance studies involving both strong and weak scaling were conducted to evaluate the computational speed-up and energy consumption of DSMC simulations. These investigations confirmed that SPARTA's dynamic load balancing feature delivered the most efficient parallel performance. Overall, this study helped to identify an optimal parameter and solver setup that ensures hybrid DSMC/CFD simulations to remain both accurate and computationally efficient.

The hybrid framework was then applied to simulate particle transport through ALS injectors under varying pressure and particle-size conditions. The study introduced physics-based drag models, including the Epstein [46] and Baines [47] formulations, and accounted for Brownian motion effects [170] to accurately resolve nanoparticle dynamics. For highly rarefied flow conditions, where standard drag models overestimate momentum transfer, a novel relaxation model was developed [74]. This model, inspired by DSMC sampling techniques, corrected the drag force based on probabilistic molecular collision filtering within a sub-cell volume. The resulting predictions for nanoparticle beam width and focus position exhibited excellent agreement with experimental observations for different particle sizes.

Comparative analyses between the hybrid framework (DSMC/CFD + particle transport) and a conventional pure CFD-based approach (CFD + particle transport) revealed that the hybrid methodology consistently outperformed the pure CFD method under the given experimental conditions, specifically for ALS systems operating at low inlet pressures. The hybrid simulations more accurately predicted both the nanoparticle beam width and focus position, with deviations falling well within the experimental uncertainty range, thereby demonstrating its superior predictive fidelity across a wide range of flow regimes and particle sizes relevant to SPI applications.

Finally, the methodology was utilized to simulate the performance of an ALS combined with cryogenic buffer-gas cooling (BGC), a configuration proposed for enhancing the focusing of smaller particles ($d_p < 100$ nm). The hybrid methodology – adapted to simulate buffer-gas environments, was first validated against available experimental data for standalone BGC and BGC-ALS injector configurations. Upon confirming its predictive capability under these cryogenic conditions, the framework was applied to investigate

the focusing performance of protein-sized nanoparticles ($\approx$ 10 nm). The hybrid simulations demonstrated that lowering the carrier gas temperature substantially improved the beam quality and focusing sharpness, especially for particles in the protein-size regime. This improvement is primarily attributed to the reduction in thermal velocity at lower temperatures, which suppresses Brownian diffusion. These findings reinforce the potential of cryogenic ALS-BGC systems for pushing the lower size limit of SPI-compatible nanoparticles.

Overall, the thesis demonstrated that the hybrid DSMC/CFD framework, when combined with appropriate drag models and detailed numerical calibration, provides a powerful tool for the accurate and efficient simulation of nanoparticle injection systems. The validated predictions not only reproduce experimental trends across a wide range of conditions but also enable systematic injector optimization for future SPI applications.

8.1 Outlook

Future work can proceed along multiple directions to further advance the simulation framework developed in this thesis and address its current limitations. Despite the promising results demonstrated in this thesis, the hybrid simulation methodology also possesses certain limitations and requires future refinement.

As the current DSMC/CFD methodology was utilized to simulate low-temperature or cryogenic gas flows, which is particularly relevant for buffer-gas cooling (BGC) systems, quantum effects in intermolecular collisions may become significant [191]. Conventional DSMC relies on classical collision models, which may not fully capture the transport phenomena at very low temperatures where ab-initio potentials and quantum scattering theory become more appropriate. For such regimes, advanced modeling approaches based on quantum kinetic theory or validated empirical corrections taking these effects into account may need to be incorporated to ensure accuracy.

Another limitation is the current use of a one-way coupled hybrid DSMC/CFD approach. While effective in many cases, this method does not capture feedback effects that may arise in regions of strong gas-particle interaction or flow instabilities, such as vortex shedding near the continuum breakdown interface. In these cases, a two-way coupled DSMC/CFD framework, where information is exchanged iteratively between the continuum and molecular solvers – could improve the fidelity of flow predictions, although at increased computational expense.

Looking ahead, future work will focus on improving and extending the drag force models used in transitional and free-molecular regimes. In particular, experimental and numerical studies are planned to better characterize the relaxed drag model introduced in this work, especially under highly rarefied BGC/BGC-ALS conditions. The aim is to refine the stochastic collision-filtering methodology and calibrate it against new measurements across a broader range of flow velocities, particle sizes, and temperatures.

Efforts will also be directed toward advancing heat transfer models in nanoparticle-laden rarefied flows. Current approaches remain simplistic in describing the thermodynamic evolution of particles during injection [170]. More sophisticated models that capture

energy exchange dynamics – including accommodation coefficients and inelastic collisions – are needed to support future experiments involving thermally sensitive biomolecules or nanoparticles.

One key challenge lies in accurately resolving low-Mach number transitional flows within the DSMC regime. Under such conditions, macroscopic quantities like pressure, temperature, and velocity are particularly susceptible to statistical noise, which can lead to inaccuracies in the simulation results. This issue is amplified when simulating unsteady or slowly evolving flows, where a large number of time steps and particle samples are required to achieve statistically converged solutions, substantially increasing the computational cost. These challenges are further intensified in three-dimensional simulations, where the increased dimensionality leads to a significant rise in the particle count, placing heavy demands on memory, processing time, and data storage. As a result, achieving convergence in 3D DSMC simulations under low-Mach number, transitional conditions remains a particularly demanding task.

A potential direction for mitigating these limitations lies in the integration of discrete velocity methods (DVM) as an alternative to DSMC for low-speed flows. Unlike DSMC, which relies on statistical sampling of particle interactions, DVM directly solves the Boltzmann equation on a discretized velocity space, avoiding stochastic noise and offering inherently smoother solutions in rarefied flow regimes. Future work could focus on developing improved DVM schemes capable of accurately capturing both low-speed and high-speed flow features. The validity of such solvers could be established through systematic comparisons with DSMC results across a range of benchmark cases. Upon validation, the refined DVM could be incorporated into a hybrid DVM/CFD framework, where continuum methods resolve high-density regions and DVM handles the rarefied zones. Alternatively, a unified DVM-based multiscale solver – such as the Unified Gas-Kinetic Scheme (UGKS) [193] or the Discrete Unified Gas-Kinetic Scheme (DUGKS) [194, 195] – could be applied to seamlessly bridge different flow regimes without requiring explicit coupling interfaces. This approach is particularly promising for 3D simulations, as it could significantly reduce the computational cost associated with statistical fluctuations while maintaining high accuracy in regions with complex rarefied flow behavior.

An additional direction for future work involves the integration of machine-learning (ML) techniques into the simulation framework to improve modeling accuracy and computational efficiency. Traditional drag models often lack accuracy, particularly under highly rarefied conditions – where more detailed, relaxed stochastic models are needed [74]. These advanced models, although more accurate, are significantly more demanding concerning computational resources. By leveraging simulation data from hybrid DSMC/CFD studies under a range of flow and particle conditions, machine learning models can be trained to reproduce relaxed drag force behavior. Once trained, these surrogate models could provide fast and accurate drag predictions across multiple flow regimes, significantly reducing the computational cost of the simulations. Furthermore, such ML-based approaches, trained on simulation data, can be used to extend drag force models for nanoparticles exhibiting non-spherical or irregular geometries.

In addition, ML can be used to reduce the limitations of pure CFD-based flow predictions by learning the discrepancies between CFD and hybrid results, particularly in

near-rarefied conditions where continuum assumptions start to break down. Currently, work is underway to apply this approach to canonical test cases, with the intention of extending it to more complex injector configurations upon successful validation. Another promising application is related to design optimization. By generating simulation data across various ALS and BGC configurations, ML-driven surrogate models can be coupled with optimization algorithms to identify injector geometries that maximize focusing efficiency for specified particle types. These approaches can significantly reduce simulation time, guide experiment planning, and enable real-time parameter tuning in complex injection systems.

In summary, the outlook for advancing hybrid gas-particle simulation frameworks is broad and promising. By incorporating deterministic kinetic solvers, quantum-level modeling, and data-driven techniques, future research can overcome current limitations and enhance the predictive capability, efficiency, and versatility of nanoparticle injection simulations. These developments will be essential for optimizing injector performance and supporting next-generation single-particle imaging experiments.

A Suplementary information – chapter 2

The `fvSchemes` and `fvSolution` files provided in this appendix define the discretization schemes and solver settings used in the OpenFOAM simulations presented in this work.

A.1 fvSolution file - rhoCentralFoam

```
 FoamFile
{
    version     2.0;
    format      ascii;
    class       dictionary;
    location    "system";
    object      fvSolution;
}
// * * * * * * * * * * * * * * * * * * * * * * * * * * * * * * * * * * * * * * * * //
solvers
{
    "(rho|rhoU|rhoE)"
    {
        solver          diagonal;
    }
    U
    {
        solver          smoothSolver;
        smoother        GaussSeidel;
        nSweeps         2;
        tolerance       1e-09;
        relTol          0.01;
    }
    e
    {
        $U;
        tolerance       1e-10;
        relTol          0;
    }
}
```

A.2 fvSolution file - sonicFoam

```
    FoamFile
{
    version     2.0;
    format      ascii;
    class       dictionary;
    location    "system";
    object      fvSolution;
}
// * * * * * * * * * * * * * * * * * * * * * * * * * * * * * * * * * * * * * * * * * * //

solvers
{
    "p.*"
    {
        solver          PBiCGStab;
        preconditioner  DILU;
        tolerance       1e-16;
        relTol          0.01;
    }

    "(U|e).*"
    {
        $p;
        tolerance       1e-16;
        relTol          0.01;
    }

    "rho.*"
    {
        solver          diagonal;
    }
}
```

A.3 fvSchemes file - rhoCentralFoam

```
    FoamFile
{
    version     2.0;
    format      ascii;
    class       dictionary;
    location    "system";
    object      fvSchemes;
}
// * * * * * * * * * * * * * * * * * * * * * * * * * * * * * * * * * * * * * * * * //
fluxScheme          Kurganov;

ddtSchemes
{
    default         Euler;
}

gradSchemes
{
    default         Gauss linear;
    grad(U)         cellLimited Gauss linear 1;
}

divSchemes
{
    default         none;
    div(tauMC)      Gauss linear;
}

laplacianSchemes
{
    default        Gauss linear limited corrected 0.5;
}

interpolationSchemes
{
    default         linear;
    reconstruct(rho) vanLeer;
    reconstruct(U)  vanLeerV;
    reconstruct(T)  vanLeer;

}
snGradSchemes
```

A.4 fvSchemes file - sonicFoam

```
 FoamFile
{
    version     2.0;
    format      ascii;
    class       dictionary;
    location    "system";
    object      fvSchemes;
}
// * * * * * * * * * * * * * * * * * * * * * * * * * * * * * * * * * * * * * * * * * //
ddtSchemes
{
    default         Euler;
}
gradSchemes
{
    default         Gauss linear;
    grad(U)         cellLimited Gauss linear 1;
}
divSchemes
{
    default         none;
    div(phi,U)      Gauss vanLeerV;
    div(phid,p)     Gauss limitedLinear 1;
    div(phi,e)      Gauss limitedLinear 1;
    div(phi,K)      Gauss limitedLinear 1;
    div(phiv,p)     Gauss limitedLinear 1;
    div(((rho*nuEff)*dev2(T(grad(U))))) Gauss linear;
}
laplacianSchemes
{
    default        Gauss linear limited corrected 0.5;
}
interpolationSchemes
{
    default         linear;
}
snGradSchemes
{
    default         corrected;
}
```

B Suplementary information – chapter 6

B.1 Additional case – Focusing of 25 nm gold nanometer particles

In this section, an additional test case is presented. Figure B.1 shows the particle beam width at different positions after the ALS exit for gold spheres of 25 nm at an inlet pressure of 180 Pa. For this gold-sphere case, a slightly different ALS geometry is used [37]. It has to be noted that for this setup, the beam width is quantified based on 70 % quantile of particle positions in radial direction (d70) instead of FWHM. The hybrid DSMC/CFD approach is used along with the molecular drag force model (Eqs. (4.9)/(4.10) or Eqs. (4.11)/(4.12) based on the Mach number of the flow). As visible in Figure B.1, the results predicted by the simulation show very good agreement with the experimental data. Furthermore, the influence of Brownian diffusion (Eq. (4.20)) on the beam widths is also discussed. The simulation without the Brownian force model showed a drastic reduction in beam widths, clearly demonstrating the necessity of including this model. This additional application case underlines the suitability of the chosen simulation approach.

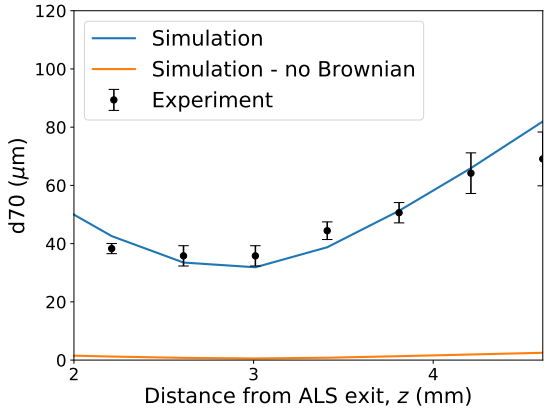

Fig. B.1. Particle-beam-size evolution of 25 nm AuNP at inlet pressure of 180 Pa.

C CMInject.jl: A Julia framework for the numerical simulation of nanoparticle injection pipelines[1]

The particle trajectory calculator, CMInject, described in Chapter 4, was originally developed and benchmarked in Python 3. To simplify numerical implementation and potentially enhance computational performance, a prototype version has been developed in Julia. The Julia implementation offers improved code alignment with mathematical notation, thereby increasing clarity for future contributors. In this chapter, the initial benchmarking results are presented, validate simulation tool against experimental data and its computational performance is evaluated by comparing the Julia and Python versions.

C.1 CMInject.jl

In the Julia build of CMInject, the Langevin dynamics are integrated directly as stochastic differential equations (SDEs) with an Euler-Heun scheme [197] provided by the `DifferentialEquations.jl` package [198], replacing the operator-splitting ODE approach used in the Python version described in Chapter 4. As in Python, `CMInject.jl` first reads the pre-computed flow-field data (velocity and pressure) and interpolates these values at every particle position. The drag (drift) and Brownian (diffusion) forces are then wrapped in an `SDEProblem` [199], promoted to an `EnsembleProblem` [200] for many separate runs, and solved in parallel with the Euler-Heun integrator via `EnsembleThreads`. The `EnsembleThreads` scheduler uses Julia's built-in multithreading to provide local, shared-memory parallelism on a single node. These wrappers let the solver be expressed in just a handful of clear calls, keeping the code nearly one-to-one with the governing equations while Julia transparently handles parallelism and data management. The framework supports nanoparticle-trajectory simulations in both 2-D and 3-D configurations, as illustrated in Figure C.1.

C.2 Sample test case and simulation settings

For benchmarking this Julia-based framework, the test case described in Appendix B was used – namely, the aerodynamic lens stack (ALS) geometry [37] with an inlet pressure of 180 Pa and 25 nm gold particles. The carrier gas flow is computed using the

[1] This chapter is based on work by S. K. Peravali et al., as presented at JuliaCon 2024 [196]. In this work, I served as the principal contributor, responsible for the development, analysis, and implementation of the underlying methods.

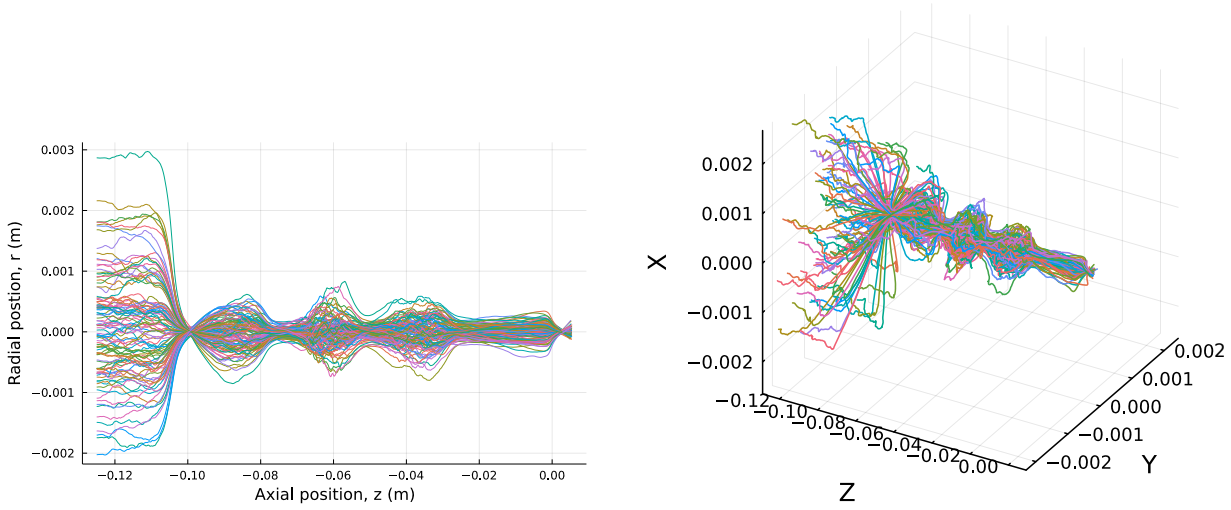

(a) 2D (b) 3D

Fig. C.1. Sample particle trajectory plots simulated using CMInject.jl.

hybrid DSMC/CFD methodology. Particle drag is modeled using the Stokes-Cunningham formulation (Eq. (4.5)), while Brownian motion is incorporated via Eqs. (4.17) and (4.18).

C.3 Results

Figure C.2 presents the evolution of the particle beam width at various positions downstream of the ALS exit for 25 nm gold spheres. The beam width is quantified using the 70% quantile of particle positions in radial direction (d70). The simulation results show excellent agreement with experimental measurements. Furthermore, a comparison between the Julia-based and Python-based frameworks under identical simulation settings shows negligible differences.

Simulation performance was evaluated by measuring wall-clock time as a function of the number of particle trajectories. Both the Julia and Python implementations ran on a single node of the HSUper HPC cluster at the Helmut-Schmidt University, which provides 72 hardware threads. Figure C.3 (a) and (b) plot the elapsed time versus particle count for the 2-D and 3-D test cases, respectively. In two dimensions, the Julia solver outperforms the Python version up to roughly 10^4 particles; beyond this threshold the Python implementation scales more favorably. In three dimensions, the Python code exhibits shorter runtimes than the Julia prototype across the entire range of particle numbers investigated.

To further assess the Julia framework, the code was profiled on the same ALS test case executed with 4 and 16 threads. Table C.1 lists a subset of representative call functions on the master thread, together with their wall-time speed-up from 4- to 16-thread execution. Most functions exhibit near-ideal scaling; however, the initialization routine `solve.jl` inside `DifferentialEquations.jl` scales poorly under `EnsembleThreads`, which may

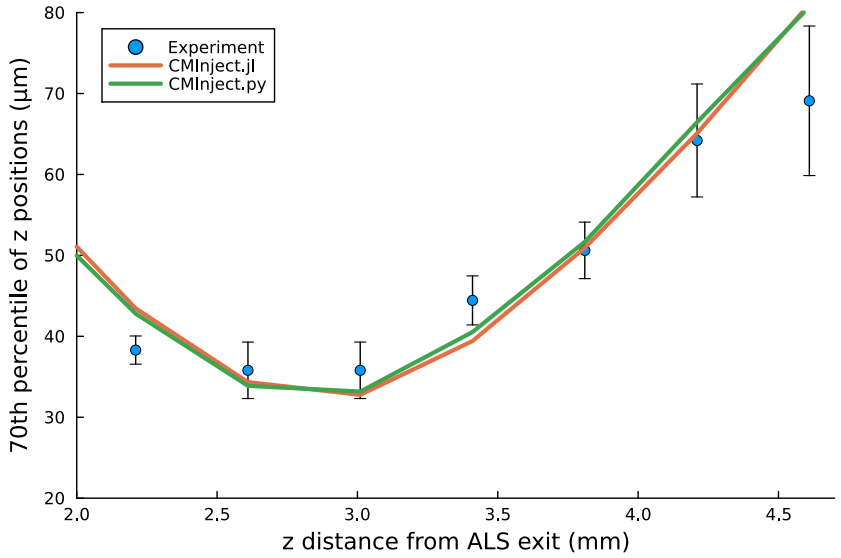

Fig. C.2. CMInject.py vs. CMInject.jl.

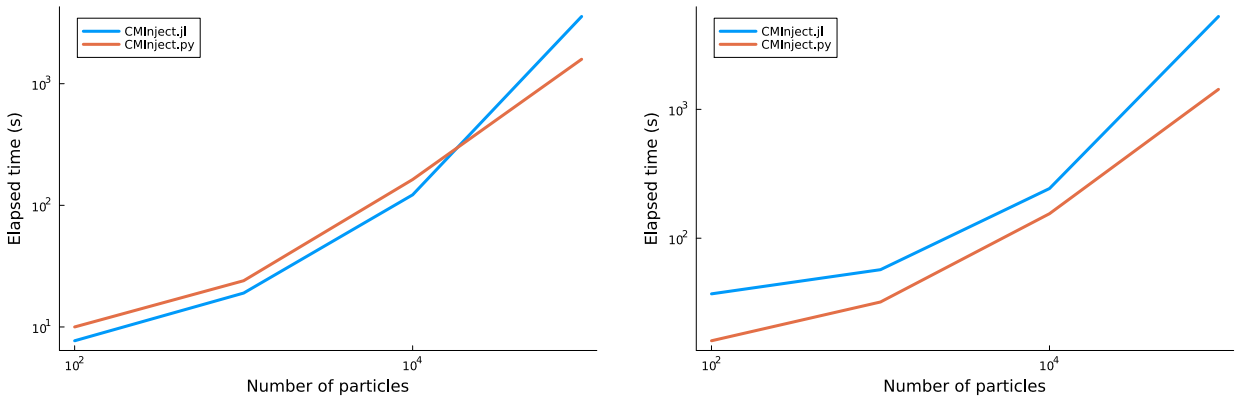

(a) 2D (b) 3D

Fig. C.3. Performance evaluation CMInject.jl compared with CMInject.py.

limit Julia performance at higher dimensions and larger particle counts. A detailed investigation of this bottleneck is planned for future work.

	4 Threads	16 Threads	Scaling Factor
Total time	11136 ms	4845 ms	2.298
Solve.jl	3681 ms	1332 ms	2.898
HDF5/interpolation	2095 ms	918 ms	2.282
_init solve.jl	641 ms	1682 ms	0.38

Tab. C.1. Call function and performance.

C.4 Concluding remark

For the ALS benchmark both frameworks – the operator-splitting Python code and the direct SDE solver implemented in Julia, yield identical particle-trajectory statistics, confirming numerical equivalence. The Python version achieves shorter wall-clock times once particle numbers and dimensionality become large, yet the Julia implementation attains comparable accuracy with far simpler, more transparent code.

D Suplementary information – chapter 7

The CFD simulation of the flat-plate flow was carried out using the `rhoCentralFoam` solver in OpenFOAM, as previously assessed in Chapter 5. The numerical setup including discretization schemes, interpolation techniques, and solver strategies were detailed in Chapter 2. These settings are implemented through the `fvSchemes` and `fvSolution` configuration files (see Appendix A). An overview of the boundary conditions applied in the simulation is provided in Table D.1.

Boundary	**U**	**P**	**T**
Inlet	fixed value	fixed value	fixed value
Outlet	zero gradient	wave transmissive	zero gradient
Wall	no-slip	zero gradient	fixed value
Top	symmetryPlane	symmetryPlane	symmetryPlane

Tab. D.1. Boundary conditions for the cryogenic helium flow over flat plate.

The flow is modeled as laminar owing to the low Reynolds number ($Re < 1000$), eliminating the need for turbulence modeling. Due to the absence of reliable Sutherland coefficients for helium at cryogenic temperatures, a constant-transport model (`constTransport`)[60] is used, in which the dynamic viscosity and Prandtl number are kept constant. These transport properties are selected based on helium data at the respective gas temperatures, as listed inTable D.2, using values from the NIST technical note [192]. The computational grid for the CFD simulations is generated using the `blockMesh` utility in OpenFOAM and consists of a structured mesh with 132×66 cells.

Gas temperature	**Dynamic viscosity** (Pa.s)	**Prandtl number**
293.14 K (room temp.)	1.96×10^{-5}	0.665
80 K	8.494×10^{-6}	0.6952
10.7 K	2.189×10^{-6}	0.6859
4 K	1.152×10^{-6}	1.135

Tab. D.2. Viscosity and Prandtl number of helium 4 at different temperatures.

D.1 OpenFOAM mesh for buffer-gas injector geometries

The computational grids for the CFD simulations are generated using the `blockMesh` and `snappyHexMesh` utilities in OpenFOAM. Figure D.1 and Figure D.2 show the structured body-fitted grids for the BGC and the BGC-ALS geometries respectively obtained by used above tools.

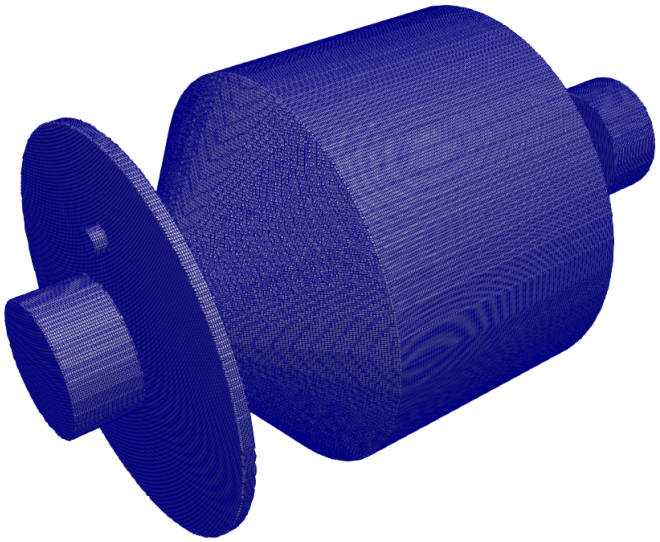

Fig. D.1. Structured body-fitted grid of the BGC geometry.

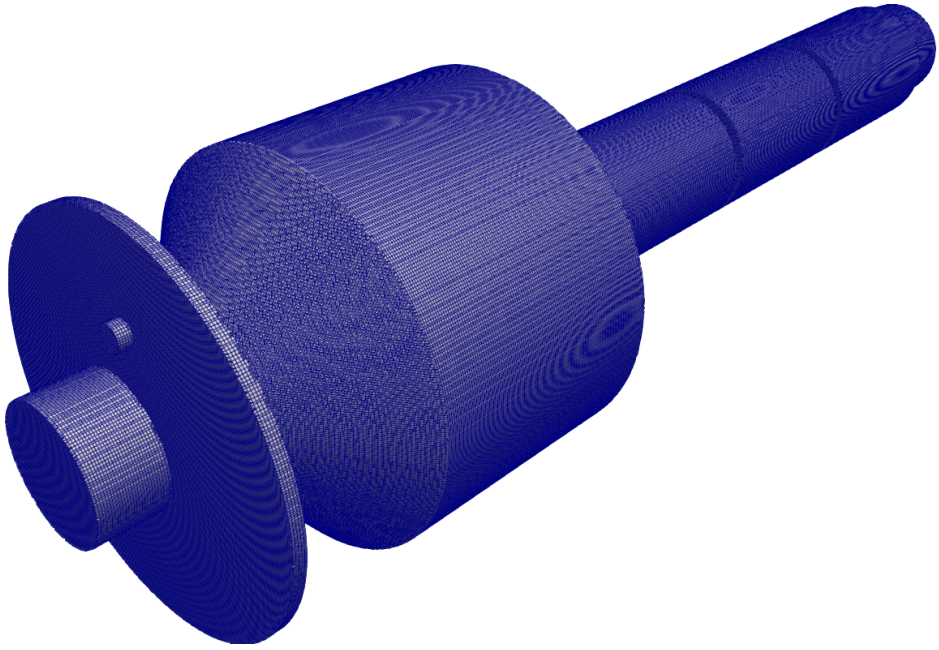

Fig. D.2. Structured body-fitted grid of the BGC-ALS geometry.

Bibliography

[1] R. Neutze, R. Wouts, D. van der Spoel, E. Weckert and J. Hajdu. Potential for biomolecular imaging with femtosecond X-ray pulses. *Nature* 406 (2000), 752–757. DOI: 10.1038/35021099.

[2] H. N. Chapman, A. Barty, M. J. Bogan, S. Boutet, M. Frank, S. P. Hau-Riege, S. Marchesini, B. W. Woods, S. Bajt, W. H. Benner, R. A. London, E. Plönjes, M. Kuhlmann, R. Treusch, S. Düsterer, T. Tschentscher, J. Schneider, E. Spiller, T. Möller and J. Hajdu. Femtosecond diffractive imaging with a soft-X-ray free-electron laser. *Nat. Phys.* 2 (2006), 839–843. DOI: 10.1038/nphys461.

[3] H. Chapman. John C. H. Spence and the Age of X-Ray Lasers. *Microscopy and Microanalysis* 28 (2022), 2758–2760. DOI: 10.1017/S1431927622010388.

[4] C. Feng and H. Deng. Review of fully coherent free-electron lasers. *Nuclear science and Technology* 29 (2018), 160. DOI: 10.1007/s41365-018-0490-1.

[5] N. Huang, H. Deng, B. Liu, D. Wang and Z. Zhao. Features and futures of X-ray free-electron lasers. *The Innovation* 2 (2) (2021), 100097. DOI: 10.1016/j.xinn.2021.100097.

[6] E. Sobolev, S. Zolotarev, K. Giewekemeyer, J. Bielecki, K. Okamoto, H. Reddy, J. Andreasson, K. Ayyer, I. Barák, S. Bari, A. Barty, R. Bean, S. Bobkov, H. Chapman, G. Chojnowski, B. Daurer, K. Dörner, T. Ekeberg, L. Flückiger and F. Maia. Megahertz single-particle imaging at the European XFEL. *Communications Physics* 3 (2020), 97. DOI: 10.1038/s42005-020-0362-y.

[7] M. J. Bogan, S. Boutet, H. N. Chapman, S. Marchesini, A. Barty, W. H. Benner, U. Rohner, M. Frank, S. P. Hau-Riege, S. Bajt, B. Woods, M. M. Seibert, B. Iwan, N. Timneanu, J. Hajdu and J. Schulz. Aerosol imaging with a soft X-ray free electron laser. *Aerosol Science and Technology* 44 (3) (2010), i–vi. DOI: 10.1080/02786820903485800.

[8] T. Ekeberg et al. Three-dimensional reconstruction of the giant mimivirus particle with an X-ray free-electron laser. *Phys. Rev. Lett.* 114 (9) (2015), 098102. DOI: 10.1103/PhysRevLett.114.098102.

[9] M. Seibert, T. Ekeberg, F. Maia, M. Svenda, J. Andreasson, O. Jönsson, D. Odić, B. Iwan, A. Rocker, D. Westphal, M. Hantke, D. DePonte, A. Barty, J. Schulz, L. Gumprecht, N. Coppola, A. Aquila, M. Liang, T. White and J. Hajdu. Single mimivirus particles intercepted and imaged with an X-ray laser. *Nature* 470 (2011), 78–81. DOI: 10.1038/nature09748.

[10] K. Ayyer, A. J. Morgan, A. Aquila, H. DeMirci, B. G. Hogue, R. A. Kirian, P. L. Xavier, C. H. Yoon, H. N. Chapman and A. Barty. Low-signal limit of X-ray single particle diffractive imaging. *Opt. Express* 27 (26) (2019), 37816–37833. DOI: 10.1364/OE.27.037816.

[11] K. Ayyer et al. 3D diffractive imaging of nanoparticle ensembles using an X-ray laser. *Optica* 8 (1) (2021), 15–23. DOI: 10.1364/OPTICA.410851.

[12] R. Fung, V. Shneerson, D. Saldin and A. Ourmazd. Structure from fleeting illumination of faint spinning objects in flight. *Nat. Phys.* 5 (2009). DOI: 10.1038/nphys1129.

[13] G. Bortel and G. Faigel. Classification of continuous diffraction patterns: A numerical study. *Journal of Structural Biology* 158 (1) (2007), 10–18. DOI: 10.1016/j.jsb.2006.10.018.

[14] Y. Shi, K. Yin, X. Tai, H. DeMirci, A. Hosseinizadeh, B. Hogue, H. Li, A. Ourmazd, P. Schwander, I. Vartanyants, C. Yoon, A. Aquila and H. Liu. Evaluation of the performance of classification algorithms for XFEL single-particle imaging data. English (US). *IUCrJ* 6 (2019), 331–340. DOI: 10.1107/S2052252519001854.

[15] T. Ekeberg et al. Observation of a single protein by ultrafast X-ray diffraction. *Light: Science & Applications* 13 (1) (2024), 15. DOI: 10.1038/s41377-023-01352-7.

[16] I. V. Lundholm et al. Considerations for three-dimensional image reconstruction from experimental data in coherent diffractive imaging. *IUCrJ* 5 (5) (2018), 531–541. DOI: 10.1107/S2052252518010047.

[17] M. F. Hantke et al. High-throughput imaging of heterogeneous cell organelles with an X-ray laser. *Nature Photonics* 8 (12) (2014), 943–949. DOI: 10.1038/nphoton.2014.270.

[18] R. P. Kurta et al. Correlations in scattered X-ray laser pulses reveal nanoscale structural features of viruses. *Phys. Rev. Lett.* 119 (15) (2017), 158102. DOI: 10.1103/PhysRevLett.119.158102.

[19] M. Rose et al. Single-particle imaging without symmetry constraints at an X-ray free-electron laser. *IUCrJ* 5 (6) (2018), 727–736. DOI: 10.1107/S205225251801120X.

[20] J. Bielecki, F. R. N. C. Maia and A. P. Mancuso. Perspectives on single particle imaging with x rays at the advent of high repetition rate X-ray free electron laser sources. *Structural Dynamics* 7 (4) (2020), 040901. DOI: 10.1063/4.0000024.

[21] J. Fan, J. Zhang and Z. Liu. Coherent diffraction imaging of cells at advanced X-ray light sources. *TrAC Trends in Analytical Chemistry* 171 (2024), 117492. DOI: 10.1016/j.trac.2023.117492.

[22] K. J. Gaffney and H. N. Chapman. Imaging atomic structure and dynamics with ultrafast X-ray scattering. *Science* 316 (5830) (2007), 1444–1448. DOI: 10.1126/science.1135923.

[23] J.-D. Fan, Y.-J. Tong, Y.-G. Nie, Z.-C. Gao, B. He, H. Luan, D.-H. Lu, J.-H. Zhang, D.-F. Zhang, X.-Y. Yuan, J.-H. Chen, Z. Guo, T. Liu, M. Zhang, C. Feng, H.-X. Deng, B. Liu, Z.-T. Zhao, Z. Liu and H.-D. Jiang. First commissioning results of the coherent scattering and imaging endstation at the Shanghai soft X-ray free-electron laser facility. *Nuclear Science and Techniques* 33 (9) (2022), 114. DOI: 10.1007/s41365-022-01103-0.

[24] D. Nam, C. Kim, Y. Kim, T. Ebisu, M. Gallagher-Jones, J. Park, S. Kim, S. Kim, K. Tono, D. Y. Noh, M. Yabashi, T. Ishikawa and C. Song. Fixed target single-shot imaging of nanostructures using thin solid membranes at SACLA. *Journal of Physics B: Atomic, Molecular and Optical Physics* 49 (3) (2016), 034008. DOI: 10.1088/0953-4075/49/3/034008.

[25] D. P. DePonte, U. Weierstall, K. Schmidt, J. Warner, D. Starodub, J. C. H. Spence and R. B. Doak. Gas dynamic virtual nozzle for generation of microscopic droplet streams. *Journal of Physics D: Applied Physics* 41 (19) (2008), 195505. DOI: 10.1088/0022-3727/41/19/195505.

[26] J. Bielecki et al. Electrospray sample injection for single-particle imaging with x-ray lasers. *Science Advances* 5 (5) (2019), eaav8801. DOI: 10.1126/sciadv.aav8801.

[27] I. Poudyal, M. Schmidt and P. Schwander. Single-particle imaging by x-ray free-electron lasers—How many snapshots are needed? *Structural Dynamics* 7 (2) (2020), 024102. DOI: 10.1063/1.5144516.

[28] P. Liu, P. Ziemann, D. Kittelson and P. McMurry. Generating particle beams of controlled dimensions and divergence: I. Theory of particle motion in aerodynamic lenses and nozzle expansions. English (US). *Aerosol Science and Technology* 22 (3) (1995), 293–313. DOI: 10.1080/02786829408959748.

[29] A. Robinson. On the motion of small particles in a potential field of flow. *Communications on Pure and Applied Mathematics* 9 (1) (1956), 69–84. DOI: 10.1002/cpa.3160090105.

[30] L. Qi, P. H. McMurry, D. J. Norris and S. L. Girshick. Micropattern Deposition of Colloidal Semiconductor Nanocrystals by Aerodynamic Focusing. *Aerosol Science and Technology* 44 (1) (2010), 55–60. DOI: 10.1080/02786820903376876.

[31] Y. Su, M. F. Sipin, H. Furutani and K. A. Prather. Development and Characterization of an Aerosol Time-of-Flight Mass Spectrometer with Increased Detection Efficiency. *Analytical Chemistry* 76 (3) (2004), 712–719. DOI: 10.1021/ac034797z.

[32] X. Wang, F. E. Kruis and P. H. McMurry. Aerodynamic focusing of nanoparticles: I. Guidelines for designing aerodynamic lenses for nanoparticles. *Aerosol Science and Technology* 39 (7) (2005), 611–623. DOI: 10.1080/02786820500181901.

[33] Aerodynamic focusing of particles and molecules in seeded supersonic jets. In: *Rarefied Gas Dynamics: Physical Phenomena*. 1989, 247–277. DOI: 10.2514/5.9781600865916.0247.0277.

[34] L. Worbs. Toward Cryogenic Beams of Nanoparticles and Proteins. Ph.D. thesis. Universität Hamburg, Hamburg, Germany, 2022. URL: https://ediss.sub.uni-hamburg.de/bitstream/ediss/9894/1/thesis.pdf.

[35] A. K. Samanta, M. Amin, A. D. Estillore, N. Roth, L. Worbs, D. A. Horke and J. Küpper. Controlled beams of shock-frozen, isolated, biological and artificial nanoparticles. *Structural Dynamics* 7 (2) (2020), 024304. DOI: 10.1063/4.0000004.

[36] N. Roth, S. Awel, D. A. Horke and J. Küpper. Optimizing aerodynamic lenses for single-particle imaging. *Journal of Aerosol Science* 124 (2018), 17–29. DOI: 10.1016/j.jaerosci.2018.06.010.

[37] L. Worbs, N. Roth, J. Lübke, A. D. Estillore, P. L. Xavier, A. K. Samanta and J. Küpper. Optimizing the geometry of aerodynamic lens injectors for single-particle coherent diffractive imaging of gold nanoparticles. *Journal of Applied Crystallography* 54 (6) (2021), 1730–1737. DOI: 10.1107/S1600576721009973.

[38] X. Wang, A. Gidwani, S. L. Girshick and P. H. McMurry. Aerodynamic focusing of nanoparticles: II. Numerical simulation of particle motion through aerodynamic lenses. *Aerosol Science and Technology* 39 (7) (2005), 624–636. DOI: 10.1080/02786820500181950.

[39] X. Zhang, K. A. Smith, D. R. Worsnop, J. Jimenez, J. T. Jayne and C. E. Kolb. A numerical characterization of particle beam collimation by an aerodynamic lens-nozzle system: Part I. An Individual Lens or Nozzle. *Aerosol Science and Technology* 36 (5) (2002), 617–631. DOI: 10.1080/02786820252883856.

[40] X. Zhang, K. A. Smith, D. R. Worsnop, J. L. Jimenez, J. T. Jayne, C. E. Kolb, J. Morris and P. Davidovits. Numerical characterization of particle beam collimation: Part II. integrated aerodynamic-lens-nozzle system. *Aerosol Science and Technology* 38 (6) (2004), 619–638. DOI: 10.1080/02786820490479833.

[41] X. Wang and P. H. McMurry. A design tool for aerodynamic lens systems. *Aerosol Science and Technology* 40 (5) (2006), 320–334. DOI: 10.1080/02786820600615063.

[42] S. Welker, M. Amin and J. Küpper. CMInject: Python framework for the numerical simulation of nanoparticle injection pipelines. *Computer Physics Communications* 270 (2022), 108138. DOI: 10.1016/j.cpc.2021.108138.

[43] G. A. Bird. *Molecular Gas Dynamics and Direct Simulation of Gas Flows*. Oxford. 1994.

[44] G. Abbate, B. Thijsse and C. Kleijn. Coupled Navier-Stokes/DSMC Method for Transient and Steady-State Gas Flows. In: *Computational Science – ICCS 2007*. Vol. 4487. 2007, 842–849. DOI: 10.1007/978-3-540-72584-8_111.

[45] E. Cunningham and J. Larmor. On the velocity of steady fall of spherical particles through fluid medium. *Proceedings of the Royal Society of London. Series A, Con-*

taining Papers of a Mathematical and Physical Character 83 (563) (1910), 357–365. DOI: 10.1098/rspa.1910.0024.

[46] P. S. Epstein. On the resistance experienced by spheres in their motion through gases. *Phys. Rev.* 23 (6) (1924), 710–733. DOI: 10.1103/PhysRev.23.710.

[47] M. J. Baines, I. P. Williams, A. S. Asebiomo and R. L. Agacy. Resistance to the motion of a small sphere moving through a gas. *Monthly Notices of the Royal Astronomical Society* 130 (1) (1965), 63–74. DOI: 10.1093/mnras/130.1.63.

[48] N. Singh, M. Kroells, C. Li, E. Ching, M. Ihme, C. J. Hogan and T. E. Schwartzentruber. General drag coefficient for flow over spherical particles. *AIAA Journal* 60 (2) (2022), 587–597. DOI: 10.2514/1.J060648.

[49] ESI-OpenCFD. *OpenFOAM - The Open Source CFD Toolbox*. https://www.openfoam.com. Version v2112. 2004–present.

[50] Sandia National Laboratories. *SPARTA - Stochastic PArallel Rarefied-gas Time-accurate Analyzer*. https://www.sparta.github.io. release 18 Jul 2022. 2022.

[51] J. Peraire, K. Morgan, J. Peiro and O. Zienkiewicz. An adaptive finite element method for high speed flows. In: *25th AIAA Aerospace Sciences Meeting*. DOI: 10.2514/6.1987-558.

[52] W. Sutherland. LII. The viscosity of gases and molecular force. *The London, Edinburgh, and Dublin Philosophical Magazine and Journal of Science* 36 (223) (1893), 507–531. DOI: 10.1080/14786449308620508.

[53] C. Greenshields. *OpenFOAM v12 User Guide*. The OpenFOAM Foundation. London, UK, 2024.

[54] C. M. Rhie and W. L. Chow. Numerical study of the turbulent flow past an airfoil with trailing edge separation. *AIAA Journal* 21 (11) (1983), 1525–1532. DOI: 10.2514/3.8284.

[55] A. Kurganov and E. Tadmor. New high-resolution central Schemes for nonlinear conservation laws and convection-diffusion equations. *Journal of Computational Physics* 160 (2000), 241–282. DOI: 10.1006/jcph.2000.6459.

[56] A. Kurganov, S. Noelle and G. Petrova. Semidiscrete central-upwind schemes for hyperbolic conservation laws and hamilton–jacobi equations. *SIAM Journal on Scientific Computing* 23 (3) (2001), 707–740. DOI: 10.1137/S1064827500373413.

[57] C. Greenshields, H. Weller, L. Gasparini and R. J. Implementation of semi-discrete, non-staggered central schemes in a colocated, polyhedral, finite volume framework, for high-speed viscous flows. *International Journal for Numerical Methods in Fluids* 62 (1) (2010), 1–21. DOI: 10.1002/fld.2069.

[58] R. Issa. Solution of the implicitly discretised fluid flow equations by operator-splitting. *Journal of Computational Physics* 62 (1) (1986), 40–65. DOI: 10.1016/0021-9991(86)90099-9.

[59] L. F. Gutiérrez Marcantoni, J. P. Tamagno and S. A. Elaskar. High speed flow simulation using OpenFOAM. In: *Mecánica Computacional*. Vol. 31. 16. Conference Proceedings. Salta, Argentina, 2012, 2939–2959.

[60] C. Greenshields and H. Weller. *Notes on Computational Fluid Dynamics: General Principles*. CFD Direct Ltd. Reading, UK, 2022.

[61] B. van Leer. Towards the ultimate conservative difference scheme. II. Monotonicity and conservation combined in a second-order scheme. *Journal of Computational Physics* 14 (4) (1974), 361–370. DOI: 10.1016/0021-9991(74)90019-9.

[62] H. A. van der Vorst. Bi-CGSTAB: A fast and smoothly converging variant of Bi-CG for the solution of nonsymmetric linear systems. *SIAM Journal on Scientific and Statistical Computing* 13 (2) (1992), 631–644. DOI: 10.1137/0913035.

[63] R. Barrett, M. Berry, T. Chan, J. Demmel, J. Donato, J. Dongarra, V. Eijkhout, R. Pozo, C. Romine and H. Van der Vorst. Templates for the solution of linear systems: Building blocks for iterative methods. *Mathematics of Computation* 64 (1996), 1349–1352. DOI: 10.2307/2153507.

[64] M.-S. Liou and C. J. Steffen. A new flux splitting scheme. *Journal of Computational Physics* 107 (1) (1993), 23–39. DOI: 10.1006/jcph.1993.1122.

[65] E. F. Toro, M. Spruce and W. Speares. Restoration of the contact surface in the HLL-Riemann solver. *Shock Waves* 4 (1) (1994), 25–34. DOI: 10.1007/BF01414629.

[66] P. Roe and J. Pike. Efficient construction and utilisation of approximate riemann solutions. In: *Proc. of the Sixth Int'l. Symposium on Computing Methods in Applied Sciences and Engineering, VI*. North-Holland Publishing Co. Versailles, France, 1985, 499–518.

[67] A. Lucas-Serrano, J. A. Font, J. M. Ibáñez and J. M. Martí. Assessment of a high-resolution central scheme for the solution of the relativistic hydrodynamics equations. *Astronomy &Astrophysics* 428 (2) (2004), 703–715. DOI: 10.1051/0004-6361:20035731.

[68] S. Jaisankar and S. Raghurama Rao. A central Rankine–Hugoniot solver for hyperbolic conservation laws. *Journal of Computational Physics* 228 (3) (2009), 770–798. DOI: 10.1016/j.jcp.2008.10.002.

[69] M. Pandolfi and D. D'Ambrosio. Numerical instabilities in upwind methods: Analysis and cures for the "Carbuncle" phenomenon. *Journal of Computational Physics* 166 (2) (2001), 271–301. DOI: 10.1006/jcph.2000.6652.

[70] T. Poinsot and S. Lelef. Boundary conditions for direct simulations of compressible viscous flows. *Journal of Computational Physics* 101 (1) (1992), 104–129. DOI: 10.1016/0021-9991(92)90046-2.

[71] G. J. Pringle. *Porting OpenFOAM to HECToR. A dCSE project*. Technical Report. EPCC, The University of Edinburgh. James Clerk Maxwell Building, Mayfield Road, Edinburgh, UK, 2010. URL: http://www.hector.ac.uk/cse/distributedcse/reports/openfoam/openfoam.pdf.

[72] HPC Advisory Council. *OpenFOAM Performance Benchmark and Profiling*. Technical Report. 2010. URL: http://www.hpcadvisorycouncil.com/pdf/OpenFOAM_Analysis_and_Profiling_Intel.pdf.

[73] S. K. Peravali, V. Jafari, A. K. Samanta, J. Küpper, M. Amin, P. Neumann and M. Breuer. Accuracy and performance evaluation of low density internal and external flow predictions using CFD and DSMC. *Computers & Fluids* (2024), 106346. DOI: 10.1016/j.compfluid.2024.106346.

[74] S. K. Peravali, A. K. Samanta, M. Amin, P. Neumann, J. Küpper and M. Breuer. An improved simulation methodology for nanoparticle injection through aerodynamic lens systems. *Physics of Fluids* 37 (3) (2025), 033380. DOI: 10.1063/5.0260295.

[75] M. Torrilhon. Modeling nonequilibrium gas flow based on moment equations. *Annual Review of Fluid Mechanics* 48 (2016), 429–458. DOI: 10.1146/annurev-fluid-122414-034259.

[76] H. Struchtrup. *Macroscopic Transport Equations for Rarefied Gas Flows: Approximation Methods in Kinetic Theory*. Springer. Berlin, Heidelberg, 2005. DOI: 10.1007/3-540-32386-4.

[77] L. Mieussens. Discrete-velocity models and numerical schemes for the Boltzmann-BGK equation in plane and axisymmetric geometries. *Journal of Computational Physics* 162 (2) (2000), 429–466. DOI: 10.1006/jcph.2000.6548.

[78] V. Aristov. *Direct Methods for Solving the Boltzmann Equation and Study of Nonequilibrium Flows*. Springer. 2001. DOI: 10.1007/978-94-010-0866-2.

[79] P. L. Bhatnagar, E. P. Gross and M. Krook. A model for collision processes in gases. I. Small amplitude processes in charged and neutral one-component systems. *Phys. Rev.* 94 (3) (1954), 511–525. DOI: 10.1103/PhysRev.94.511.

[80] E. M. Shakhov. Generalization of the Krook kinetic relaxation equation. *Fluid Dynamics* 3 (5) (1968), 95–96. DOI: 10.1007/BF01029546.

[81] J. Holway Lowell H. New statistical models for kinetic theory: Methods of construction. *Physics of Fluids* 9 (9) (1966), 1658–1673. DOI: 10.1063/1.1761920.

[82] L. Mieussens. A survey of deterministic solvers for rarefied flows. *AIP Conference Proceedings* 1628 (1) (2014), 943–951. DOI: 10.1063/1.4902695.

[83] W. Liu, Y. Y. Liu, L. M. Yang, Z. J. Liu, Z. Y. Yuan, C. Shu and C. J. Teo. Coupling improved discrete velocity method and G13-based gas kinetic flux solver: A hybrid method and its application for non-equilibrium flows. *Physics of Fluids* 33 (9) (2021), 092007. DOI: 10.1063/5.0062107.

[84] L. Luo, T. Huang, Q. Li and L. Wu. Multiscale simulation of rarefied polyatomic gas flow via DIG method (2025). DOI: 10.48550/arXiv.2501.10965.

[85] V. Ghazanfari, M. Shademan and F. Mansourzadeh. Investigation of feed flow effect using CFD-DSMC method in a gas centrifuge. *Journal of Nuclear Research and Applications* 2 (2022), 7–14. DOI: 10.24200/jon.2022.1027.

[86] H. Xiao, Y. Shang and D. Wu. DSMC Simulation and experimental validation of shock interaction in hypersonic low density flow. *The Scientific World Journal* 2014 (2014), 732765. DOI: 10.1155/2014/732765.

[87] F. La Torre, S. Kenjeres, C. R. Kleijn and J.-L. P. A. Moerel. Evaluation of micronozzle performance through DSMC, Navier-Stokes and coupled DSMC/Navier-Stokes approaches. In: *Computational Science–ICCS 2009: 9th Int. Conf. Baton Rouge, LA, USA, May 25-27, 2009 Proc., Part I 9*. Springer. 2009, 675–684. DOI: 10.1007/978-3-642-01970-8_67.

[88] M. Liu, X. Zhang, G. Zhang and Y. Chen. Study on micronozzle flow and propulsion performance using DSMC and continuum methods. *Acta Mechanica Sinica/Lixue Xuebao* 22 (2006), 409–416. DOI: 10.1007/s10409-006-0020-y.

[89] J. Moss, R. Wilmoth and J. Price. DSMC simulations of blunt body flows for Mars entries: Mars pathfinder and mars microprobe capsules. In: *32nd Thermophysics Conference*. 1997, 2508. DOI: 10.2514/6.1997-2508.

[90] Sandia Corporation. *Sparta Users Manual*. English. Version 18 July 2022. Sandia National Laboratories. 2022. 368 pp. URL: https://sparta.github.io/doc/Manual.pdf. July 18, 2022.

[91] C. White, M. Borg, T. Scanlon, S. Longshaw, B. John, D. Emerson and J. Reese. dsmcFoam+: An OpenFOAM based direct simulation Monte Carlo solver. *Computer Physics Communications* 224 (2018), 22–43. DOI: 10.1016/j.cpc.2017.09.030.

[92] C. Shen. *Rarefied Gas Dynamics: Fundamentals, Simulations and Micro Flows*. Springer. 2005. DOI: 10.1007/b138784.

[93] F. Alexander and A. Garcia. The direct simulation Monte Carlo method. *Computers in Physics* 11 (1997), 588–593. DOI: 10.1063/1.168619.

[94] SPARTA Developers. *SPARTA Benchmarks*. 2025. URL: https://sparta.github.io/bench.html (visited on 08/14/2022).

[95] A. Klothakis and I. K. Nikolos. Modeling of rarefied hypersonic flows using the massively parallel DSMC kernel SPARTA. In: *Proceedings of the 8th GRACM*

International Congress on Computational Mechanics. Conference paper. Volos, Greece, July 2015.

[96] G. A. Bird. *The DSMC Method: Version 1.2*. CreateSpace. 2013.

[97] J. J. Hinchen and W. M. Foley. Scattering molecular beams by metallic surfaces. In: *5th International Symposium on Rarefied Gas Dynamics*. 1966, 505.

[98] C. Cercignani and M. Lampis. Kinetic models for gas-surface interactions. *Transport Theory and Statistical Physics* 1 (2) (1971), 101–114. DOI: 10.1080/00411457108231440.

[99] R. G. Lord. Application of the Cercignani-Lampis scattering kernel to the DSMC calculation. In: *17th International Symposium on Rarefied Gas Dynamics*. 1991, 1427–1433.

[100] R. G. Lord. Some extensions to the Cercignani-Lampis gas-surface scattering kernel. *Physics of Fluids* A3 (1991), 706–710. DOI: 10.1063/1.858076.

[101] R. G. Lord. Some further extensions to the Cercignani-Lampis gas-surface interaction model. *Physics of Fluids* 7 (1995), 1159–1161. DOI: 10.1063/1.868557.

[102] K. Koura and H. Matsumoto. Variable soft sphere molecular model for inverse power law or Lennard-Jones potential. *Physics of Fluids* 3 (1991), 2459. DOI: 10.1063/1.858184.

[103] P. L. Larsen and C. Borgnakke. Statistical Collision Model for Simulating Polyatomic Gas with Restricted Energy Exchange. In: *Rarefied Gas Dynamics*. Ed. by M. Becker and M. Fiebig. Vol. A7. Proceedings contribution. DFVLR. 1974.

[104] P. S. Larsen and C. Borgnakke. Statistical collision model for Monte Carlo simulation of polyatomic gas mixture. *J. Comput. Phys* 18 (1975), 405. DOI: 10.1016/0021-9991(75)90094-7.

[105] C.-H. Chung, S. C. Kim, R. M. Stubbs and K. J. De Witt. Low-density nozzle flow by the direct simulation Monte Carlo and continuum methods. *Journal of Propulsion and Power* 11 (1) (1995), 64–70. DOI: 10.2514/3.23841.

[106] A. B. Weaver and A. A. Alexeenko. Revised variable soft sphere and Lennard-Jones model parameters for eight common gases up to 2200 K. *Journal of Physical and Chemical Reference Data* 44 (2015), 023103. DOI: 10.1063/1.4921245.

[107] J. G. Parker. Rotational and vibrational relaxation in diatomic gases. *Physics of Fluids* 2 (4) (1959), 449–462. DOI: 10.1063/1.1724417.

[108] J. A. Lordi and R. E. Mates. Rotational relaxation in nonpolar diatomic gases. *Physics of Fluids* 13 (2) (1970), 291–308. DOI: 10.1063/1.1692920.

[109] N. Hadjiconstantinou, A. Garcia, M. Bazant and G. He. Statistical error in particle simulations of hydrodynamic phenomena. *Journal of Computational Physics* 187 (2003), 274–297. DOI: 10.1016/S0021-9991(03)00099-8.

[110] D. Wadsworth and D. Erwin. One-dimensional hybrid continuum/particle simulation approach for rarefied hypersonic flows. In: *5th Joint Thermophysics and Heat Transfer Conference*. DOI: 10.2514/6.1990-1690.

[111] D. Wadsworth and D. Erwin. Two-dimensional hybrid continuum/particle approach for rarefied flows. In: *23rd Plasmadynamics and Lasers Conference*. DOI: 10.2514/6.1992-2975.

[112] D. B. Hash and H. A. Hassan. Assessment of schemes for coupling Monte Carlo and Navier-Stokes solution methods. *Journal of Thermophysics and Heat Transfer* 10 (2) (1996), 242–249. DOI: 10.2514/3.781.

[113] D. Hash and H. Hassan. A decoupled DSMC/Navier-Stokes analysis of a transitional flow experiment. In: *34th Aerospace Sciences Meeting and Exhibit*. DOI: 10.2514/6.1996-353.

[114] J. George and I. Boyd. Simulation of nozzle plume flows using a combined CFD-DSMC approach. In: *33rd Thermophysics Conference*. DOI: 10.2514/6.1999-3454.

[115] A. L. Garcia and B. J. Alder. Generation of the Chapman–Enskog distribution. *Journal of Computational Physics* 140 (1) (1998), 66–70. DOI: 10.1006/jcph.1998.5889.

[116] I. Boyd. Predicting breakdown of the continuum equations under rarefied flow conditions. *AIP Conference Proceedings* 663 (2003), 899–906. DOI: 10.1063/1.1581636.

[117] G. A. Bird. Breakdown of translational and rotational equilibrium in gaseous expansions. *AIAA Journal* 8 (11) (1970), 1998–2003. DOI: 10.2514/3.6037.

[118] R. Cattolica, F. Robben, L. Talbot and D. R. Willis. Translational nonequilibrium in free jet expansions. *Physics of Fluids* 17 (10) (1974), 1793–1807. DOI: 10.1063/1.1694620.

[119] I. D. Boyd, G. Chen and G. V. Candler. Predicting failure of the continuum fluid equations in transitional hypersonic flows. *Physics of Fluids* 7 (1) (1995), 210–219. DOI: 10.1063/1.868720.

[120] W.-L. Wang and I. Boyd. Hybrid DSMC-CFD simulations of hypersonic flow over sharp and blunted bodies. In: *36th AIAA Thermophysics Conference, Orlando, Florida, USA*. Orlando, Florida, USA, 2003, 1–13. DOI: 10.2514/6.2003-3644.

[121] M. Pfeiffer, A. Mirza and P. Nizenkov. Evaluation of particle-based continuum methods for a coupling with the direct simulation Monte Carlo method based on a nozzle expansion. *Physics of Fluids* 31 (2019), 073601. DOI: 10.1063/1.5098085.

[122] K. Swaminathan-Gopalan and K. A. Stephani. Recommended direct simulation Monte Carlo collision model parameters for modeling ionized air transport processes. *Physics of Fluids* 28 (2) (2016), 027101. DOI: 10.1063/1.4939719.

[123] X. Ze. DSMC Simulation on Couette flow in micro-channels. In: *Proceedings of the 2017 2nd Int. Conference on Materials Science, Machinery and Energy Engineering (MSMEE 2017)*. Atlantis Press. 2017/05, 991–994. DOI: 10.2991/msmee-17.2017.192.

[124] S. K. Stefanov, R. W. Barber, M. Ota and D. R. Emerson. Comparison between Navier-Stokes and DSMC calculations for low Reynolds number slip flow past a confined microsphere. In: *Rarefied Gas Dynamics: 24th International Symposium on Rarefied Gas Dynamics*. Ed. by M. Capitelli. Vol. 762. AIP Conference Series. 2005, 701–706. DOI: 10.1063/1.1941617.

[125] C. E. Glass and T. J. Horvath. Comparison of a 3-D CFD-DSMC solution methodology with a wind tunnel experiment. *AIP Conference Proceedings* 663 (1) (2003), 441–448. DOI: 10.1063/1.1581580.

[126] S. J. Plimpton, S. G. Moore, A. Borner, A. K. Stagg, T. P. Koehler, J. R. Torczynski and M. A. Gallis. Direct simulation Monte Carlo on petaflop supercomputers and beyond. *Physics of Fluids* 31 (8) (2019), 086101. DOI: 10.1063/1.5108534.

[127] M. Ivanov, G. Markelov, S. Taylor and J. Watts. Parallel DSMC strategies for 3D computations. In: *Parallel Computational Fluid Dynamics 1996*. Ed. by P. Schiano, A. Ecer, J. Periaux and N. Satofuka. North-Holland. Amsterdam, 1997, 485–492. DOI: 10.1016/B978-044482327-4/50128-5.

[128] M. A. Gallis, J. R. Torczynski, S. J. Plimpton, D. J. Rader and T. Koehler. Direct simulation Monte Carlo: The quest for speed. *AIP Conference Proceedings* 1628 (1) (2014), 27–36. DOI: 10.1063/1.4902571.

[129] G. O. Khanlarov and G. A. Lukianov. DSMC of the inner atmosphere of a comet on shared memory multiprocessors. In: *High-Performance Computing and Networking*. Ed. by P. Sloot, M. Bubak, A. Hoekstra and B. Hertzberger. Springer Berlin Heidelberg. Berlin, Heidelberg, 1999, 1187–1189.

[130] E. Roohi and M. Darbandi. Recommendations on performance of parallel DSMC algorithm in solving subsonic nanoflows. *Applied Mathematical Modelling* 36 (5) (2012), 2314–2321. DOI: 10.1016/j.apm.2011.08.036.

[131] J. Li, Z. Zhang, L. Deng, X. Ding, D. Jiang and P. Wang. Massively Parallel Acceleration of Unstructured DSMC Computing. In: *Proceedings of the 2022 6th High Performance Computing and Cluster Technologies Conference*. HPCCT '22. Association for Computing Machinery. Fuzhou, China, 2022, 1–6. DOI: 10.1145/3560442.3560443.

[132] M. Braunstein and J. Cline. Progress on parallelizing a general purpose direct simulation Monte Carlo (DSMC) Code for High Performance Computing Applications. In: *NASA Publications 20030107284, AMOS 2003 Technical Conference, Maui, HI, United States, 10 Sep. 2003*. 2003.

[133] M. Celoria. Porting of DSMC to multi-GPUs using OpenACC. In: *Master Thesis*. SISSA. 2022, 5–63.

[134] C. Virgile, A. Albert and L. Julien. Optimisation of a hybrid NS–DSMC methodology for continuous–rarefied jet flows. *Acta Astronautica* 195 (2022), 295–308. DOI: 10.1016/j.actaastro.2022.03.012.

[135] G. Malaikannan, R. Kumar and A. K. Chinnappan. A novel efficient hybrid DSMC–dynamic collision limiter algorithm for multiscale transitional flows. *International Journal for Numerical Methods in Fluids* 86 (9) (2018), 565–581. DOI: 10.1002/fld.4466.

[136] D. E. R. Espinoza, V. Casseau, T. J. Scanlon and R. E. Brown. An open-source hybrid CFD-DSMC solver for high speed flows. *AIP Conference Proceedings* 1786 (1) (2016), 050007. DOI: 10.1063/1.4967557.

[137] K. Farber, P. Farber, J. Gräbel, S. Krick, J. Reitz and P. Ueberholz. Development and validation of a coupled Navier-Stokes/DSMC simulation for rarefied gas flow in the production process for OLEDs. *Appl. Math. Comput.* 272 (P3) (2016), 648–656. DOI: 10.1016/j.amc.2015.05.040.

[138] G. Abbate, C. R. Kleijn and B. J. Thijsse. Validation of a hybrid Navier-Stokes/DSMC method for multiscale transient and steady-state gas flows. *International Journal for Multiscale Computational Engineering* 6 (2008), 1–12. DOI: 10.1615/IntJMultCompEng.v6.i1.10.

[139] M. Auweter-Kurtz, M. Fertig, D. Petkow, T. Stindl, M. Quandt, C.-D. Munz, P. Adamidis, M. Resch, S. Roller, D. D'Andrea and R. Schneider. Development of a hybrid PIC/DSMC code. In: *29th Int. Electric Propulsion Conference*. 2005, 1–15.

[140] J. S. Wu, Y. Y. Lian, G. Cheng and Y.-S. Chen. Parallel hybrid particle-continuum (DSMC-NS) flow simulations using 3-D unstructured mesh. *Parallel Computational Fluid Dynamics 2006* (2007), 1–10. DOI: 10.1016/B978-044453035-6/50003-1.

[141] D. A. Fedosov, S. V. Rogasinsky, M. I. Zeifman, M. S. Ivanov, A. A. ALexeenko and D. A. Levin. Analysis of numerical errors in the DSMC method. *AIP Conference Proceedings* 762 (1) (2005), 589–594. DOI: 10.1063/1.1941600.

[142] G. Chen and I. D. Boyd. Statistical error analysis for the direct simulation Monte Carlo technique. *Journal of Computational Physics* 126 (2) (1996), 434–448. DOI: 10.1006/jcph.1996.0148.

[143] M. Y. Plotnikov and E. V. Shkarupa. Selection of sampling numerical parameters for the DSMC method. *Computers & Fluids* 58 (12) (2012), 102–111. DOI: 10.1016/j.compfluid.2012.01.007.

[144] M. Hedahl and R. Wilmoth. *Comparisons of the Maxwell and CLL gas/surface interaction models using DSMC*. Tech. rep. NASA Langley Research Center Hampton, VA, United States. 1996.

[145] K. Koura and H. Matsumoto. Variable soft sphere molecular model for inverse power law or Lennard-Jones potential. *Physics of Fluids A: Fluid Dynamics* 3 (1991), 2459. DOI: 10.1063/1.858184.

[146] A. Falchi, E. Minisci, M. Vasile and M. Kubicek. Aero-thermal re-entry sensitivity analysis using DSMC and a high dimensional model representation-based approach. In: *7th European Conference on Space Debris*. 2017, 1–11.

[147] P. Armand, D. Boulaud, M. Pourprix and J. Vendel. Two-fluid modeling of aerosol transport in laminar and turbulent flows. *Journal of Aerosol Science* 29 (8) (1998), 961–983. DOI: 10.1016/S0021-8502(98)00006-8.

[148] M. Alletto and M. Breuer. One–way, two–way and four–way coupled LES predictions of a particle–laden turbulent flow at high mass loading downstream of a confined bluff body. *Int. J. Multiphase Flow* 45 (2012), 70–90. DOI: 10.1016/j.ijmultiphaseflow.2012.05.005.

[149] M. Breuer and M. Alletto. Efficient simulation of particle–laden turbulent flows with high mass loadings using LES. *Int. J. Heat Fluid Flow* 35 (2012), 2–12. DOI: 10.1016/j.ijheatfluidflow.2012.01.001.

[150] R. S. C. Davuluri, S. C. C. Bailey, K. A. Tagavi and A. Martin. A drag coefficient model for Lagrangian particle dynamics relevant to high-speed flows. *International Journal of Heat and Fluid Flow* 87 (2021), 108706. DOI: 10.1016/j.ijheatfluidflow.2020.108706.

[151] C. Altantzis, R. Bates and A. Ghoniem. 3D Eulerian modeling of thin rectangular gas-solid fluidized beds: Estimation of the specularity coefficient and its effects on bubbling dynamics and circulation times. *Powder Technology* 270 (2015), 256–270. DOI: 10.1016/j.powtec.2014.10.029.

[152] S. Cloete, S. T. Johansen and S. Amini. Grid independence behaviour of fluidized bed reactor simulations using the Two Fluid Model: Effect of particle size. *Powder Technology* 269 (2015), 153–165. DOI: 10.1016/j.powtec.2014.08.055.

[153] C. Ilea, P. Kosinski and A. Hoffmann. Three-dimensional simulation of a dust lifting process with varying parameters. *International Journal of Multiphase Flow* 34 (9) (2008), 869–878. DOI: 10.1016/j.ijmultiphaseflow.2008.02.007.

[154] H. Utkilen, B. V. Balakin and P. Kosinski. Numerical study of dust lifting using the Eulerian–Eulerian approach. *Journal of Loss Prevention in the Process Industries* 27 (2014), 89–98. DOI: 10.1016/j.jlp.2013.11.009.

[155] X. Wang, A. Gidwani, S. Girshick and P. McMurry. Aerodynamic focusing of nanoparticles: II. Numerical simulation of particle motion through aerodynamic lenses. *Aerosol Science and Technology* 39 (7) (2005), 624–636. DOI: 10.1080/02786820500181950.

[156] X. Wang, F. E. Kruis and P. H. McMurry. Aerodynamic Focusing of Nanoparticles: I. Guidelines for Designing Aerodynamic Lenses for Nanoparticles. *Aerosol Science and Technology* 39 (7) (2005), 611–623. DOI: 10.1080/02786820500181901.

[157] X. Wang and P. H. McMurry. A design tool for aerodynamic lens systems. *Aerosol Science and Technology* 40 (5) (2006), 320–334. DOI: 10.1080/02786820600615063.

[158] C. B. Henderson. Drag coefficients of spheres in continuum and rarefied Flows. *AIAA Journal* 14 (6) (1976), 707–708. DOI: 10.2514/3.61409.

[159] E. Loth. Compressibility and rarefaction effects on drag of a spherical particle. *AIAA Journal* 46 (9) (2008), 2219–2228. DOI: 10.2514/1.28943.

[160] C. Li, N. Singh, A. Andrews, B. A. Olson, T. E. Schwartzentruber and C. J. Hogan. Mass, momentum, and energy transfer in supersonic aerosol deposition processes. *International Journal of Heat and Mass Transfer* 129 (2019), 1161–1171. DOI: 10.1016/j.ijheatmasstransfer.2018.10.028.

[161] M. A. Gallis, J. R. Torczynski and D. J. Rader. An approach for simulating the transport of spherical particles in a rarefied gas flow via the direct simulation Monte Carlo method. *Physics of Fluids* 13 (11) (2001), 3482–3492. DOI: 10.1063/1.1409367.

[162] J. Burt. Monte Carlo simulation of solid rocket exhaust plumes at high altitude. Ph.D. thesis. University of Michigan, USA, 2006.

[163] A. Li and G. Ahmadi. Dispersion and deposition of spherical particles from point sources in a turbulent channel flow. *Aerosol Science and Technology* 16 (4) (1992), 209–226. DOI: 10.1080/02786829208959550.

[164] P. Virtanen et al. SciPy 1.0: Fundamental algorithms for scientific computing in Python. *Nature Methods* 17 (3) (2020), 261–272. DOI: 10.1038/s41592-019-0686-2.

[165] L. Petzold. Automatic selection of methods for solving stiff and nonstiff systems of ordinary differential Equations. *SIAM Journal on Scientific and Statistical Computing* 4 (1) (1983), 136–148. DOI: 10.1137/0904010.

[166] D. K. Hutchins, M. H. Harper and R. L. Felder. Slip correction measurements for solid spherical particles by modulated dynamic light scattering. *Aerosol Science and Technology* 22 (2) (1995), 202–218. DOI: 10.1080/02786829408959741.

[167] R. A. Millikan. Coefficients of slip in gases and the law of reflection of molecules from the surfaces of solids and liquids. *Phys. Rev.* 21 (3) (1923), 217–238. DOI: 10.1103/PhysRev.21.217.

[168] R. A. Millikan. The general law of fall of a small spherical body through a gas, and its bearing upon the nature of molecular reflection from surfaces. *Phys. Rev.* 22 (1) (1923), 1–23. DOI: 10.1103/PhysRev.22.1.

[169] M. Allen and O. Raabe. Re-evaluation of Millikan's oil drop data for the motion of small particles in air. *Journal of Aerosol Science* 13 (6) (1982), 537–547. DOI: 10.1016/0021-8502(82)90019-2.

[170] N. Roth, M. Amin, A. K. Samanta and J. Küpper. *Microscopic force for aerosol transport*. 2020. DOI: 10.48550/arXiv.2006.10652.

[171] D. E. Rothe. *Experimental Study of Viscous Low-Density Nozzle Flows*. Tech. rep. CAL-AI-2590-A-2, Cornell Aeronautical Laboratory, Inc., Cornell University, Buffalo, New York. 1970.

[172] F.M.White. *Viscous Fluid Flow*. McGraw-Hill. 2006.

[173] W.-L. Wang, Q. Sun and I. Boyd. Towards development of a hybrid DSMC-CFD method for simulating hypersonic interacting flows. *AIAA Paper* (2002), 2002–3099, DOI: 10.2514/6.2002-3099.

[174] J. Moss and G. Bird. DSMC simulations of hypersonic flows with shock interactions and validation with experiments. In: *37th AIAA Thermophysics Conference*. 2004, 2585. DOI: 10.2514/6.2004-2585.

[175] E. Y.-K. Ng and N. Liu. The impacts of time-step size in the application of the direct simulation Monte Carlo method to ultra-thin gas film lubrication. *Journal of Micromechanics and Microengineering* 12 (5) (2002), 567. DOI: 10.1088/0960-1317/12/5/309.

[176] Y. Georgiou, T. Cadeau, D. Glesser, D. Auble, M. Jette and M. Hautreux. Energy accounting and control with SLURM resource and job management system. In: *Distributed Computing and Networking*. Springer Berlin Heidelberg. Berlin, Heidelberg, 2014, 96–118. DOI: 10.1007/978-3-642-45249-9_7.

[177] S. Awel, R. A. Kirian, N. Eckerskorn, M. Wiedorn, D. A. Horke, A. V. Rode, J. Küpper and H. N. Chapman. Visualizing aerosol-particle injection for diffractive-imaging experiments. *Opt. Express* 24 (6) (2016), 6507–6521. DOI: 10.1364/OE.24.006507.

[178] S. K. Peravali, A. K. Samanta, J. Küpper, M. Amin, P. Neumann and M. Breuer. Exploitation of continuum and kinetic theory approaches for the simulation of particle beam experiments. In: *Proceedings of the 33rd International Symposium on Rarefied Gas Dynamics*. Springer Nature. 2025.

[179] N. R. Hutzler, H.-I. Lu and J. M. Doyle. The buffer gas beam: An intense, cold, and slow source for atoms and molecules. *Chemical Reviews* 112 (9) (2012), 4803–4827. DOI: 10.1021/cr200362u.

[180] S. E. Maxwell, N. Brahms, R. deCarvalho, D. R. Glenn, J. S. Helton, S. V. Nguyen, D. Patterson, J. Petricka, D. DeMille and J. M. Doyle. High-flux beam source for cold, slow atoms or molecules. *Phys. Rev. Lett.* 95 (17) (2005), 173201. DOI: 10.1103/PhysRevLett.95.173201.

[181] T. Gantner, M. Koller, X. Wu, G. Rempe and M. Zeppenfeld. Buffer-gas cooling of molecules in the low-density regime: comparison between simulation and experiment. *Journal of Physics B: Atomic, Molecular and Optical Physics* 53 (14) (2020), 145302. DOI: 10.1088/1361-6455/ab8b42.

[182] V. Singh, A. K. Samanta, N. Roth, D. Gusa, T. Ossenbrüggen, I. Rubinsky, D. A. Horke and J. Küpper. Optimized cell geometry for buffer-gas-cooled molecular-beam sources. *Phys. Rev. A* 97 (3) (2018), 032704. DOI: 10.1103/PhysRevA.97.032704.

[183] S. Truppe, M. Hambach, S. M. Skoff, N. E. Bulleid, J. S. Bumby, R. J. Hendricks, E. A. Hinds, B. E. Sauer and M. R. T. and. A buffer gas beam source for short, intense and slow molecular pulses. *Journal of Modern Optics* 65 (5-6) (2018), 648–656. DOI: 10.1080/09500340.2017.1384516.

[184] N. E. Bulleid, S. M. Skoff, R. J. Hendricks, B. E. Sauer, E. A. Hinds and M. R. Tarbutt. Characterization of a cryogenic beam source for atoms and molecules. *Phys. Chem. Chem. Phys.* 15 (29) (2013), 12299–12307. DOI: 10.1039/C3CP51553B.

[185] O. Schullian, J. Loreau, N. Vaeck, A. van der Avoird, B. Heazlewood, C. Rennick and T. S. and. Simulating rotationally inelastic collisions using a direct simulation Monte Carlo method. *Molecular Physics* 113 (24) (2015), 3972–3978. DOI: 10.1080/00268976.2015.1098740.

[186] M. J. Doppelbauer, O. Schullian, J. Loreau, N. Vaeck, A. van der Avoird, C. J. Rennick, T. P. Softley and B. R. Heazlewood. Using a direct simulation Monte Carlo approach to model collisions in a buffer gas cell. *The Journal of Chemical Physics* 146 (4) (2017), 044302. DOI: 10.1063/1.4974253.

[187] Y. Takahashi, D. Shlivko, G. Woolls and N. R. Hutzler. Simulation of cryogenic buffer gas beams. *Phys. Rev. Res.* 3 (2) (2021), 023018. DOI: 10.1103/PhysRevResearch.3.023018.

[188] O. Schullian and B. R. H. and. Beyond direct simulation Monte Carlo (DSMC) modelling of collision environments. *Molecular Physics* 117 (21) (2019), 3076–3087. DOI: 10.1080/00268976.2019.1602740.

[189] O. Schullian, H. S. Antila and B. R. Heazlewood. A variable time step self-consistent mean field DSMC model for three-dimensional environments. *The Journal of Chemical Physics* 156 (12) (2022), 124309. DOI: 10.1063/5.0083033.

[190] M. Becker, F. Robben and R. Cattilica. Velocity distribution functions near the leading edge of a flat plate. *AIAA Journal* 12 (9) (1974), 1247–1253. DOI: 10.2514/3.49461.

[191] F. Sharipov. Modeling of transport phenomena in gases based on quantum scattering. *Physica A: Statistical Mechanics and its Applications* 508 (2018), 797–805. DOI: 10.1016/j.physa.2018.05.129.

[192] V. D. Arp, R. D. McCarty and D. G. Friend. *Thermophysical Properties of Helium-4 from 0.8 to 1500 K with Pressures to 2000 Mpa*. Tech. rep. Technical Note 1334. National Institute of Standards and Technology (NIST). Washington, D.C., 1998.

[193] K. Xu and J.-C. Huang. A unified gas-kinetic scheme for continuum and rarefied flows. *Journal of Computational Physics* 229 (20) (2010), 7747–7764. DOI: 10.1016/j.jcp.2010.06.032.

[194] Z. Guo, K. Xu and R. Wang. Discrete unified gas kinetic scheme for all Knudsen number flows: Low-speed isothermal case. *Phys. Rev. E* 88 (3) (2013), 033305. DOI: 10.1103/PhysRevE.88.033305.

[195] Z. Guo, R. Wang and K. Xu. Discrete unified gas kinetic scheme for all Knudsen number flows. II. Thermal compressible case. *Phys. Rev. E* 91 (3) (2015), 033313. DOI: 10.1103/PhysRevE.91.033313.

[196] S. K. Peravali. *Simulating nano-particle trajectories using CMInject.jl*. Presented at JuliaCon 2024. https://youtu.be/V-VbC4xIq-4. 2024.

[197] P. E. Kloeden and E. Platen. *Numerical Solution of Stochastic Differential Equations*. Applications of Mathematics. Springer. 1992. DOI: 10.1007/978-3-662-12616-5.

[198] SciML Developers. *DifferentialEquations.jl Documentation*. https://docs.sciml.ai/DiffEqDocs/stable/. 2025.

[199] SciML Developers. *SDE Problems — DifferentialEquations.jl Documentation*. https://docs.sciml.ai/DiffEqDocs/stable/types/sde_types/. 2025.

[200] SciML Developers. *Parallel Ensemble Simulations — DifferentialEquations.jl Documentation*. https://diffeq.sciml.ai/stable/features/ensemble/. 2025.

Publications and conference contributions

The following is a complete, chronologically ordered list of publications and conference contributions associated with the present thesis.

Peer reviewed publications

- S. K. Peravali, A. K. Samanta, M. Amin, P. Neumann, J. Küpper and M. Breuer, "An improved simulation methodology for nanoparticle injection through aerodynamic lens systems", *Physics of Fluids* **37** (3), 033380 (2025). DOI: 10.1063/5.0260295.
- S. K. Peravali, V. Jafari, A. K. Samanta, J. Küpper, M. Amin, P. Neumann and M. Breuer, "Accuracy and performance evaluation of low density internal and external flow predictions using CFD and DSMC", *Computers & Fluids* **279**, 106346 (2024). DOI: 10.1016/j.compfluid.2024.106346.

Peer reviewed publications (In press)

- S. K. Peravali, A. K. Samanta, M. Amin, P. Neumann, J. Küpper and M. Breuer, "Exploitation of continuum and kinetic theory approaches for the simulation of particle beam experiments", accepted for publication in *Proc. 33rd Int. Symp. Rarefied Gas Dyn.*, Springer Nature (2025).

Manuscripts in preparation

- S. K. Peravali, L. Worbs, J. He, A. D. Estilore, A. K. Samanta, P. Neumann, M. Breuer and J. Küpper, "Aerodynamic-lens-stack injector with cryogenic cooling: Toward efficient focusing of protein-sized nanoparticles," planned for submission to *Phys. Rev. Fluids* (2025).

Conference contributions

- DESY/Europen XFEL Simulation Users' meeting, Hamburg, Germany, *invited talk* (2024).
- 33rd International Symposium on Rarefied Gas Dynamics, Göttingen, Germany, *contributed talk* (2024).

- JuliaCon2024, Eindhoven, Netherlands, *contributed talk* (2024).
- Deutsche Physikalische Gesellschaft (DPG) SKM Frühjahrstagung, Berlin, Germany, *contributed talk and poster* (2024).
- RGD NextGen talks, Online, *invited talk* (2024).
- DESY photon science users meeting and Europen XFEL users meeting, Hamburg, Germany, *poster* (2024).
- DSMC Conference, Santa Fe, USA, *contributed talk* (2023).
- Deutsche Physikalische Gesellschaft (DPG) SKM Frühjahrstagung, Dresden, Germany, *contributed talk* (2023).